

UNDERSTANDING DEFORMATION AND CYCLIC  
BEHAVIOR OF SHAPE MEMORY CERAMICS:  
A QUANTITATIVE PHASE-FIELD STUDY

by

Amirreza Lotfolahpour

Copyright by Amirreza Lotfolahpour 2024

All Rights Reserved

A thesis submitted to the Faculty and the Board of Trustees of the Colorado School of Mines in partial fulfillment of the requirements for the degree of Doctor of Philosophy (Mechanical Engineering).

Golden, Colorado

Date \_\_\_\_\_

Signed: \_\_\_\_\_

Amirreza Lotfolahpour

Signed: \_\_\_\_\_

Dr. Mohsen Asle Zaeem  
Thesis Advisor

Signed: \_\_\_\_\_

Dr. Cristian Ciobanu  
Thesis Co-advisor

Golden, Colorado

Date \_\_\_\_\_

Signed: \_\_\_\_\_

Dr. Carl Frick  
Professor and Department Head  
Department of Mechanical Engineering

## ABSTRACT

Zirconia-based shape memory ceramics (SMCs) are a class of intelligent materials that can be utilized in industries such as aerospace and biomedical engineering for their remarkable superelasticity (SE) and shape memory effect (SME). These ceramics are brittle and unable to fully accommodate the large shape change due to martensitic phase transformation (MPT) and this leads to their low fracture toughness and short cyclic life.

In this Ph.D. research, we aimed to develop a reliable computational framework to study the complex interactions between phase transformation, microstructural features, fracture, and plasticity in order to design SMCs with a higher fatigue life. For this purpose, first, we proposed a modified phase-field (PF) fracture model to study cracking in brittle materials at microscopic domains. Unlike traditional models, this modified model incorporates the influence of both fracture strength and cleavage plane effects simultaneously. As a result, it accurately reproduces the mechanical response and crack propagation path and reveals that intergranular fracture is the dominant type of cracking in ceramics.

Additionally, to investigate the interaction between cracking and MPT in SE SMCs, an advanced PF-based model was developed. Unlike previous PF-MPT models, this model successfully predicts the correct elastic response in the stress-strain curve. This improvement is attributed to the proposed modified chemical free energy formulation. This is the first PF model used for simulating cracking in SE regime and accurately predicts reverse MPT behind the crack tip, a phenomenon attributed to SE regime. In addition, the model captures the effects of grain orientation and predicts a final stress drop in the stress-strain curve.

Furthermore, to explore the influence of different microstructural features on the cyclic life of SMCs prior to fatigue crack initiation, the modified chemical free energy model was

integrated with a viscoplasticity model. The plastic strain accumulation (PSA) was used as a cyclic life indicator, and we aimed to lower PSA by microstructure tailoring. Simulations revealed that by controlling grain orientations, lowering the GB density, or locating pores at GBs, the PSA decreases significantly.

Finally, a new predictive numerical framework was developed incorporating the PF fracture, PF-MPT, and crystal viscoplasticity to study crystal-orientation dependent SE and SME behaviors of 3D micropillars. Through validation against experimental data, the proposed framework demonstrated the ability to accurately predict the intricate interplay between MPT, cracking, and plasticity. Our investigation revealed a broad spectrum of crystal orientations in which these ceramics undergo a complete MPT cycle without experiencing fracturing or slipping. However, we also identified certain orientations where either fracturing or slipping emerges as the dominant mechanism, with little to no observable MPT.

The findings of this Ph.D. research provided valuable insights into the crystal-orientation dependent mechanical properties of SMCs and strategies for enhancing their cyclic life, thus possibly enabling their practical applications.

## TABLE OF CONTENTS

ABSTRACT.....	iii
LIST OF FIGURES.....	viii
LIST OF TABLES .....	xi
ACKNOWLEDGMENTS.....	xii
CHAPTER 1 INTRODUCTION.....	1
1.1 Overload Crack Propagation.....	2
1.2 Cyclic Loadings .....	3
1.3 Modeling Techniques.....	6
1.3.1 Fracture.....	6
1.3.2 PF method for MPT .....	9
1.4 Objectives and Thesis Layout.....	10
CHAPTER 2 MODIFICATION TO BRITTLE PF FRACTURE MODEL TO INCLUDE MATERIAL STRENGTH AND CLEAVAGE PLANE.....	13
2.1 Abstract.....	13
2.2 Introduction.....	14
2.3 Phase-Field Model .....	16
2.4 Cleavage planes .....	17
2.5 Fracture surface energy and strength of GBs.....	19
2.6 Mechanical Properties of ZrB <sub>2</sub> .....	20
2.7 Creating Grains and GBs .....	22
2.8 Solution Scheme .....	23
2.9 Results and Discussion .....	23
2.9.1 Fracture surface energy anisotropy.....	24
2.9.2 Crack path and mechanical response of bicrystal models .....	25
2.9.3 Crack path and mechanical response of polycrystalline models .....	30
2.9.4 Crack path in polycrystalline models with strong texture .....	32
2.10 Conclusion .....	35
2.11 Appendix A - Derivation of Parameter <i>B</i> .....	36
CHAPTER 3 INTERACTIVE EVOLUTION BETWEEN CRACK PROPAGATION AND MARTENSITIC PHASE TRANSFORMATION.....	38
3.1 Abstract.....	38

3.2	Coupling PT and fracture in PF context.....	43
3.2.1	Elastic strain energy ( $F_{el}$ ) .....	43
3.2.2	Chemical free energy ( $F_{ch}$ ).....	45
3.2.3	Gradient free energy .....	46
3.3	Coupling MPT with fracture .....	46
3.4	Governing equations .....	47
3.5	The difference between linear and quadratic OP-strain relations .....	49
3.6	Solution scheme .....	50
3.7	Results and Discussion .....	51
3.7.1	Comparison of different $F_{ch}$ for modeling SE in 3Y-STZ .....	51
3.7.2	Modification of the chemical free energy ( $F_{ch}$ ).....	56
3.7.3	Interaction of MPT and fracture .....	60
3.8	Conclusion .....	65
CHAPTER 4 LOCALIZED PLASTIC STRAIN ACCUMULATION IN SHAPE MEMORY CERAMICS		
	UNDER CYCLIC LOADING.....	67
4.1	Abstract .....	67
4.2	Introduction.....	68
4.3	Phase-Field Model .....	73
4.3.1	Coupling the PF of MPT and viscoplasticity.....	73
4.3.2	Generating polycrystals .....	78
4.4	Solution Scheme and Model Parameters .....	80
4.4.1	Solution scheme and boundary conditions .....	80
4.4.2	Material properties and model parameters .....	82
4.5	Results and Discussion .....	83
4.5.1	Effects of grain boundary density.....	88
4.5.2	Effects of grain orientations .....	91
4.5.3	Effects of engineered pores .....	93
4.5.4	Analysis of parameters controlling PSA.....	95
4.6	Conclusions.....	98
4.7	Appendix B .....	99
CHAPTER 5 A 3D PHASE-FIELD MODEL FOR PREDICTING ORIENTATION-DEPENDENT		
	DEFORMATION AND FAILURE OF MICROPILLAR SHAPE MEMORY CERAMICS .....	103
5.1	Abstract.....	103
5.2	Introduction:.....	103

5.3	Formulation.....	106
5.4	Governing equations .....	109
5.5	Crystal viscoplasticity .....	110
5.6	Solution Scheme, boundary conditions, model and material constants: .....	112
5.7	Material properties and model parameters.....	113
5.8	Results and Discussion: .....	116
5.9	Identification of $\sigma_y0n$ in the crystal viscoplasticity model.....	121
5.10	Conclusions:.....	122
CHAPTER 6 CONCLUSIONS AND RECOMMENDATIONS FOR FUTURE WORK .....		124
6.1	Conclusions.....	124
6.2	Recommendations for Future Work.....	127
REFERENCES.....		129
APPENDIX A PERMISSION FOR REUSE OF PUBLISHED MATERIALS.....		142

## LIST OF FIGURES

Figure 1.1	TEM micrograph of alternating regions of untransformed (tetragonal) and transformed (monoclinic) regions in ceria-stabilized zirconia [13].	3
Figure 1.2	A zirconia-based single crystal SE SMC sample under compressive cyclic loading which fractures after 109 cycles [6].	4
Figure 1.3	Observation of slip in single crystal SMCs micropillars in some crystal orientations [8].	4
Figure 1.4	discrete crack (a), 2D PF crack approximation (b), 3D visualization of PF fracture profile (c) taken from [51].	8
Figure 1.5	Microstructure prediction by PF-MPT.	9
Figure 1.6	Schematics of $F_{ch}$ double-well used for simulating SE and SME behaviors.	10
Figure 2.1	The cleavage planes of $ZrB_2$ crystal: a) Prismatic view, and b) Isometric view.	22
Figure 2.2	A schematic of three adjacent grains, their orientations, and cleavage planes.	23
Figure 2.3	a) Geometry of the benchmark problem for studying the effect of $\alpha$ on the surface energy anisotropy, and b) the normalized surface energy for different values of $\alpha$ for the case of a material containing cleavage direction of $45^\circ$ .	25
Figure 2.4	The bi-crystal model and its boundary conditions.	26
Figure 2.5	The effect of $G_{cGB}$ on the crack path in bi-crystal model: (a-d) without cleavage planes, and (e-h) with cleavage planes.	27
Figure 2.6	The effect of strength on the crack path in bi-crystals, $G_{cGB} = 21\text{Jm}^2$ .	28
Figure 2.7	Crack paths and stress-strain curves for bi-crystal models: a) crack path with $G_{cGB} = 21\text{Jm}^2$ and without strength, b) stress-strain curve of (a), c) crack path with $G_{cGB} = 21\text{Jm}^2$ and $\sigma_{yGB} = 262\text{ MPa}$ , and d) stress-strain curve of (c).	29
Figure 2.8	Polycrystalline model: a) boundary conditions, and b) random grain orientation angles ( $\theta$ ) and cleavage plane directions ( $\varphi$ ).	30
Figure 2.9	The crack propagation in polycrystalline model: (a1)-(a4) without considering the cleavage planes and strength, (b1)-(b4) with considering only the cleavage planes, and (c1)-(c4) with considering both the cleavage planes and strength.	31
Figure 2.10	Stress-strain curve of the polycrystalline model: a) with cleavage plane and without strength (row b in Figure 2.9), and b) with cleavage plane and strength (row c in Figure 2.9).	32
Figure 2.11	Grain orientation angle and cleavage direction for a) Texture0, and b) Texture55.	33
Figure 2.12	The crack propagation in Texture0 model: (a1)-(a4) without considering the cleavage planes and strength, (b1)-(b4) with considering only the cleavage planes, and (c1)-(c4) with considering both the cleavage planes and strength.	33
Figure 2.13	The crack propagation in Texture55 model: (a1)-(a4) without considering the cleavage planes and strength, (b1)-(b4) with considering only the cleavage planes, and (c1)-(c4) with considering both the cleavage planes and strength.	34

Figure 2.14	Comparison of stress-strain curves of polycrystalline models with random grain orientations, Texture0, and Texture55.....	34
Figure 3.1	a) Dimensions and boundary conditions, and b) Applied displacement versus time for simulating forward and reverse transformation without fracture. x- axis represents <i>at</i> direction and z axis represent <i>ct</i> of the tetragonal phase .....	51
Figure 3.2	Three different <i>Fch</i> used for modeling SE.....	52
Figure 3.3	Predicted stress-strain curve and microstructure for [001] oriented sample by (I) Convex, (II) Concave, and (III) Double-well <i>Fch</i> . .....	55
Figure 3.4	a) The modified double-well versus double-well form of <i>Fch</i> , and b) The first derivative of the modified double-well form of <i>Fch</i> with respect to $\eta$ around $\eta = 0$ . .....	58
Figure 3.5	Predicted stress-strain curve and microstructure for [001] oriented sample by modified <i>Fch</i> . .....	59
Figure 3.6	Stress-strain curve, MPT, crack path, and stress map for [001] oriented sample under uniaxial tension in the z direction.....	61
Figure 3.7	The average volume fraction of the monoclinic variants vs. half crack length versus applied displacement for [001] oriented sample. ....	62
Figure 3.8	a) Stress-strain curve, MPT, crack path (deformed and undeformed), and stress map for [104] oriented sample under uniaxial tension in z direction, and b) Experimentally observed MPT and crack deflection due to PT in a zirconia-based ceramic [11]. .....	64
Figure 4.1	a) domain dimensions and boundary conditions, and b) applied displacement versus loading cycle.....	81
Figure 4.2	a) The obtained microstructure using 30 OPs in Eq.(4. 29, and b) Random orientations are assigned to grains. ....	85
Figure 4.3	Mechanical response ( $\sigma_y$ vs. $\epsilon_y$ ) of C1, C3, C7, and C9; MPT map at the beginning (I), end of loading (II), and end of unloading (III) of C9. ....	86
Figure 4.4	PSA plot; Equivalent plastic strain maps are shown at the end of unloading of C1, C3 and C9. ....	88
Figure 4.5	a) The PSA in the initial model, S1, and S2 sub domains; Inset-Top) the location of sub domains S1 and S2 in the initial model; Inset-Bottom) the MPT in S1 and S2 at the end of loading of C9; b) the equivalent plastic strain in S1 and S2 at the end of C9. ....	89
Figure 4.6	(a) The PSA versus number of loading cycles; Inset) MPT for RO and TX1 cases at the end of loading of C9; (b) the microstructure and grains orientation (top row), and the equivalent plastic strain in the domains at the end of C9 (bottom row). ....	91
Figure 4.7	(a) PSA plots; Inset) MPT for TX2, TX3 and TX4 at the end of loading of C9; (b) TX2 and TX3 grains orientation (top row), and equivalent plastic strain in TX2, TX3 and TX4 cases at the end of C9 (bottom row). ....	92
Figure 4.8	(a) PSA plots for different PVF and pore size, and (b) equivalent plastic strain in the domains with randomly distributed pores at the end of C9 for 4 different cases. ....	94

Figure 4.9 (a) PSA plot; (b) the equivalent plastic strain distribution in the domains with randomly distributed pores at the end of C9 (top row) and in the domains with pores located at GBs at the end of C9 (bottom row). .....	95
Figure 4.10 The correlation between the studied microstructural features and two target variables of $\epsilon_{pl}$ (at C9) and MPT fraction (at the end of loading of C9). .....	97
Figure 4.11 The distribution of dGB. ....	100
Figure 4.12 The analytical solution of Eq.(4.44) ( $\tanh(x2k)$ ) and the process of calculating the smeared interface width. ....	101
Figure 4.13 The distribution of $dGB \geq 2.6 \times 10^6 m - 1$ .....	102
Figure 5.1 Micropillar dimensions and boundary conditions. ....	113
Figure 5.2 Pole figure presenting the effects of grain orientation on the interplay between MPT, cracking, and slip in micropillars. ....	117
Figure 5.3 Load-displacement curve for selected pillar with full MPT. ....	119
Figure 5.4 The crack path, MPT, and mechanical response of p1 under load-controlled and displacement-controlled loading conditions. ....	120
Figure 5.5 Slip band formation and load-displacement curve of p1 with $\sigma_{y0n} = 550$ MPa and with MPT turned off. ....	122

## LIST OF TABLES

Table 3.1	Coefficients of different chemical free energies. ....	52
Table 3.2	Simulation parameters. ....	54
Table 3.3	Coefficients of the modified chemical free energy (Eq. (3.36)). ....	58
Table 4.1	Model parameters.....	83
Table 5.1	Model parameters.....	114
Table 5.2	Pillars ID and orientations .....	116

## ACKNOWLEDGMENTS

I would first like to thank my primary advisor, Professor Mohsen Asle Zaeem and I highly appreciate his support with my research endeavors and in helping me to develop a career path. I will always be very grateful for his advice, guidance, and support in my study, development, and career search.

Additionally, I extend my sincere appreciation to my co-advisor, Professor Cristian Ciobanu and highly appreciate his support with my research and in helping me to develop my teaching skills. His guidance during our collaboration in teaching different sections of Introduction to Solid Mechanics and Dynamics has been truly invaluable.

I would also like to thank the other students in the Computational Materials and Mechanics Laboratory (CMML), especially William Huber, for our enriching discussions, stimulating debates, and late-night meetings during the Covid pandemic.

I would like to thank my fiancée Katharyn, my parents Masoud and Rezvan, my sister Golnaz, and my friends for always supporting and encouraging me in this path.

Finally, I thank the U.S. National Science Foundation (NSF) for supporting this work under award number 2054274.

## CHAPTER 1

### INTRODUCTION

Zirconia based SMCs are a class of smart materials that can be used as actuators, sensors, thermal protection layers, and energy dampers due to their light weight and high melting temperature [1-4]. However, low fracture toughness and premature cracking have halted their applications under both overload and cyclic loadings. This issue is rooted in the required large shape change (both shearing and volume change) associated with MPT which these ceramics are unable to fully accommodate in macroscopic samples [5]. However, multiple experimental studies on microscopic samples reported full MPT over multiple loading cycles before fracture was developed in these ceramics [5, 6]. These studies established that microstructural features such as grain orientation and sample size play an important role in determining fracture and cyclic life in these ceramics. Therefore, microscope studies to identify the effects of microstructural features is a critical step toward designing microscopic and consequently macroscopic SMCs with desirable and enhanced mechanical properties. The current experimental studies [5-8] are limited to studying the effects of grain orientation and sample size and have not explored other important features such as grain size, textures, and pores. In addition, experimental studies have limitations and are unable to separately capture the effects of the microstructural features, i.e. entirely decoupled from other effects. Computational models can address the experimental studies limitations and can be used as a guide for future experiments. In this Ph.D. thesis, we have developed two PF based computational frameworks to investigate the overload cracking and cyclic response in Zirconia-based SMCs. The models formulated in this research are applicable beyond zirconia-based materials and can be effectively utilized for studying other shape memory materials, such as NiTi.

## 1.1 Overload Crack Propagation

The performance and durability of engineering materials including SMCs are dependent on their fracture behavior. Fracture can happen under overload conditions or due to cyclic loadings. Modeling crack propagation in transforming materials like SMCs presents unique challenges compared to non-transforming materials due to the intricate interactive evolution between cracks and MPT. Crack affects MPT where MPT can start from the crack tip. Additionally, MPT can alter the crack path leading to significant crack deflections and bifurcation.

Furthermore, MPT is an inelastic mechanism that dissipates a considerable amount of energy at the crack tip. This energy dissipation not only has a blunting effect on crack propagation, but also contribute to the rising R-curve observed in SMCs [9, 10]. The rising R-curve phenomenon refers to transformation toughening with crack extension, which is attributed to the energy-absorbing mechanisms associated with MPT. When the system is in SE regime, reverse MPT occurs behind the crack tip due to vanishing load bearing capacity behind the crack tip triggering the reverse transformation of martensite back to the original phase [11]. Reverse MPT behind the crack tip does not happen when the system is in SME regime.

In addition, the crack propagation and MPT are highly dependent on microstructural features such as grain size, GBs, and grain orientation. It is noteworthy that transformed microstructures, as observed in experimental studies comprise alternating regions of tetragonal and monoclinic phases (Figure 1.1) [12, 13].

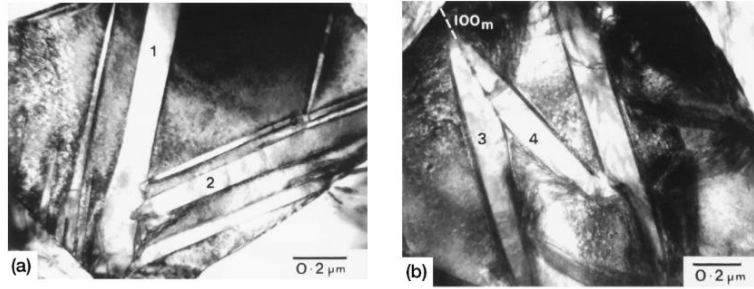


Figure 1.1 TEM micrograph of alternating regions of untransformed (tetragonal) and transformed (monoclinic) regions in ceria-stabilized zirconia, taken from [13]

Although there are many numerical studies on the microstructural evolution in SMCs [14-19], there are a limited number of papers [20-25] on the interactive evolution of cracking and MPT in these ceramics. However, they did not report a final stress drop in the stress-strain curve, mainly due to using load-controlled, rather than displacement-controlled, boundary conditions. In other words, these models were not able to establish an ultimate strength in the stress-strain curve and this is a common and noticeable shortcoming in all of these studies. Additionally, none of the previous studies [20-25] were performed in the SE regime due to the complexity of capturing reverse MPT behind the crack tip. Furthermore, these studies did not provide insight on the interaction between cracking and MPT and did not report an R-curve or crack propagation rate consistent with the experimentally reported transformation toughening in SMCs.

## 1.2 Cyclic Loadings

When SMCs are used as actuators or thermal protection layers, they undergo mechanical and/or thermal cyclic loadings. There are few experimental papers showing that microscopic samples can tolerate up to 100 cycles before they fracture, depending on the microstructure characteristics. For example, Lai et al. [5] showed that ceria stabilized tetragonal zirconia micropillars with diameters ranging from  $1.14\mu\text{m}$  to  $1.9\mu\text{m}$  and few grains (oligocrystalline) are able to handle compressive cyclic loads up to 53 cycles before they fracture. In a different study,

Du *et al.* [6] showed that single crystal spherical samples of 16mol%Ce-ZrO<sub>2</sub> are able to handle up to about 110 cycles before they fracture as illustrated in Figure 1.2.

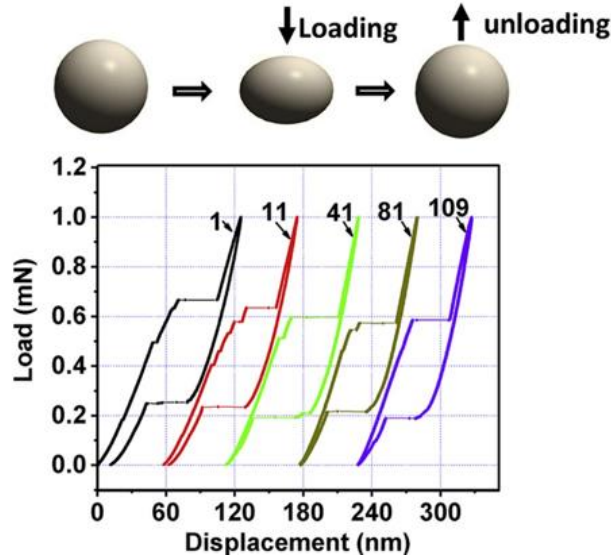


Figure 1.2 A zirconia-based single crystal SE SMC sample under compressive cyclic loading which fractures after 109 cycles, taken from [6].

In addition, it has been experimentally observed that these ceramics at microscale can show significant amount of plastic deformation as a result of irreversible mechanisms such as slip (Figure 1.3) [8] or GB sliding [26].

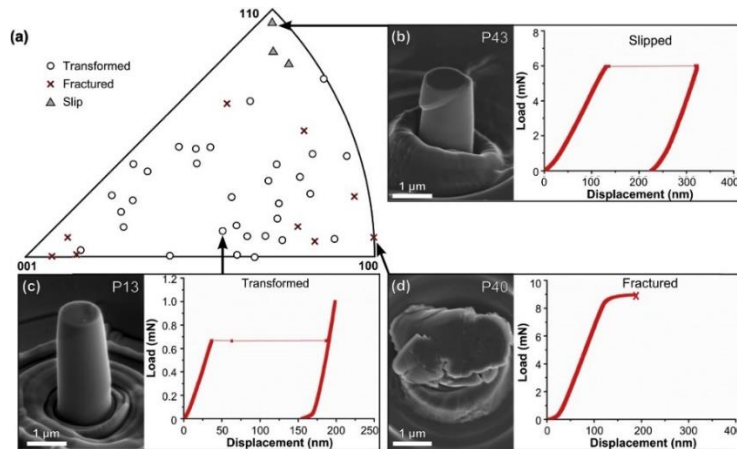


Figure 1.3 Observation of slip in single crystal SMCs micropillars in some crystal orientations, taken from [8].

In polycrystalline materials, cyclic plastic deformation mainly occurs at the sites with the highest stress concentration such as GBs [27], phase interfaces [28], and around inclusions [29] and the accumulation of these plastic strains leads to emergences of fatigue crack formation and propagation. Since SMCs are brittle, the cyclic life after fatigue crack formation will be limited [6]. Therefore, delaying fatigue crack formation is an effective approach to increase their cyclic life. The fatigue crack formation can be delayed by reducing the rate of PSA due to possible irreversible mechanisms. The occurrence of irreversible mechanism is highly dependent on the microstructural features. For instance, Zeng et al. [8] tested the compressive behavior of single crystal zirconia-based SMC micropillars with a wide range of crystal orientations. They observed that the inelastic deformation is governed only by slip in some specific crystal orientations and in some others only by MPT, and some crystal orientations show a combination of both MPT and slip plasticity (Figure 1.3). The same observations were reported by molecular dynamics (MD) [30] and phase-field (PF) simulations [18, 31]. These results indicate that it is possible to reduce the PSA and consequently increase the cyclic life of these ceramics by tailoring their microstructure. In simulating cyclic response of these ceramics, the PSA rate can be used as a cyclic life indicator to compare different microstructures and possibly find microstructure(s) with lowest PSA.

PSA has been used as a fatigue crack indicator in previous studies on different materials under cyclic loadings [32, 33]. In addition, there are limited number of studies on the cyclic response of shape memory materials including SMCs [34-37]. However, none of previous studies explored the effects of microstructural features on the PSA. In addition, most of these studies used complicated plastic models with numerous parameters, but they have not provided

prescriptions on determining these parameters [34, 38-41] and have not compared their results with experiments quantitatively.

### **1.3 Modeling Techniques**

#### **1.3.1 Fracture**

Among a variety of methods to model fracture, four methods of continuum damage models (such as Johnson and Cook's damage model [42], or Gurson's model [43]), cohesive zone methods (CZM) [44], extended finite element method (XFEM) [45, 46], and PF method [47, 48] have gained the most interest in the literature.

In continuum damage models, a parameter is used to define damage and this parameter degrades stiffness or the plastic yield surface to predict softening in the stress-strain curve as damage evolves. The softening causes strain localization in a single band of elements and makes these models extremely mesh objective [49].

CZM is another widely used method to simulate fractures in engineering materials. In this method a traction-separation relation is defined along the edges of elements where crack propagates on. The traction-separation relation determines the critical energy after which the separation between nodes occurs and the shape of the plot of the traction-separation law has a noticeable effect on the predicted stress-strain curve. The main drawback of CZM methods is that the crack path must be known prior to start of the simulation.

XFEM is a different method to model fracture. In this method, element shape functions must be modified to produce displacement jump across the crack face. Element modification, which is also known as element enrichment is a time-consuming process and makes the implementation of XFEM models challenging. In addition, this method is not able to predict

crack nucleation and crack path and an additional model is needed to dictate the crack nucleation and propagation path [50].

The PF method has been widely used recently to simulate fractures in brittle materials [47]. In PF method for brittle fracture, crack evolution (nucleation and propagation) is handled by only one equation and this equation can be solved by simple Lagrange elements. Equations (1.1) through (1.4) show the total energy of the system ( $F_{\text{tot}}$ ), elastic energy ( $F_{\text{el}}$ ), fracture energy ( $F_{\text{fr}}$ ), the crack evolution obtained through minimizing the energy functional with respect to order parameter (OP)  $\phi$ .

$$F_{\text{tot}}(u_i, \phi) = F_{\text{el}} + F_{\text{fr}} \quad (1.1)$$

$$F_{\text{el}}(u_i, \phi) = \int_V \frac{1}{2} g(\phi) C_{ijkl} \varepsilon_{kl}^{\text{el}} \varepsilon_{ij}^{\text{el}} dV \quad (1.2)$$

$$F_{\text{fr}}(\phi) = \int_V G_c \left( \frac{\phi^2}{2l} + \frac{l}{2} |\nabla \phi|^2 \right) dV \quad (1.3)$$

$$\frac{\partial \phi}{\partial t} = M \left( \frac{\delta F_{\text{tot}}}{\delta \phi} \right) = -(1 - \phi) C_{ijkl} \varepsilon_{kl}^{\text{el}} \varepsilon_{ij}^{\text{el}} + G_c \left( \frac{\phi}{l} - l \nabla^2 \phi \right) \quad (1.4)$$

where  $g(\phi) = (1 - \phi)^2$  is a degradation function to penalize the load bearing capacity as crack develops,  $G_c$  is the material critical energy release rate,  $C_{ijkl}$  is the material's elastic modulus ( $E$  in isotropic materials),  $\varepsilon_{ij}^{\text{el}}$  is elastic strain,  $M$  is a mobility parameter, and  $l$  is PF regularization parameter.

In PF fracture, element enrichment is not required, and the crack path does not need to be known before the start of the simulation. In PF fracture method similar to other PF methods, the discontinuity associated with fracture is smeared out over a band rather than being localized at a sharp interface. There is a regularization parameter  $l$  which controls the width of the localized band (Figure 1.4) and when  $l \rightarrow 0$  the problem converges to discrete fracture problem. Figure 1.4

shows a schematic of sharp crack (a), 2D representation of PF crack (b), and a 3D illustration of PF crack profile (c) [51].

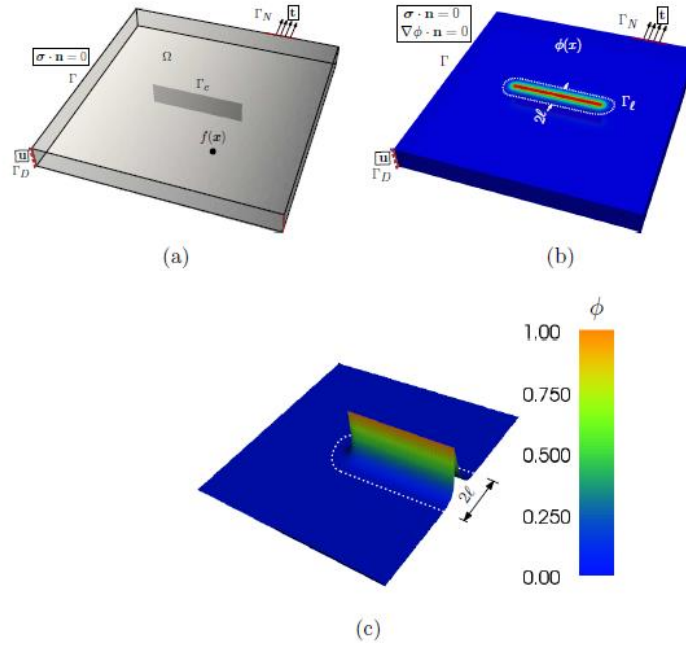


Figure 1.4 discrete crack (a), 2D PF crack approximation (b), 3D visualization of PF fracture profile (c), taken from [51].

It is worth noting,  $l$  must be small enough compared to sample dimension and some researchers suggest 10% of the length vertical to the crack path [52]. One of the shortcomings of this method is that the strength ( $\sigma_{cr}$ ) depends on three parameters of elastic modulus ( $E$ ), critical energy release rate ( $G_c$ ), and  $l$  and it does not consider the actual strength of the material. The equation shows the strength predicted by original brittle PF fracture which is obtained from analytical solution of time-independent, homogeneous, one-dimensional problem of (1.4):

$$\sigma_{cr} = \sqrt{\frac{EG_c}{6l}} \quad (1.5)$$

Based on equation (1.5), in microscale simulations, since  $l$  is small, the  $\sigma_{cr}$  is calculated to be extremely high and unrealistic. In this Ph.D. research we introduce a modification to the original brittle PF fracture to take into account the strength of the material to produce accurate stress-strain curve in microscale simulations.

### 1.3.2 PF method for MPT

The PF approach also stands out as a reliable method to model MPT in shape memory materials. In this method the energy dissipation due to MPT, also known as chemical energy ( $F_{ch}$ ), is written in terms of OPs and these OPs represent different phases in the system. The time evolution of each OP is derived by minimizing the total energy of the system with respect to each OP. The following equation shows the widely used 2-3-4  $F_{ch}$ :

$$F_{ch}(\eta_1, \eta_2, \dots, \eta_m) = \int_V \Delta G \left( a \sum_{p=1}^m \eta_p^2 - b \sum_{p=1}^m \eta_p^3 + c \left( \sum_{p=1}^m \eta_p^2 \right)^2 \right) dV \quad (1.6)$$

where  $\eta_p$  is the OP and varies between 0 to 1.  $\eta_p = 0$  represents original phase (tetragonal (T)) and  $\eta_p = 1$  represents  $p$ th product phase (monoclinic (M)) as shown in Figure 1.5.

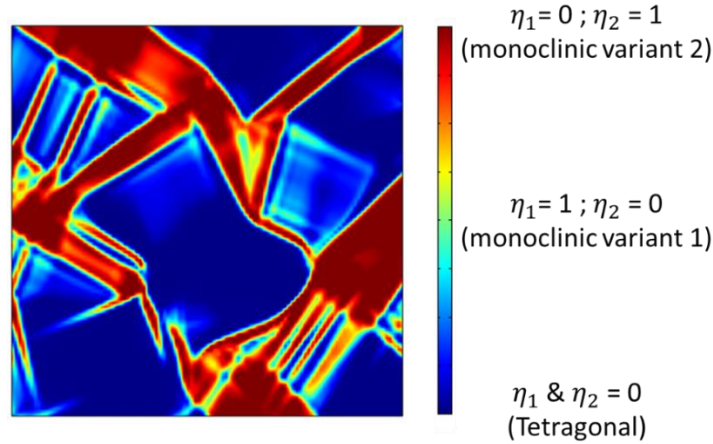


Figure 1.5 Microstructure prediction by PF-MPT.

In Eq. (1.6),  $\Delta G$  is the chemical driving force and is the difference in the specific  $F_{ch}$  between the parent and the product.  $a$ ,  $b$ , and  $c$  are model constants, and they determine the shape of the  $F_{ch}$  plot. To predict localized transformed regions and alternating regions of T and M (Figure 1.1 and Figure 1.5), the shape of chemical energy must be either double-well [16, 26, 53] or concave [54]. Figure 1.6 depicts the widely used  $F_{ch}$  double-well plots appropriate for modeling SE or SME behaviors.

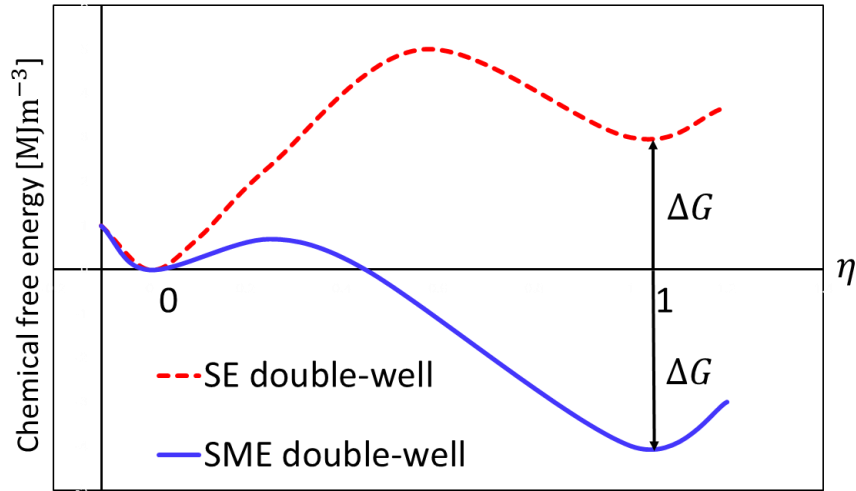


Figure 1.6 Schematics of  $F_{ch}$  double-well used for simulating SE and SME behaviors.

Most PF-MPT models underestimate the elastic modulus in the beginning of the stress-strain curve and are unable to produce accurate mechanical response. This issue is rooted in the order of  $F_{ch}$  polynomial and the rate of OPs' evolution upon loading. In this research, to address this issue we introduce a modification to the 2-3-4  $F_{ch}$  to control and slow down the evolution rate of OPs in the beginning of loading. We show that our modified  $F_{ch}$  retains all the requirements for  $F_{ch}$  and is able to predict accurate stress-strain curve.

#### 1.4 Objectives and Thesis Layout

The objectives of this thesis are as follows:

1. To modify the original PF brittle fracture model so as to take into account the strength of the material. In addition, the model we present includes the effects of cleavage planes. Including the effects of material's strength and cleavage plane makes our model a suitable model to study crack propagation in microscale samples and is able to produce correct stress-strain curve and crack path.
2. To modify PF-MPT models so as to correctly simulate the stress-strain curve in shape memory materials. Most previous PF-MPT underestimate the elastic modulus in the beginning of stress-strain by around 35%. We address this issue by modifying the  $F_{ch}$  to control the evolution rate of OPs. We show our model reduces the error to less than 5% and is able to produce reasonable stress-strain curve and microstructure.
3. To investigate the effects of microstructural features on cyclic response of SMCs by combining our modified PF-MPT and a viscoplasticity model. We study systematically the isolated effects of grain size, grain orientation, pores, and textures. We model the irreversible mechanisms such as slip GB sliding etc., in an average sense using a simple Von Mises based viscoplasticity model. We show that the model is able to predict rational PSA at each cycle and the results are close to experimental reports. We use the PSA rate as a cyclic life indicator and put suggestions to reduce it by tailoring microstructure.
4. To investigate the effects of grain orientation on the interplay between the MPT and failure in 3D SMC micropillars. To validate the model, we compare our results with available experimental reports. Our model can produce the same trend for orientation-dependence fracture, slip, or MPT.

The rest of this thesis is organized as follows. Chapter 2 presents a modified PF fracture which includes the effects of material strength and cleavage plane. We tested this model on bi-crystals and polycrystalline samples, and we report predicted crack path and stress-strain curve. Chapter 3 details our modified PF-MPT model. We first test our model on crack free single crystal samples to show the accuracy of predicted stress-strain curve under tensile loading. Then we add a central fracture to investigate the interactive evolution between cracking and MPT in SE SMCs for two different grain orientations. In chapter 4, we investigate the effects of microstructural features such as grain size, grain orientation, texture, pores as well as sample size on the cyclic response of polycrystalline SMCs. For this, we combine our modified PF-MPT with a viscoplasticity model. In Chapter 5 we investigate the mechanical response of 3D micropillars and we provide a pole plot to specify grain orientation effects on the competition between MPT, fracture and slip and we compare these results with experimental reports. At the end, Chapter 6 concludes the thesis and provides direction for future developments.

## CHAPTER 2

### MODIFICATION TO BRITTLE PF FRACTURE MODEL TO INCLUDE MATERIAL STRENGTH AND CLEAVAGE PLANE

Reproduced from A. Lotfolahpour and M. Asle Zaeem, “Effects of cleavage plane and material strength on fracture of polycrystalline brittle materials: A phase-field modeling study”, *Computational Materials Science* 197 (2021): 110642.

#### **2.1 Abstract**

A modified phase-field model for fracture is presented which includes the material strength and cleavage planes to quantitatively predict the crack propagation path and the mechanical response in polycrystalline brittle materials. To demonstrate the capability of this model, the crack initiation and propagation and the mechanical response in zirconium diboride bi-crystal and polycrystalline samples are investigated. Using a relationship analogous to the modified Read-Shockley model for grain boundaries with large misorientation angles, the fracture surface energy and the strength of the grain boundaries are made dependent on the misorientation angle of the adjacent grains. In general, the crack path inside each grain follows the orientation of the cleavage plane similar to the experimental observations. At the grain boundaries, a low fracture surface energy and/or a low material strength can result in intergranular crack propagation. Comparing the results of different models shows that to have a reasonable mechanical response it is necessary to include the material strength and cleavage planes in the formulations of the model. The proposed phase-field model enables designing texture and engineering grain boundaries to control intergranular and transgranular crack propagations and the macroscopic mechanical response.

## 2.2 Introduction

The size, shape and orientation of the grains and the properties of grain boundaries (GBs) strongly affect the overall mechanical properties and fracture behavior of polycrystalline materials. Consequently, prediction of cracking and fracture at the microscopic length scale is essential to obtain an accurate estimate of durability of structures.

At GBs, the atoms are not as well-ordered as inside the grains, also impurities and foreign atoms can segregate along GBs, making them weaker than inside the grains [55-57]. Therefore, GBs with a lower strength than grain interiors are more favorable sites for propagation of microcracks.

In general, microcracks can grow inside the grains (transgranular crack) or along the GBs (intergranular crack). Additionally, based on experimental observations the transgranular microcracks often change their direction grain to grain, and this behavior can be explained by cleavage or preferential planes with the lowest fracture resistance in the crystals [58, 59]. For example, there have been a variety of studies showing that the (0 0 1) plane is the cleavage plane in most body centered cubic (bcc) structures [60-62]. Also in another study done by Matsunaga et al. [63], it was observed that (010) plane is the cleavage plane of magnesium oxide by both experiments and molecular dynamics simulations [63].

To study and predict the fracture in polycrystalline materials, different numerical approaches have been proposed, mainly based on the extended finite element method (XFEM), the cohesive zone model (CZM), and the phase-field method (PFM). XFEM usually requires predefining the crack paths and enriching the involved nodes on the predefined paths; therefore, in the case of multiple crack interactions, XFEM may encounter convergence problems and also can become computationally expensive. In addition, predicting crack nucleation in XFEM needs

additional assumptions that makes its implementation more difficult. On the other hand, in CZM, the cohesive law must be defined along element boundaries; therefore, the crack propagation becomes mesh dependent. PFM was proposed to overcome some of these shortcomings.

PFM for fracture was first introduced by Francfort and Marigo [64]. They proposed a variational model based on Griffith's theory for studying the quasi-static brittle fracture. Initially this approach was used only for single crystal, single phase materials at macroscale level [65-67]. Also, in the original PFM studies, the fracture surface energy release rate ( $G_c$ ) was the only material property which determined the initiation and propagation of the crack. In order to address this shortcoming, Emdadi et al. [52] proposed a new model which considers the effect of material strength ( $\sigma_y$ ) on the crack initiation and growth in addition to  $G_c$ . This model was used later to design microarchitecture of  $ZrB_2$ -based ceramics to increase their fracture toughness [68].

More recently, some studies used PFM in microscale for predicting the initiation and propagation of transgranular and intergranular cracks in polycrystalline materials. For example Abdollahi et al. [69] studied the crack propagation in barium titanate polycrystalline and used the grain growth model proposed by Fan et al. [70] for representing the polycrystalline microstructure. Clyton et al. [71] proposed a PFM in order to consider the cleavage planes in each grain in polycrystalline materials. They investigated the effect of crystal and GB properties on crack path and mechanical response of SiC and Zn polycrystals. In another study by Nguyen et al. [72], the PFM in [71] was used for considering cleavage planes inside the grains, and they represented the GB as a smeared region instead of discrete boundary. Paggi et al. [73] studied the crack propagation in a two-dimensional (2D) solar grade polycrystalline silicon using a combination of phase-field and cohesive zone approaches. They considered orientation

dependent elastic constant and fracture surface energy in each grain. Also, they studied the effect of different GB fracture surface energy on the crack path. Nguyen-Thahn et al. [74] proposed a new adaptive higher order phase-field model to simulate crack in 2D and three-dimensional polycrystalline materials. In their model, the cleavage planes and elastic anisotropy are considered, however the effect of grain boundary properties versus misorientation angles and the strength of the material were not considered. Very recently, Emdadi and Asle Zaeem [75] considered different strengths and crack surface energies for GBs and inside grains, and studied intergranular and transgranular crack propagation in ZrB<sub>2</sub> bicrystal systems. To the best of our knowledge, no previous study concurrently considered the effect of cleavage planes and different strengths for GBs and inside grains to investigate the fracture behaviors in polycrystalline materials.

In this paper, we propose a model which considers the effects of both material strength and cleavage planes on crack initiation, propagation, and mechanical response in polycrystalline brittle materials. To demonstrate the capability of this model, the crack initiation and propagation in zirconium diboride (ZrB<sub>2</sub>) bi-crystal and polycrystalline samples are investigated.

### 2.3 Phase-Field Model

The initial variational form of Griffith's fracture theory [76] is:

$$E(\mathbf{u}, \Gamma) = \int_{\Omega} F_e(\boldsymbol{\varepsilon}(\mathbf{u})) d\Omega + G_c \int_{\Gamma} ds, \quad (2.1)$$

where  $F_e$  is the elastic energy density,  $\boldsymbol{\varepsilon}(\mathbf{u})$  is the strain tensor, and  $\mathbf{u}$  is the displacement.  $G_c$  is the fracture surface energy in Griffith's theory,  $\Omega$  is the domain volume in 3D or the domain area in 2D cases, and  $\Gamma$  is the crack surface area. Bourdin et al. [65] proposed the regularized formulation of Eq.(2.1) as:

$$E(\mathbf{u}, \phi) = \int_{\Omega} g(\phi) F_e(\boldsymbol{\varepsilon}(\mathbf{u})) d\Omega + G_c \int_{\Omega} \gamma d\Omega - \int_{\partial\Omega} \mathbf{t} \cdot \mathbf{u} ds, \quad (2.2)$$

$$\gamma = \frac{\phi^2}{2k} + \frac{k}{2} |\nabla\phi|^2. \quad (2.3)$$

$\phi$  is the scalar PF variable which represents the crack ( $\phi = 1$ ) and the intact material ( $\phi = 0$ ).  $\partial\Omega$  is the boundary of the domain.  $k$  is a positive regularization parameter with dimension of length to regulate the fracture zone.  $g(\phi)$  is the degradation function;  $g(\phi) = (1 - \phi)^2$  is one of the widely used degradation functions [74, 77, 78] that we adopt in this work as well.

The above formulation does not consider the material strength in the fracture process. In this paper, similar to Emdadi et al. [52], a correction parameter ( $B$ ) is derived and used to consider the effect of material strength on the crack path and mechanical response. In this paper, we introduce a more physical approach to calculate parameter  $B$  and to ensure a proper mechanical response. The details on deriving the parameter  $B$  is explained in the following subsection and in the Appendix A.

## 2.4 Cleavage planes

To consider cleavage planes in the PFM formulation, Clayton et al. [71] modified Eq.(2.3) by introducing a second order tensor ( $\boldsymbol{\omega}$ ):

$$\gamma = \frac{\phi^2}{2k} + \frac{k}{2} \boldsymbol{\omega} : (\nabla\phi \otimes \nabla\phi), \quad (2.4)$$

$$\boldsymbol{\omega} = \mathbf{I} + \alpha(\mathbf{I} - \mathbf{M} \otimes \mathbf{M}), \quad (2.5)$$

where  $\mathbf{M}$  is the unit vector normal to the preferential cleavage planes. For example, if the cleavage plane is oriented  $\varphi$  degree counterclockwise with respect to  $x$  axis (horizontal axis) in Cartesian coordinates, the vector  $\mathbf{M}$  is:  $-\sin(\varphi) \mathbf{i} + \cos(\varphi) \mathbf{j}$ . In addition,  $\alpha > 1$  is used to

prevent crack from propagating on planes not normal to  $\mathbf{M}$ , which also determines the extent of surface energy anisotropy (Figure 2.4).

By combining equations (2.2), (2.4) and (2.5), and making the variation of  $E$  equal to zero, following equation is obtained:

$$\begin{aligned} \delta E(\mathbf{u}, \phi) = & \int_{\Omega} g(\phi) \frac{\partial F_e(\boldsymbol{\varepsilon}(\mathbf{u}))}{\partial \boldsymbol{\varepsilon}} : \delta \boldsymbol{\varepsilon} d\Omega - \int_{\partial \Omega} \mathbf{t} \cdot \delta \mathbf{u} ds + \int_{\Omega} g(\phi)' F_e \delta \phi d\Omega \\ & + G_c \int_{\Omega} \left\{ \frac{\phi}{k} - k[\nabla^2 \phi + a(\nabla^2 \phi - \mathbf{M} \otimes \mathbf{M} : \nabla \nabla \phi)] \right\} d\Omega = 0. \end{aligned} \quad (2.6)$$

Eq. (2.6) must be valid for arbitrary values of  $\delta \mathbf{u}$  and  $\delta \phi$ , therefore, it leads to two equations:

$$\int_{\Omega} g(\phi) \frac{\partial F_e(\boldsymbol{\varepsilon}(\mathbf{u}))}{\partial \boldsymbol{\varepsilon}} : \delta \boldsymbol{\varepsilon} d\Omega - \int_{\partial \Omega} \mathbf{t} \cdot \delta \mathbf{u} ds = 0, \quad (2.7)$$

$$\int_{\Omega} g(\phi)' F_e(\boldsymbol{\varepsilon}(\mathbf{u})) \delta \phi d\Omega + G_c \int_{\Omega} \left\{ \frac{\phi}{k} - k[\nabla^2 \phi + a(\nabla^2 \phi - \mathbf{M} \otimes \mathbf{M} : \nabla \nabla \phi)] \right\} d\Omega = 0. \quad (2.8)$$

By applying the Gauss divergence theorem to Eq.(2.7) and Eq.(2.8), the following balance equations will be obtained for the PFM evolution and the linear momentum equation, respectively:

$$g(\phi)' F_e(\boldsymbol{\varepsilon}(\mathbf{u})) - G_c \left( \frac{\phi}{k} - k[\nabla^2 \phi + a(\nabla^2 \phi - \mathbf{M} \otimes \mathbf{M} : \nabla \nabla \phi)] \right) = 0, \quad (2.9)$$

$$\text{div}(\boldsymbol{\sigma}(\mathbf{u}, \phi)) = 0 ; \boldsymbol{\sigma}(\mathbf{u}, \phi) = g(\phi) \frac{\partial F_e(\boldsymbol{\varepsilon}(\mathbf{u}))}{\partial \boldsymbol{\varepsilon}} = g(\phi) \mathbf{C} : \boldsymbol{\varepsilon}, \quad (2.10)$$

Now similar to [52], the correction parameter  $B$  is introduced to consider the material strength and is multiplied to strain tensor, the final form of Eq.(2.10) becomes:

$$\text{div}(\boldsymbol{\sigma}(\mathbf{u}, \phi)) = 0 ; \boldsymbol{\sigma}(\mathbf{u}, \phi) = g(\phi) \frac{\partial F_e(\boldsymbol{\varepsilon}(\mathbf{u}))}{\partial \boldsymbol{\varepsilon}} = g(\phi) \mathbf{C} : (\sqrt{B} \boldsymbol{\varepsilon}). \quad (2.11)$$

As explained in Appendix A, for deriving parameter  $B$ , the width of the regularized crack is needed. The crack width is calculated to be  $2k\sqrt{1 + a(1 - \cos^2(\frac{\pi}{2} + \varphi))}$ , and the parameter  $B$  is determined as below:

$$B = \frac{\sqrt{1 + a(1 - \cos^2(\frac{\pi}{2} + \varphi)) k^*}}{k}, \quad (2.12)$$

$$k^* = \frac{27EG_c}{256\sigma_s^2}, \quad (2.13)$$

where  $\sigma_s$  is the material strength (fracture stress) and  $\varphi$  is the cleavage plane angle inside each grain. The parameter  $k^*$  is obtained through equating the maximum stress in front of crack tip to the material strength. The maximum stress is calculated based on the analytical solution of homogenous, one dimensional, quasi-static crack evolution equation [79, 80]. More details on the derivation of parameter  $B$  is provided in Appendix A.

In this paper, to ensure irreversibility of crack (crack healing prevention), the method proposed by Miehe et al. [81] is used by considering the maximum strain energy density history:

$$F_e(\boldsymbol{\varepsilon}(\mathbf{u}), t) = \max F_e(\boldsymbol{\varepsilon}(\mathbf{u}), s), \quad s \in [0, t]. \quad (2.14)$$

Since in this study only tension is applied, the anisotropy with respect to tension and compression is not considered in the model. Readers can refer to [79] for anisotropies in tension and compression.

## 2.5 Fracture surface energy and strength of GBs

Since the defects, impurities, and foreign atoms segregate in GBs, these regions have a higher energy and a lower strength compared to grain interior. Therefore, GBs are weak regions which are favorable for crack to initiate and/or propagate. In a study by Dai et al. [57] the strength of different types of GBs in  $ZrB_2$  with and without solute foreign atoms was calculated

using first principle calculations. They showed that GBs have a lower strength than grain interior, also their strength is highly dependent on the type of foreign solute atoms.

Read-Shockley model [82] relates the GB energy to misorientation angle of the neighboring grains for low-angle GBs. Wolf [83] modified the Read-Shockley model for both low and high-angle GBs. In this paper, the strength and fracture surface energy of GBs are dependent on GB misorientation angle. In both bi-crystal and polycrystalline models we consider a large range of grain orientations, therefore we use the modified Read-Shockley model [83]:

$$\begin{cases} \sigma_y^{gb}(\theta_{ij}) = \sigma_y^{bulk} [1 - (1 - \chi)\sin(\theta_{ij}) \times (1 - \ln\sin(\theta_{ij}))], & 0^\circ \leq \theta_{ij} \leq 90^\circ \\ \sigma_y^{gb}(180^\circ - \theta_{ij}) = \sigma_y^{bulk} [1 - (1 - \chi)\sin(180^\circ - \theta_{ij}) \times (1 - \ln\sin(180^\circ - \theta_{ij}))], & 90^\circ \leq \theta_{ij} \leq 180^\circ \end{cases} \quad (2.15)$$

where  $\sigma_y^{GB}$  and  $\sigma_y^{Bulk}$  are GB strength and grain interior strength, respectively, and  $\theta_{ij}$  is GB misorientation angle.  $\chi\sigma_y^{Bulk}$  ( $0 < \chi < 1$ ) is the minimum strength along the GBs. Since, based on the experimental results, the fracture strength of GBs can be less than 30% of the grain interior [84], we consider that  $\chi$  is equal to 0.25. Since in most of polycrystalline materials, low-angle GBs are more resistant to fracture than high-angle GBs [85, 86], a similar equation to Eq.(2.15) is used for making the fracture surface energy of GB ( $G_c^{GB}$ ) dependent on GB misorientation as well.

## 2.6 Mechanical Properties of ZrB<sub>2</sub>

The ZrB<sub>2</sub> has a hexagonal crystal structure and its single crystal elastic constants at room temperature are  $C_{11} = 567.8$  GPa,  $C_{33} = 436.1$  GPa,  $C_{12} = 56.9$  GPa,  $C_{13} = 120.5$  GPa,  $C_{44} = 247.5$  GPa in the coordinate system where  $x_3$  is parallel with the axis of the hexagonal ( $z$  in Figure 2.1) [87]. We considered different GB orientations for bi-crystal and polycrystalline models,

and the following transformation operation is used to determine the elastic stiffness matrix for individual grains with different grain orientations:

$$C_{ijkl}^{bulk} = \mathbf{R}_{im} \mathbf{R}_{jn} \mathbf{R}_{ko} \mathbf{R}_{lp} C_{mnop}, \quad (2.16)$$

where  $C_{mnop}$  is the elastic stiffness matrix of a grain in the local coordinate system, and  $C_{ijkl}^{bulk}$  is its elastic stiffness matrix in the global coordinate system.  $\mathbf{R}_{ij}$  is the rotation matrix for a grain with an orientation angle of  $\theta_k$ :

$$\mathbf{R}_{ij} = \begin{bmatrix} \cos(\theta_k) & \sin(\theta_k) \\ -\sin(\theta_k) & \cos(\theta_k) \end{bmatrix}. \quad (2.17)$$

The fracture surface energy in grain interiors is  $G_c^{Bulk} = 24 \frac{\text{J}}{\text{m}^2}$  [88]. Also, the strength in grain interiors is  $\sigma_y^{Bulk} = 350 \text{ MPa}$  which is selected based on one of the highest values reported by experiments for the bulk  $\text{ZrB}_2$  at room temperature [89]. In this study, two parallel cleavage planes are considered in each grain which they are  $(10\bar{1}1)$  and  $(10\bar{1}\bar{1})$  [90]. It is worth mentioning that both cleavage planes have the same normal vector (M). Also, considering the lattice parameters of  $a = 3.17 \text{ \AA}$  and  $c = 3.544 \text{ \AA}$  [91], the angle of cleavage planes with respect to the top plane of (0001) of the crystal ( $\varphi$  in Figure 2.1) is about  $48.19^\circ$  in each grain. In the GBs the isotropic properties of  $\text{ZrB}_2$ ,  $E = 500 \text{ GPa}$  and  $\nu = 0.13$  [88], is assumed. In those bi-crystal models that cleavage plane is considered, the value of 5 is chosen for  $\alpha$  (Eq.(2.5)).

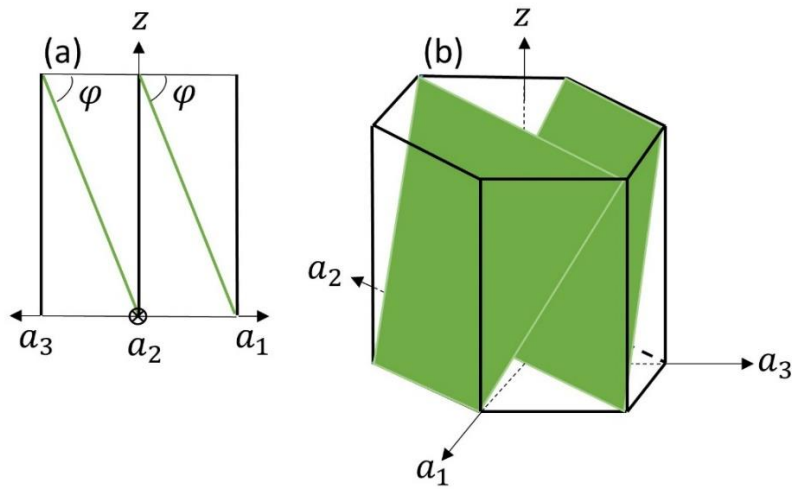


Figure 2.1 The cleavage planes of  $ZrB_2$  crystal: a) Prismatic view, and b) Isometric view

## 2.7 Creating Grains and GBs

Figure 2.2 shows a schematic of three adjacent grains and demonstrates the approach used for creating grains and GBs in both bicrystal and polycrystalline models. The orientation angle of grain 1 ( $\theta_1$ ) is equal to 0. By rotating the crystals only around  $a_2$  axis, a new grain is created. In this example, grain 2 and grain 3 are created by rotating grain 1 for  $30^\circ$  and  $60^\circ$  counterclockwise around  $a_2$  axis, respectively. Since  $a_2$  is the only rotation axis and it is perpendicular to  $(\bar{1}2\bar{1}0)$  plane,  $180^\circ$  is the crystal symmetry. In other words, when the misorientation angle between two grains is equal to  $0^\circ$  or  $180^\circ$ , prismatic planes match, therefore no GB forms.

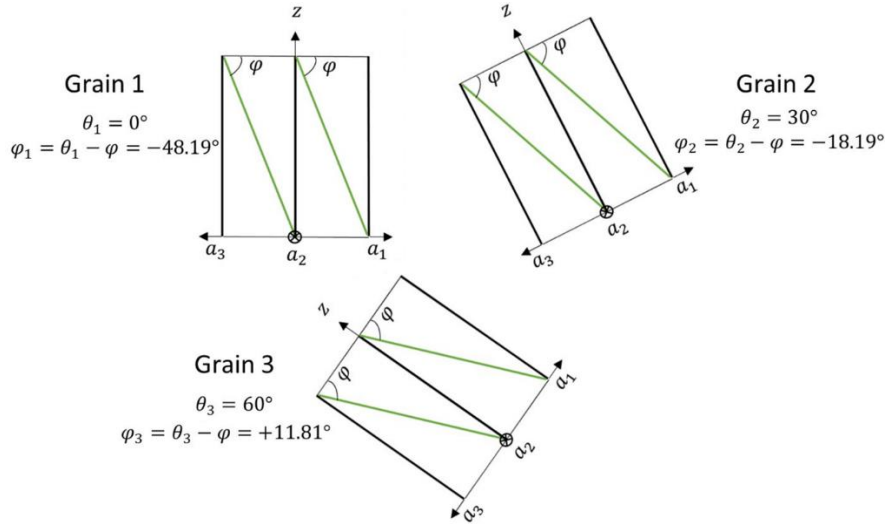


Figure 2.2 A schematic of three adjacent grains, their orientations, and cleavage planes.

## 2.8 Solution Scheme

The governing equations of the presented PFM were solved in a finite element framework using the mathematics modulus of COMSOL Multiphysics. Lagrangian triangle elements were used in all the simulations. The widely used staggered scheme, which is called the segregated scheme in COMSOL, is adopted to solve the governing equation. Since the total energy functional with respect to the primary variables is non-convex, the monolithic scheme for solving these governing equations has convergence problems. By fixing one primary variable in the staggered scheme, the total energy functional becomes convex, therefore it usually does not have convergence problem; this process has been widely used for solving governing equations of PFM of fracture [92]. It is worth mentioning, all simulations were performed on a desktop computer equipped with two Xeon Gold 6163 processors (24 CPU cores) and 128 GB of RAM.

## 2.9 Results and Discussion

In this section the numerical results for crack propagation in bi-crystals and polycrystalline models are presented. In subsection 2.9.1, the effect of parameter  $\alpha$  in Eq.(2.5) on

the extent of anisotropy of the fracture surface energy is studied using a benchmark problem introduced in [72]. In subsection 2.9.2, first, four models without considering the cleavage planes and strength are considered to investigate the effect of fracture surface energy of the GB on the crack path. Then the effect of cleavage planes and GB strength on the crack path in the same bi-crystal models are investigated. Finally, in subsection 2.9.3, the crack propagation in a polycrystalline model is studied considering all the physical characteristics.

### 2.9.1 Fracture surface energy anisotropy

A benchmark problem is considered to study the effect of parameter  $\alpha$  on the fracture surface energy anisotropy, shown in Figure 2.3a [72]. The order parameter is set to 1 (fully cracked) inside a circle with radius of 0.05 mm at the center of the domain. Also, a single cleavage direction of  $\varphi = 45^\circ$  is considered in the entire domain. The magnitude of the fracture surface energy around the circle and at a distance of  $2l = 0.01$  mm is measured. Then the normalized surface energy is plotted in Figure 2.3b. It is worth mentioning that  $E$  and  $G_c$  are considered equal to 500 GPa and  $24 \frac{\text{J}}{\text{m}^2}$  respectively. When  $\alpha = 0$  there won't be fracture surface energy anisotropy and the original PFM equation is recovered. Also, as it can be seen in Figure 2.3b, by increasing the  $\alpha$  the fracture surface energy anisotropy will increase. In this paper in some bi-crystal and polycrystalline models that cleavage plane is considered, in grain interior,  $\alpha$  is chosen to be 5 and in GBs it is equal to zero. After testing several values for  $\alpha$ ,  $\alpha=5$  was the minimum value that crack followed the predefined cleavage planes inside the grains.

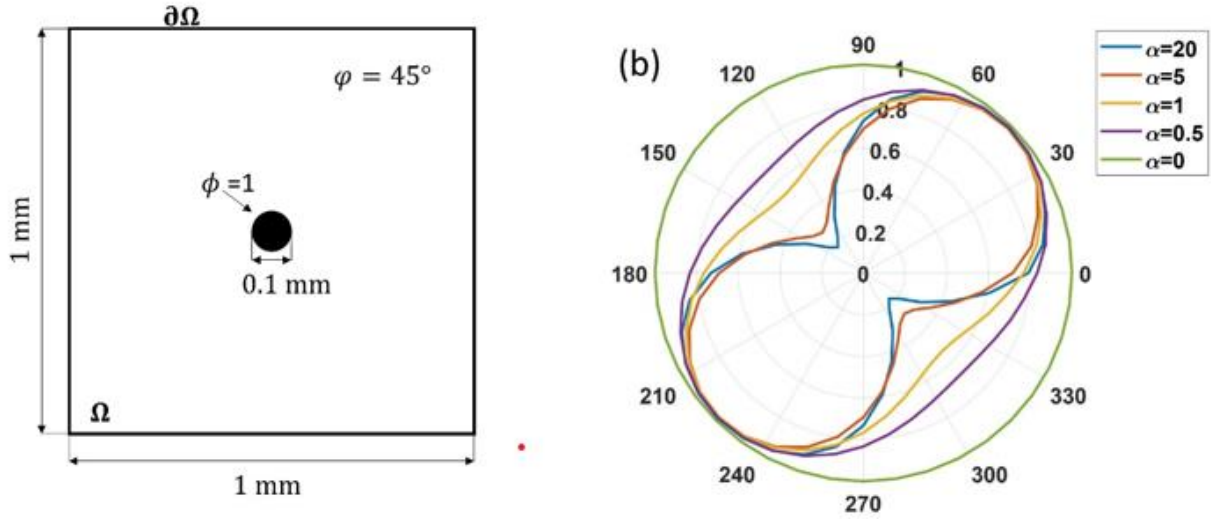


Figure 2.3 a) Geometry of the benchmark problem for studying the effect of  $\alpha$  on the surface energy anisotropy, and b) the normalized surface energy for different values of  $\alpha$  for the case of a material containing cleavage direction of  $45^\circ$ .

## 2.9.2 Crack path and mechanical response of bicrystal models

The geometry, dimensions and boundary conditions of the bi-crystal model are given in Figure 2.4. The GB width is 10 nm.  $\theta_i$  is the grain orientation and  $\varphi_i$  is the direction of cleavage plane in each grain, and their relationship is shown in Figure 2.2. In all bi-crystal models,  $k = 5$  nm and  $\theta_1 = 0^\circ$ . Also,  $\theta_2$  is calculated based on the selected values of  $G_c^{GB}$  or  $\sigma_y^{GB}$  using Eq.(2.15). In addition,  $\theta$  inside the GB is zero. Likewise, a uniform displacement of  $u^* = \dot{u} \times t$  is applied to the top edge.  $\dot{u}$  is a uniform displacement rate of  $20 \text{ nms}^{-1}$  and the time increment is  $500 \mu\text{s}$ . The bottom boundary is fixed in both  $x$  and  $y$  directions. A uniform mesh (the mesh size is the same in entire domain) with 322,139 linear triangle elements is used in bi-crystal models. It is worth mentioning that we conducted a mesh study, we found at least three elements should be used within GB width to ensure convergence and accuracy. Plane stress condition is assumed for all the simulations.

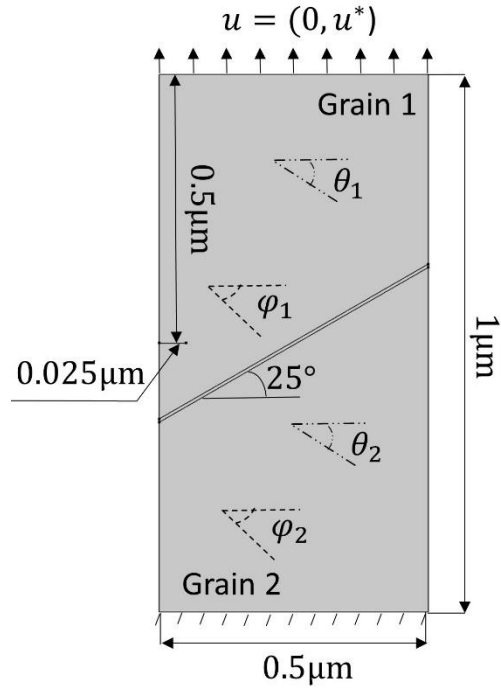


Figure 2.4 The bi-crystal model and its boundary conditions.

The crack path in the bi-crystal models is investigated considering different  $G_c^{GB}$ , and the results are shown in Figure 2.5. In these models, the effect of  $G_c^{GB}$  on the crack path is studied without (Figure 2.5 (a)-(d)) and with (Figure 2.5 (e)-(h)) considering cleavage planes. It is evident that the crack follows the cleavage plane direction inside each grain. Also, by decreasing the  $G_c^{GB}$ , with or without considering cleavage planes, the crack tends to become intergranular. In other words, there is a transition from transgranular to intergranular crack by decreasing  $G_c^{GB}$ .

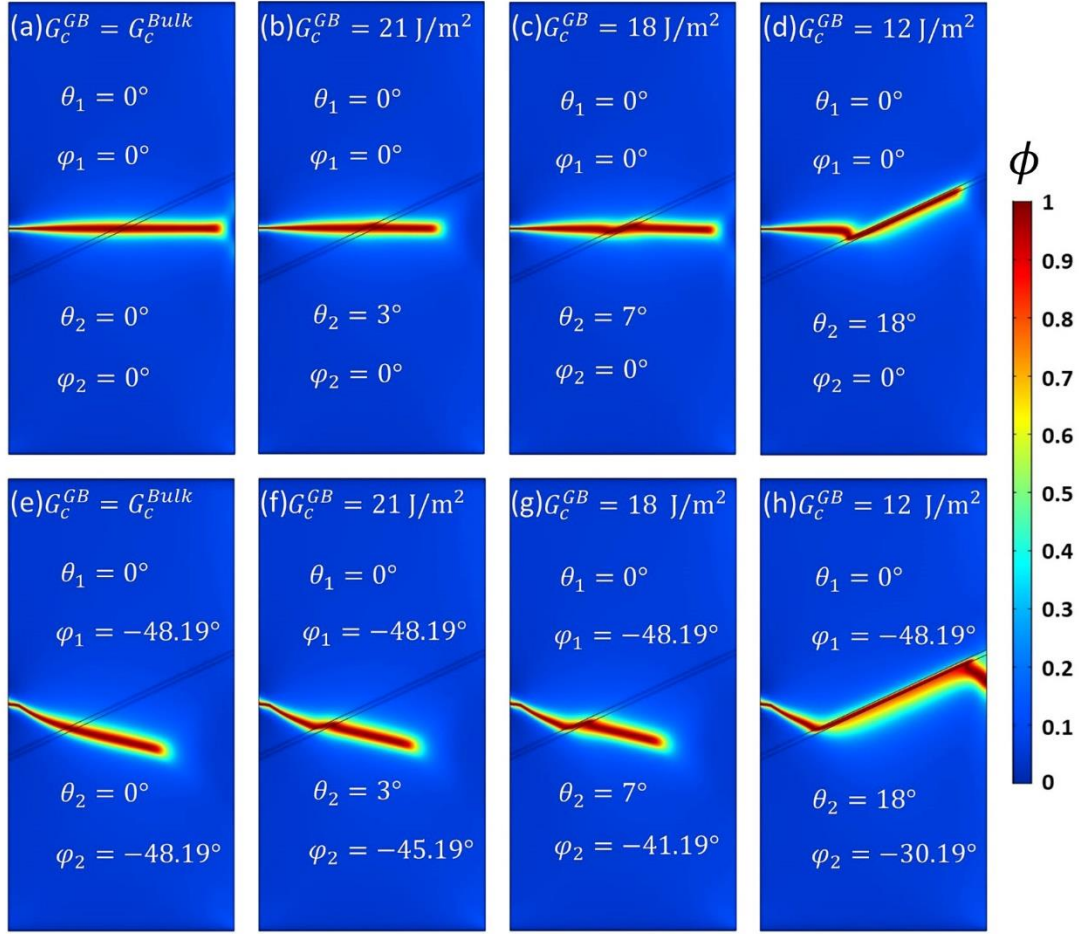


Figure 2.5 The effect of  $G_c^{GB}$  on the crack path in bi-crystal model: (a-d) without cleavage planes, and (e-h) with cleavage planes.

To study the effect of strength of GB, the correction parameter  $B$  is added to Eq.(2.10).

$G_c^{GB} = 21 \frac{\text{J}}{\text{m}^2}$  is chosen independent of GB misorientation angle. Four different  $\sigma_y^{GB}$  equal to  $\sigma_y^{Bulk}$ ,  $0.75\sigma_y^{Bulk}$ ,  $0.5\sigma_y^{Bulk}$ , and  $0.25\sigma_y^{Bulk}$  are considered to study the effect of  $\sigma_y^{GB}$  on crack path.  $\theta_2$  is calculated based on the values of  $\sigma_y^{GB}$  using Eq.(2.15). Results in Figure 2.6 show by reducing the  $\sigma_y^{GB}$ , the crack tends to grow and stay inside the GB before entering grain 2. The presented results demonstrate that the PFM is effectively modified for considering the effects of material strength on the crack path.

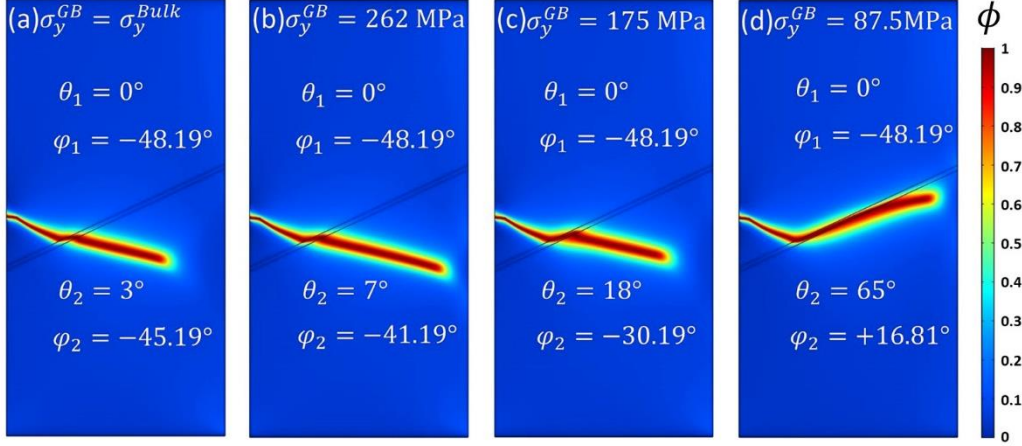


Figure 2.6 The effect of strength on the crack path in bi-crystals,  $G_c^{GB} = 21 \frac{\text{J}}{\text{m}^2}$ .

Additionally, we investigated the mechanical response of bi-crystal samples. In other brittle fracture models, the length scale parameter  $k$  significantly affects the maximum stress ( $\sigma_y$ ) that material can bear before fracture initiates. To target a specific value of  $\sigma_y$ , other models [67, 79, 80] consider  $k$  to be a material property which is chosen according to Eq.(2.13). For  $\text{ZrB}_2$  with  $G_c = 24 \frac{\text{J}}{\text{m}^2}$ ,  $\sigma_y = 350 \text{ MPa}$ , and Young's modulus ( $E$ ) equal to 500 GPa, Eq.(2.13) yields to  $k$  of  $10.33 \mu\text{m}$ . Essentially for each material property set, there is one value of  $k$ . But this length scale is only appropriate for domains that are in millimeter length scale. Because the diffusive crack width is equal to  $2k$ , such a value of  $k$  cannot be used for small domains that are several microns by several microns, such as the ones for study of polycrystalline systems. On the other hand, for small domains like the ones in this paper, if a small  $k$  is chosen, for example  $k = 5 \text{ nm}$  in this paper, although an acceptable crack width and path will be obtained, the maximum stress will be very high, therefore, the mechanical response will be unrealistic. Figure 2.7b shows the mechanical response of bi-crystal model considering  $G_c^{GB} = 21 \frac{\text{J}}{\text{m}^2}$  and without strength (case (f) in Figure 2.5). As it is shown in this figure the maximum stress is about 10GPa which is unacceptable since the failure strength in grain interiors is 350 MPa; the maximum amount of

stress that single crystal  $\text{ZrB}_2$  can tolerate in tension. The modified phase-field model presented in this paper solves this problem and not only provides a correct crack path, but also yields an acceptable mechanical response. Figure 2.7(d) shows the mechanical response of bi-crystal model considering  $G_c^{GB} = 21 \frac{\text{J}}{\text{m}^2}$  and  $\sigma_y^{GB} = 262 \text{ MPa}$  (case (b) in Figure 2.6). In Figure 2.7(d), the maximum stress is about 155 MPa which is in an acceptable range. The tensile strength in grain interiors is equal to 350 MPa, and since there is an initial crack and a GB in the domain, it is reasonable that the predicted maximum stress is lower than the strength in grain interiors. It is also worth mentioning that the length of initial crack affects the maximum stress, and a smaller initial crack produces a higher stress before propagation starts.

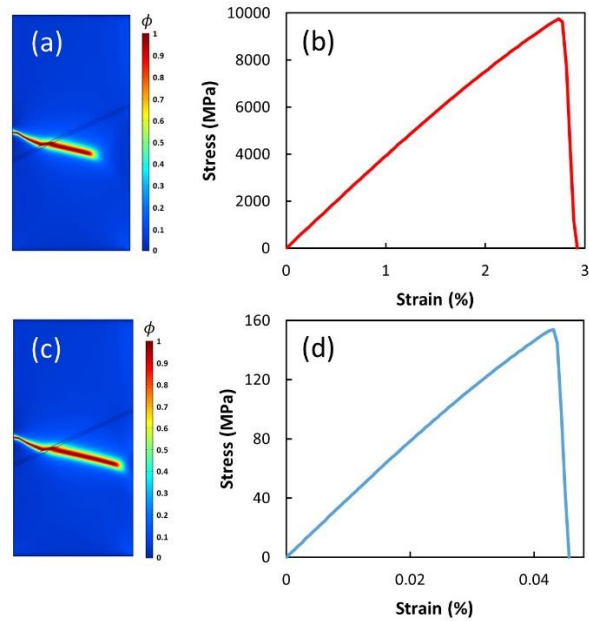


Figure 2.7 Crack paths and stress-strain curves for bi-crystal models: a) crack path with  $G_c^{GB} = 21 \frac{\text{J}}{\text{m}^2}$  and without strength, b) stress-strain curve of (a), c) crack path with  $G_c^{GB} = 21 \frac{\text{J}}{\text{m}^2}$  and  $\sigma_y^{GB} = 262 \text{ MPa}$ , and d) stress-strain curve of (c).

### 2.9.3 Crack path and mechanical response of polycrystalline models

In this section the crack evolution in a polycrystalline model consisting of 13 grains with an average size of about  $2\ \mu\text{m}$  (the average grain size of  $\text{ZrB}_2$  [93]) will be investigated. The boundary conditions and random grain orientations of the polycrystalline model are depicted in Figure 2.8. The same thickness of GBs and  $k$  (regularized parameter) used in bi-crystal models are used for polycrystalline model as well. Plane stress condition is assumed. The bottom edge is fully constrained and a uniform displacement of  $u^* = \dot{u} \times t$  is applied to the top edge.  $\dot{u}$  is a uniform displacement rate of  $80\ \text{nms}^{-1}$  and the time increment is  $500\ \mu\text{s}$ . A uniform mesh with 3,424,409 linear triangle elements is used.

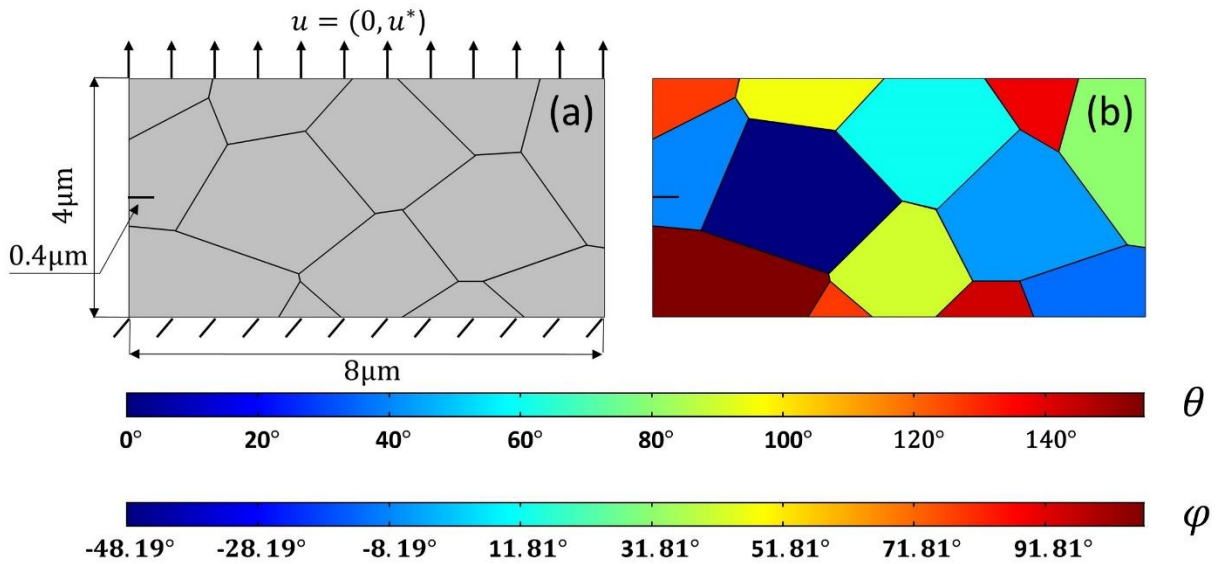


Figure 2.8 Polycrystalline model: a) boundary conditions, and b) random grain orientation angles ( $\theta$ ) and cleavage plane directions ( $\varphi$ ).

Figure 2.9(a1)-(a4) shows the crack path in the polycrystalline model without considering cleavage planes and strength at different time steps. Likewise, Figure 2.9(b1)-(b4) shows the crack path with cleavage planes and without considering strength. In rows (a) and (b) the effect of strength is not considered, but since  $G_c$  is dependent on misorientation angle, intergranular fracture is observed in some GBs. Eventually, Figure 2.9(c1)-(c4) shows the crack path with both

cleavage planes and strength's effect at different time steps. As it is shown in this figure, there is a combination of transgranular and intergranular cracks similar to experimental observations [94]. Also, since the strength in GBs is lower than grain interior, it has a noticeable effect on crack path and promotes intergranular fracture. Figure 2.10a shows the mechanical response of polycrystalline model considering cleavage planes but without considering the strength (row b in Figure 2.9). In this case the maximum stress is about 6 GPa which is much higher than the tensile strength of the grain interior, which is unacceptable. On the other hand, Figure 2.10b shows the mechanical response with considering strength using the modified phase-field model (row c in Figure 2.9). The maximum stress is about 110 MPa which is in an acceptable range. It is worth mentioning, for polycrystalline  $ZrB_2$ , the strength has been reported by experiment to be in the range of 150 MPa [95] to 350 MPa [89] at room temperature.

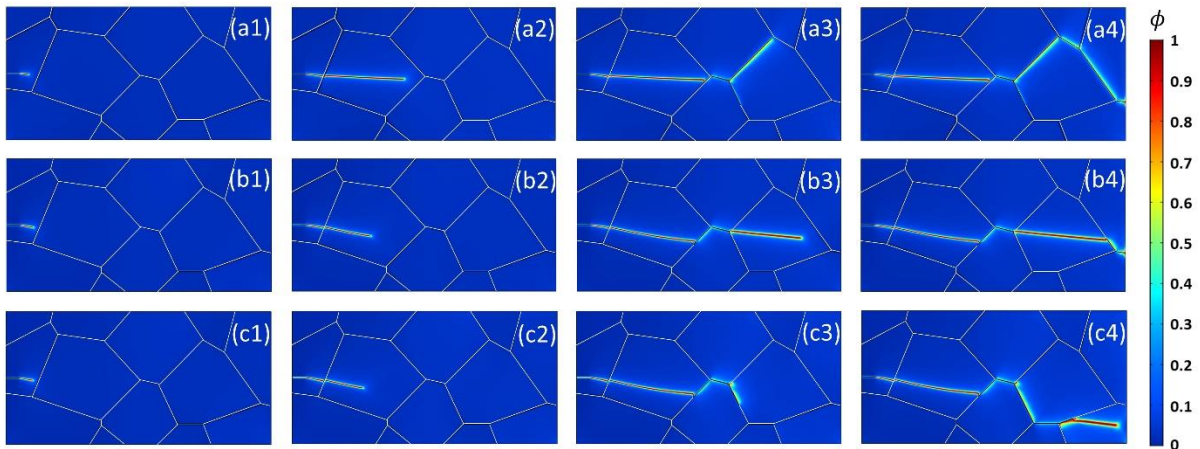


Figure 2.9 The crack propagation in polycrystalline model: (a1)-(a4) without considering the cleavage planes and strength, (b1)-(b4) with considering only the cleavage planes, and (c1)-(c4) with considering both the cleavage planes and strength.

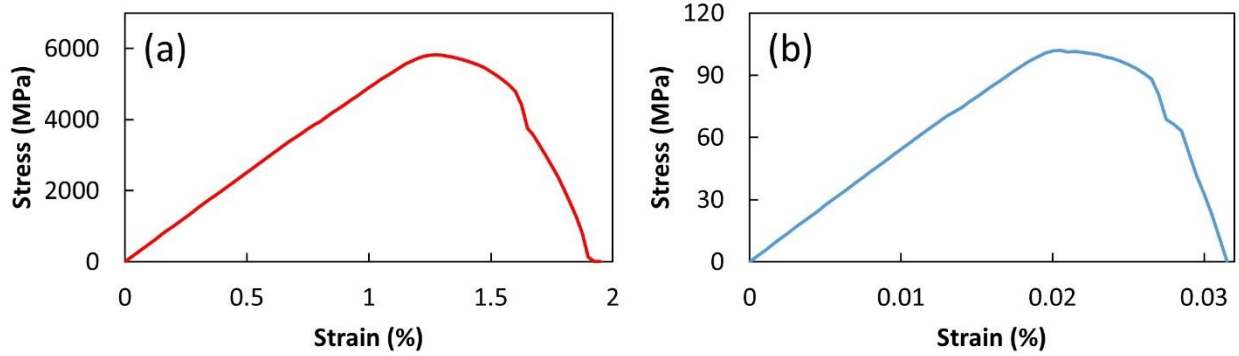


Figure 2.10 Stress-strain curve of the polycrystalline model: a) with cleavage plane and without strength (row b in Figure 2.9), and b) with cleavage plane and strength (row c in Figure 2.9).

#### 2.9.4 Crack path in polycrystalline models with strong texture

In the previous section, the crack path and mechanical response of the polycrystalline model with random misorientation angles was studied. In this section the crack path in the polycrystalline models with low misorientation angles (texture) is studied. For this purpose, two sets of misorientation angles of  $\theta = 0^\circ \pm 10^\circ$  (Texture0) and  $\theta = 55^\circ \pm 10^\circ$  (Texture55) are considered (Figure 2.11). The same boundary conditions shown in Figure 2.8 are applied. Figure 2.13 show the crack path in Texture0 and Texture55, respectively. In these figures similar to Figure 2.9, row (a) shows the crack path without cleavage planes and strength, row (b) shows the crack path with cleavage planes and without strength, and row (c) shows the crack path with considering both the cleavage planes and strength. It is worth mentioning, similar to Figure 2.9, in all rows the  $G_c$  is dependent on misorientation angles.

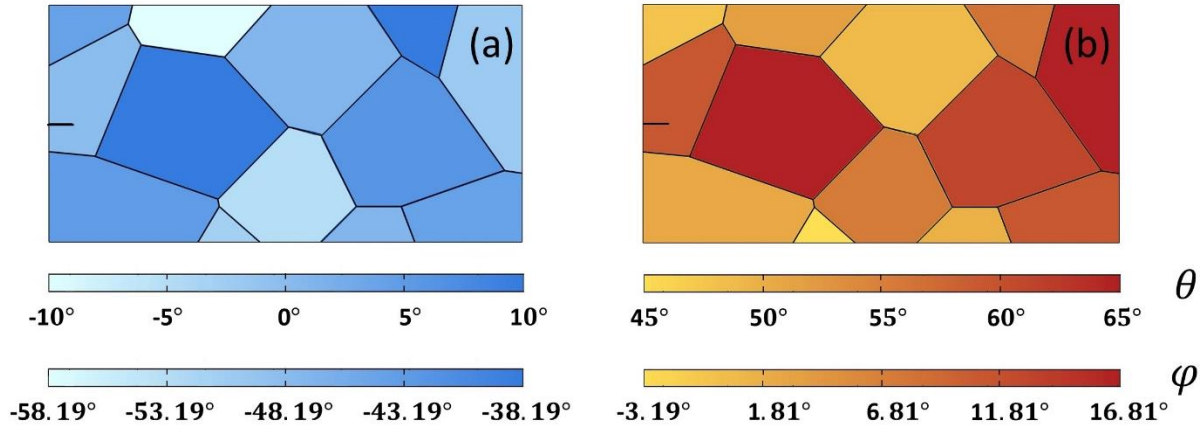


Figure 2.11 Grain orientation angle and cleavage direction for a) Texture0 , and b) Texture55.

Since in these two cases the misorientation angles of neighboring grains are rather small, the values of  $G_c^{GB}$  and  $\sigma_y^{GB}$  are close to  $G_c^{Bulk}$  and  $\sigma_y^{Bulk}$ , respectively; therefore, intergranular crack is not promoted. Figure 2.14 shows the comparison of mechanical responses of polycrystalline models with random grain orientations (Figure 2.8) and those with texture.

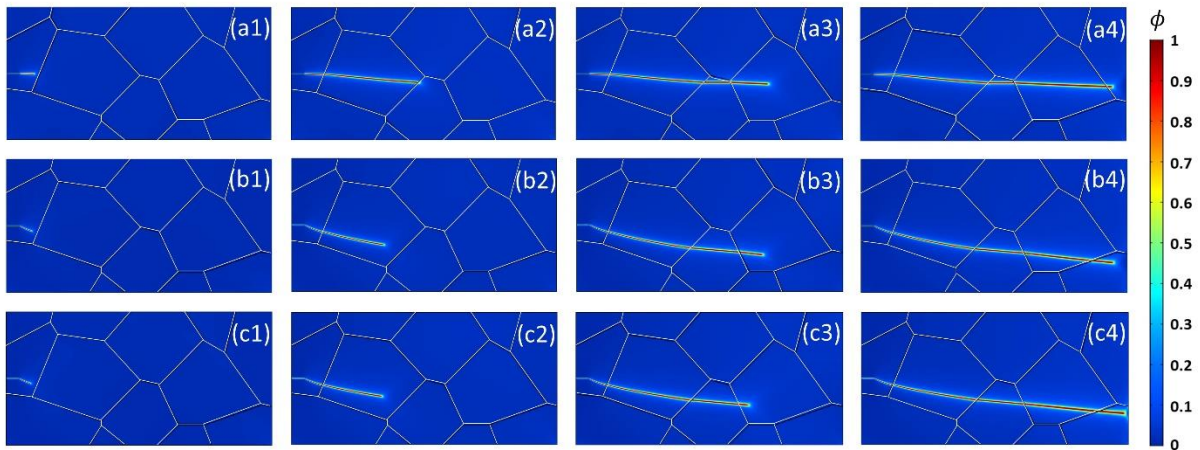


Figure 2.12 The crack propagation in Texture0 model: (a1)-(a4) without considering the cleavage planes and strength, (b1)-(b4) with considering only the cleavage planes, and (c1)-(c4) with considering both the cleavage planes and strength.

Both Texture0 and Texture55 show a lower toughness compared to the case with random grain orientations. This observation can be explained based on crack deflection due to intergranular fracture. According to experimental results [96], crack deflection along GBs in

ceramics can lead to increase in toughness. From Figure 2.14, the apparent Young's modulus of Texture0 model is lower than that of two other cases because of elastic anisotropy. In other words, since in Texture0 the orientation of the grains is close to  $0^\circ$ , the apparent Young's modulus is close to  $C_{33} = 436.1$  GPa. In addition, the apparent Young's modulus in the case with random grain orientations is about 520 GPa, which is in good agreement with the experimental result of 500 GPa for  $ZrB_2$  [88].

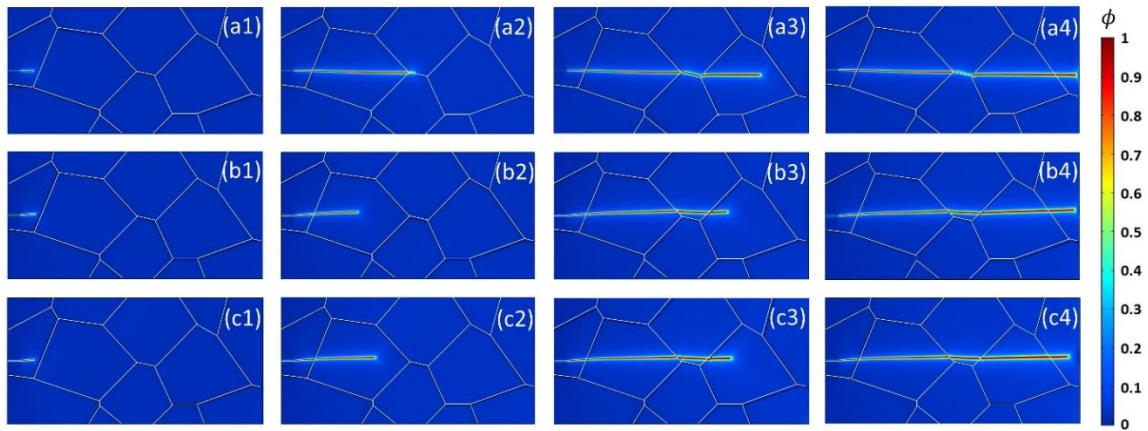


Figure 2.13 The crack propagation in Texture55 model: (a1)-(a4) without considering the cleavage planes and strength, (b1)-(b4) with considering only the cleavage planes, and (c1)-(c4) with considering both the cleavage planes and strength

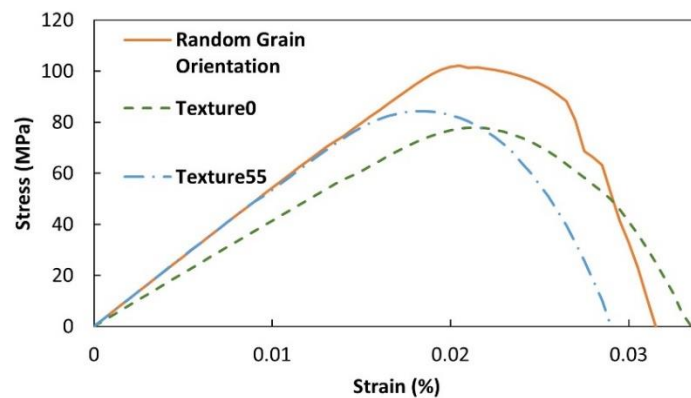


Figure 2.14 Comparison of stress-strain curves of polycrystalline models with random grain orientations, Texture0, and Texture55.

## 2.10 Conclusion

A modified phase-field model was presented to study crack propagation and mechanical response in polycrystalline brittle materials. The fracture surface energy and strength in GBs were considered to be a function of the misorientation angle of the neighboring grains. An equation similar to the modified Read-Shockley model was used, where a larger GB misorientation leads to a lower fracture surface energy and strength in the GB compared to the grain interiors.

Bi-crystal simulations showed the effect of fracture surface energy, cleavage planes, and strength on the crack path. When cleavage planes were considered, crack propagated along those planes in each grain. Also, the results illustrated that lower fracture surface energy and strength in GBs promote intergranular fracture. Likewise, bi-crystal results showed that the presented model yields a reasonable mechanical response which cannot be obtained by other models. Polycrystalline results illustrated that the model is able to predict the experimentally observed of the combination of intergranular and transgranular crack in polycrystalline brittle materials, where the transgranular cracks propagate along predefined cleavage planes in each grain. In addition, similar to results of bi-crystal model, polycrystalline results showed that model effectively takes the strength into account on the predicting crack path and mechanical response.

In summary, the proposed model includes the fracture surface energy, cleavage plane direction and material strength in its formulations, providing a more quantitative phase-field model for crack propagation in polycrystalline materials. Also, this model is more flexible compared to other models to be calibrated based on experimental results. The presented model can be used to design grain and GB structure and topology to control crack propagation and fracture toughness of polycrystalline materials.

## 2.11 Appendix A - Derivation of Parameter B

Before deriving parameter  $B$ , we need to calculate the crack width and critical stress.

According to Clayton and Knap [71], the crack surface energy is:

$$\gamma(\phi, \nabla\phi, \omega) = \frac{1}{2k} + \frac{k}{2} \omega : (\nabla\phi \otimes \nabla\phi) ; \quad \omega = \mathbf{I} + \alpha(\mathbf{I} - \mathbf{M} \otimes \mathbf{M}), \quad (2.18)$$

where  $\mathbf{M}$  is the unit vector normal to the preferential cleavage planes. For example, if the cleavage plane is oriented  $\varphi$  degree counterclockwise with respect to  $x$  axis (horizontal axis) in the Cartesian coordinates, the vector  $\mathbf{M}$  is:  $-\sin(\varphi)\mathbf{i} + \cos(\varphi)\mathbf{j}$ . In addition,  $\alpha > 1$  is used to prevent crack from propagating on planes not normal to  $\mathbf{M}$ . The variational derivative of the crack density function is:

$$\delta\gamma = \frac{\phi}{k} - k[\nabla^2\phi + \alpha(\nabla^2\phi - \mathbf{M} \otimes \mathbf{M} : \nabla\nabla\phi)] \quad (2.19)$$

The expansion of Eq.(2.19) results in:

$$\begin{aligned} \delta\gamma = \frac{\phi}{k} - k & \left[ \frac{\partial^2\phi}{\partial x^2} + \frac{\partial^2\phi}{\partial y^2} + \alpha \left( \frac{\partial^2\phi}{\partial x^2} + \frac{\partial^2\phi}{\partial y^2} - \cos^2\left(\frac{\pi}{2} + \theta\right) \frac{\partial^2\phi}{\partial x^2} \right. \right. \\ & \left. \left. - 2 \cos\left(\frac{\pi}{2} + \theta\right) \sin\left(\frac{\pi}{2} + \theta\right) \frac{\partial^2\phi}{\partial xy} - \sin^2\left(\frac{\pi}{2} + \theta\right) \frac{\partial^2\phi}{\partial y^2} \right]. \end{aligned} \quad (2.20)$$

Following the approach introduced in [66], we can obtain the profile of crack in one dimension:

$$\phi(x) = e^{-\frac{|x|}{k\sqrt{1+a(1-\cos^2(\frac{\pi}{2}+\varphi))}}} \quad (2.21)$$

When plotting  $\phi(x)$ , the tangential lines at  $x=0$  ( $\phi = 1$ ) intercept the  $x$  axis (horizontal axis) in the Cartesian coordinates at:

$$\pm k\sqrt{1+a(1-\cos^2(\frac{\pi}{2}+\varphi))} \quad (2.22)$$

So, the crack width can be defined as:

$$2k\sqrt{1+a(1-\cos^2(\frac{\pi}{2}+\varphi))} \quad (2.23)$$

Similar to Emdadi et al. [52], we multiply  $\sqrt{B}$  to the elastic strain. Therefore, the equilibrium equation of  $\phi$ , Eq. (2.9) in this paper, becomes:

$$g(\phi)'F_e(\boldsymbol{\varepsilon}(\mathbf{u})) - \frac{G_c}{B} \left( \frac{\phi}{k} - k[\nabla^2 \phi + a(\nabla^2 \phi - \mathbf{M} \otimes \mathbf{M} : \nabla \nabla \phi)] \right) = 0. \quad (2.24)$$

Following the approach in [52], we define the average crack surface energy as:

$$\frac{G_c}{2Bk \sqrt{1 + a(1 - \cos^2(\frac{\pi}{2} + \varphi))}} \quad (2.25)$$

Therefore, by imposing the condition that for each  $k$ , the average crack surface energy is equal to  $\frac{G_c}{2k^*}$ , and the parameter  $B$  becomes:

$$B = \frac{\sqrt{1 + a(1 - \cos^2(\frac{\pi}{2} + \varphi))} k^*}{k}, \quad (2.26)$$

where parameter  $k^*$  is obtained through equating the maximum stress in front of crack tip to the material strength [79, 80].

CHAPTER 3  
INTERACTIVE EVOLUTION BETWEEN CRACK PROPAGATION AND  
MARTENSITIC PHASE TRANSFORMATION

Reproduced from A. Lotfolahpour, W. Huber, and M. Asle Zaeem, “*A phase-field model for interactive evolution of phase transformation and cracking in superelastic shape memory ceramics*”, Computational Materials Science 216 (2023): 111844.

### 3.1 Abstract

This work presents a modified phase-field model for accurate coupling of phase transformation and cracking in shape memory ceramics. The existing phase-field models underestimate the elastic response at the beginning of the mechanical response. We modified the chemical free energy to control the rate of phase transformation and consequently obtain a physical elastic response before initiation of phase transformation. First, the forward and reverse martensitic phase transformation in a super-elastic single crystal 3mol% yttria-stabilized tetragonal zirconia is studied. Then, the interaction between phase transformation and fracture under displacement-controlled loading condition is investigated. The model predicts a realistic mechanical response and the experimentally observed microstructure and crack deflection due to the phase transformation. In addition, the model captures the reverse phase transformation and the stress drop due to the crack propagation.

Shape memory ceramics (SMCs) have various applications in the biomedical and aerospace industries [1]. One of the main characteristics of SMCs is their recoverable stress/temperature-induced solid-state martensitic phase transformation (MPT), which results in strain recovery. Based on the temperature of the material, two different behaviors can be observed: super-elasticity (SE) (also known as pseudoelasticity) or the shape memory effect (SME) (also known as pseudoplasticity). If the temperature is higher than the equilibrium transformation temperature, SE is observed. In SE behavior, the strain is fully recovered when

the load is removed, and a stress-strain hysteresis loop is obtained [16, 31, 97]. If the temperature is lower than the equilibrium transformation temperature, the SME is observed. In SME, after removing the load there is a large residual strain and a temperature higher than the equilibrium temperature is required to recover the original shape and phase of the material [16, 31, 97-99].

The main ingredient of SMCs is often zirconia. Zirconia-based ceramics have high strength, high operating temperature, and high corrosion resistance which make these ceramics suitable for extreme operating conditions. In addition, they show promising SME and SE behaviors due to stress or temperature induced recoverable phase transformation between their tetragonal (T) and monoclinic (M) phases ( $T \leftrightarrow M$ ). However, because these phases are brittle, zirconia-based ceramics have a low fracture toughness. In addition,  $T \rightarrow M$  phase transformation causes inelastic dilatation, which contributes to low SME and SE fatigue life in SMCs [18].

Since the overall mechanical properties and fracture behavior of materials is strongly affected by their microstructure, studying microstructure evolution and fracture at the microscopic length scale is essential to obtain an accurate estimate of durability of structures. There are a few experimental works on zirconia ceramics to study the microstructural evolution [5, 11] and interaction between crack and phase transformation [100] in order to study and improve the fracture and overall mechanical properties of SMCs. In addition to requiring a considerable amount of materials, testing time and cost, experiments are unable to fully capture the interactions between cracking and phase transformation in ceramics, because both happen at a very high pace. Therefore, numerical studies could be suitable alternatives to study such interactions.

Phase-field (PF) modeling stands out as a powerful numerical approach for simulating MPT [31]. In the PF approach, the product of a phase transformation is represented by a scalar

called an order parameter (OP). In addition, the PF approach has been widely applied as a powerful and robust approach for modeling fracture in brittle [47, 80, 101, 102] and ductile materials [50, 103] where an OP represents the crack surface.

Based on experimental observations, when phase transformation occurs in shape memory materials, the strain localization produces a twinned-martensite (strip-like microstructure) microstructure of alternating austenite-martensite or martensite-martensite variants [13, 104]. To obtain a reliable mechanical response and experimentally observed microstructures, one must choose an appropriate chemical free energy in the total free energy functional of the PF model of MPT. The chemical free energy represents the energy dissipation due to MPT, and 2-3-4 and 2-4-6 polynomials are commonly used in the literature for first order transformations [31]. Depending on the parameters of the polynomial, the shape of chemical free energy can be either double-well, concave, or convex. In addition to the chemical free energy, the relationship between the OPs and the stress-free strain tensor (or OP-strain relation) plays an important role in prediction of the mechanical response.

Mamivand et al. [14] were the first to develop a PF model for T→M phase transformation in single crystal zirconia under stress-controlled loading conditions. They used a 2-4-6 polynomial and a quadratic OP-strain relation. They validated their simulated microstructure against experimental results. In another work, Mamivand et al. [105] used a similar model and studied both SE and SME in a polycrystalline zirconia under a stress-controlled loading condition; they showed that the obtained twinned-martensite microstructure and mechanical response were consistent with experiments. Recently, Cisse and Asle Zaeem [16] developed a non-isothermal elastoplastic PF model considering 2-4-6 and a quadratic OP-strain relation to study the SE and SME in both single crystal and polycrystalline 3mol% yttria-stabilized

tetragonal zirconia (3Y-STZ) under stress-controlled loading conditions. In [106], the authors used a 2-3-4 polynomial and a linear OP-strain relationship to study the ferroelastic domain switching in a zirconia crystal in the presence of crack propagation which was qualitatively compared to experimental observations. A combination of the linear OP-strain relation with 2-3-4 or 2-4-6 polynomials has also been used for modeling MPT in other shape memory materials like NiTi [40, 107-110].

Based on the aforementioned research works, linear or quadratic OP-strain relation has been used in PF models for simulating the MPT in SMCs and shape memory alloys. But we will show in Sec.3.5 of this paper that under some circumstances the quadratic OP-strain relation loses its generality and validity. We will discuss the advantage and this advantage of linear and quadratic OP-strain relations in Sec.3.5 and explain why the linear OP-strain relation is used in this paper. It is also important note that PF models of MPT underestimate the elastic modulus in the initial part of the stress-strain response regardless of the choice of the OP-strain relation or the chemical free energy polynomial; we will also address this shortcoming of the current PF models in this work.

There are only limited studies to investigate the interactions of MPT and cracking in SMCs. Zhao et al. [21] studied this interaction in single crystal zirconia under a displacement controlled loading condition using PF method. They considered a chemical free energy polynomial that simulates SME. Although they obtained a twinned-martensite microstructure as a result of the SME chemical free energy polynomial, they did not report the mechanical response in the form of a stress-strain curve, and it is not expected that the employed formulations generate a reasonable mechanical response. Zhu and Lao [20] used the same PF

model in [21] to study phase transformation and fracture in polycrystalline zirconia. Their work lacked prediction of mechanical response as well.

Moshkelgosha et al. studied fracture propagation in single crystal zirconia [22] and separately in polycrystalline zirconia [23] adopting a chemical free energy polynomial that simulates SME. They applied a stress-controlled loading condition. Although they obtained experimentally observed twinned-martensite microstructures, their mechanical response did show any drop in the stress-strain curve when crack initiated and propagated. Also, they predicted a maximum strain of at least 5.5% for single crystal and 12% for polycrystalline before fracture is fully developed, which is unphysical. This is an indication that stress-controlled loading is not appropriate to simulate fracture. In a different study by the same authors [24], they studied phase transformation and fracture in a 3D single crystal zirconia by applying a displacement-controlled loading, however, they did not show any drop in the stress-strain curve after crack initiation and propagation. Also, their maximum reported strain under uniaxial tension was 15%, while the experimental work by Lai et al. [5] reported a maximum bending strain of 8%. Therefore, it is expected that a specimen under uniaxial tension fails at a lower strain.

Generally, since most of the experimental studies for determining the mechanical properties are under displacement-controlled loading conditions [111-119], the numerical results obtained under stress-controlled loading cannot be compared and validated with experiments. Especially, when the goal is to study crack propagation in a continuum model, quasi-static stress-controlled loading cannot be used, because when the crack propagation starts, the stress-controlled loading causes unbounded displacement and the final drop in the mechanical response cannot be obtained by the stress-controlled loading conditions [120].

Based on the above literature review, we can conclude that none of the current models can properly simulate the coupled phase transformation and fracture in SMCs and produce acceptable microstructures and stress-strain curves under displacement-controlled loading conditions. In this paper, first, we examine the double well, concave, and convex chemical energies, to determine which functional form produces the most accurate predictions of microstructure and mechanical response. Then, we propose a solution to the under-prediction of the elastic modulus observed in PF simulations of SE. Finally, we show that, with the proposed modification, accurate predictions of the interaction between MPT and fracture can be made using the PF approach.

### 3.2 Coupling PT and fracture in PF context

We use OPs noted as  $\eta_p$  to describe the state of  $p^{\text{th}}$  monoclinic variants. The  $\eta_p$  varies between 0 to 1, and  $\eta_p = 1$  means the  $p^{\text{th}}$  monoclinic variant exists and when  $\eta_p = 0$ , the other monoclinic variants or the tetragonal phase exist. To derive the governing equations for MPT, first we need to construct the total free energy of the system ( $F_{\text{tot}}$ ):

$$F_{\text{tot}}(u_i, \eta_1, \eta_2, \dots, \eta_m) = F_{\text{el}} + F_{\text{ch}} + F_{\text{gd}}, \quad (3.1)$$

where  $F_{\text{el}}$  is elastic strain energy density,  $F_{\text{ch}}$  is chemical free energy, and  $F_{\text{gd}}$  is gradient energy of the tetragonal- monoclinic or monoclinic-monoclinic phases. In the following, each of these energies is explained in detail.

#### 3.2.1 Elastic strain energy ( $F_{\text{el}}$ )

The elastic strain energy can be written as:

$$F_{\text{el}}(u_i) = \int_V \frac{1}{2} C_{ijkl} \varepsilon_{kl}^{\text{el}} \varepsilon_{ij}^{\text{el}} dV, \quad (3.2)$$

where  $V$  is the domain volume,  $u_i$  is the displacement,  $C_{ijkl}$  is the elastic tensor and  $\varepsilon_{ij}^{\text{el}}$  is the elastic strain which is defined as the difference between total strain ( $\varepsilon_{ij}^{\text{tot}}$ ) and the transformation strain ( $\varepsilon_{ij}^{\text{tr}}$ ):

$$\varepsilon_{ij}^{\text{el}} = \varepsilon_{ij}^{\text{tot}} - \varepsilon_{ij}^{\text{tr}}, \quad (3.3)$$

where considering the linear OP-strain relation [107, 109, 121],  $\varepsilon_{ij}^{\text{tr}}$  is defined as:

$$\varepsilon_{ij}^{\text{tr}} = \sum_{p=1}^m \varepsilon_{ij}^{00}(p) \eta_p, \quad (3.4)$$

where  $\varepsilon_{ij}^{00}$  is the stress-free strain tensor which represents the change in microstructure between parent and product phases [16]. It should be noted that in this paper, the small strain assumption ( $\varepsilon_{ij}^{\text{tot}} = \frac{1}{2} (u_{i,j} + u_{j,i})$ ), is considered. We use the linear relation, and the reason is explained in Sec. 3.5 based on comparing these two forms of OP-strain relation.

The elastic constant difference between tetragonal and monoclinic phases is represented by the following relation [16]:

$$C_{ijkl}(\eta_1, \eta_2, \dots, \eta_m) = C_{ijkl}^{\text{T}} + \sum_{p=1}^m \eta_p (C_{ijkl}^{\text{M}} - C_{ijkl}^{\text{T}}), \quad (3.5)$$

where  $C_{ijkl}^{\text{T}}$  and  $C_{ijkl}^{\text{M}}$  are elastic constants of the tetragonal and monoclinic phases, respectively.

The elastic energy defined in Eq.(3.2) is based on Hooke's law and thus, the stress tensor is related to elastic strain tensor through the following equation:

$$\sigma_{ij}(u_i) = C_{ijkl}(\eta_1, \eta_2, \dots, \eta_m) \varepsilon_{kl}^{\text{el}}, \quad (3.6)$$

### 3.2.2 Chemical free energy ( $F_{\text{ch}}$ )

The  $F_{\text{ch}}$  drives the MPT and the shape of this energy plays an important role in predicting the mechanical response and microstructure. The 2-3-4 or 2-4-6 Landau polynomials defined in terms of OPs are the most common types of  $F_{\text{ch}}$  used in the literature. Wen et al. [122] explained that the particular order of the Landau polynomial does not have a significant effect on the predicted microstructure. Therefore, we use the 2-3-4 Landau polynomial:

$$F_{\text{ch}}(\eta_1, \eta_2, \dots, \eta_m) = \int_V \Delta G \left( a \sum_{p=1}^m \eta_p^2 - b \sum_{p=1}^m \eta_p^3 + c \left( \sum_{p=1}^m \eta_p^2 \right)^2 \right) dV, \quad (3.7)$$

where  $\Delta G$  is the chemical driving force which is the difference in the specific  $F_{\text{ch}}$  between the parent and the product. According to [16, 123], the following equation can be used to calculate  $\Delta G$  for 3Y-STZ at different temperatures:

$$\Delta G(t \rightarrow m) = -6159.18 + 6.98T, \quad (3.8)$$

where the energy is in  $\text{Jmol}^{-1}$  (or  $\text{Jm}^{-3}$ ) and the temperature ( $T$ ) is in Kelvin (K).

In Eq. (3.7)  $a$ ,  $b$ , and  $c$  are coefficients that should be chosen in a way that maintains the value of the interfacial energy within the physical reasonable range and yields  $F_{\text{ch}} = \Delta G(t \rightarrow m)$  at  $\eta_p = 1$ . In addition, the values of these parameters determine the shape of  $F_{\text{ch}}$ . Although a variety of shapes can be obtained through tuning expansion coefficients, the double-well, concave, convex have been used in the literature for modeling SE behavior. In Sec.3.7.1, we will study the difference between these three types of  $F_{\text{ch}}$  in terms of mechanical response and microstructure for modeling SE behavior in a single crystal 3Y-STZ sample.

### 3.2.3 Gradient free energy

Gradient free energy represents the interfacial energy between tetragonal-monoclinic or monoclinic-monoclinic phases and ensures a non-abrupt transition between different phases. It is defined as:

$$F_{\text{gd}}(\eta_1, \eta_2, \dots, \eta_m) = \int_V \frac{\beta_{ij}}{2} \sum_{p=1}^m \nabla_i \eta_p \nabla_j \eta_p dV, \quad (3.9)$$

where  $\nabla$  is the gradient operator and  $\beta_{ij}$  is gradient energy tensor. We assume that the gradient energy coefficient is isotropic ( $\beta_{ij} = \beta \delta_{ij}$ ) [16]. Therefore the Eq.(3.9) will be:

$$F_{\text{gd}}(\eta_1, \eta_2, \dots, \eta_m) = \int_V \frac{\beta}{2} \sum_{p=1}^m (\nabla \eta_p)^2 dV. \quad (3.10)$$

### 3.3 Coupling MPT with fracture

We use  $\phi$  as the OP of fracture, and when  $\phi = 1$  the crack is fully developed and when  $\phi = 0$  the material is undamaged. In order to couple MPT with PF fracture, we modify the total free energy of the system by adding the fracture energy ( $F_{\text{fr}}$ ) and degrading the elastic constants based on the evolution of fracture through multiplying it by a degradation function,  $g(\phi)$ . These modifications lead to:

$$F_{\text{tot}}(u_i, \eta_1, \eta_2, \dots, \eta_m, \phi) = F_{\text{el}} + F_{\text{ch}} + F_{\text{gd}} + F_{\text{fr}}, \quad (3.11)$$

where  $F_{\text{fr}}$  is defined as [65]:

$$F_{\text{fr}}(\phi) = \int_V G_c \left( \frac{\phi^2}{2k} + \frac{k}{2} |\nabla \phi|^2 \right) dV, \quad (3.12)$$

where  $G_c$  is the fracture surface energy in Griffith's theory, and  $k$  is a positive regularization parameter with the dimension of length to regulate the width of the crack phase field.

In addition, to accommodate the crack phase field,  $F_{\text{el}}$  is redefined as:

$$F_{\text{el}}(u_i, \phi) = \int_V \frac{1}{2} g(\phi) C_{ijkl}(\eta_1, \eta_2, \dots, \eta_m) \varepsilon_{kl}^{\text{el}} \varepsilon_{ij}^{\text{el}} dV, \quad (3.13)$$

where  $g(\phi)$  is the degradation function and  $g(\phi) = (1 - \phi)^2$  is one of the widely used degradation functions [74, 77] that we use in this paper as well. Also, based on Eq.(3.13), the stress tensor (Eq.(3.6)) will change to:

$$\sigma_{ij}(u_i, \phi) = g(\phi) C_{ijkl}(\eta_1, \eta_2, \dots, \eta_m) \varepsilon_{kl}^{\text{el}}. \quad (3.14)$$

We use the method proposed by Miehe et al. [81] to ensure irreversibility of crack (crack healing prevention):

$$F_{\text{el}}(u_i, t) = \max F_{\text{el}}(u_i, s), \quad s \in [0, t]. \quad (3.15)$$

### 3.4 Governing equations

The evolution of both MPT and PF fracture can be obtained through Ginzburg-Landau equation [124, 125]. This equation relates the rate of each OP to the variational derivative of total free energy with respect to the same OP. Using Ginzburg-Landau equation for MPT leads to the following equation:

$$\frac{\partial \eta_p}{\partial t} = L \left( \frac{\delta F_{\text{tot}}}{\delta \eta_p} \right) = L \left( \frac{\delta F_{\text{el}}}{\delta \eta_p} + \frac{\delta F_{\text{ch}}}{\delta \eta_p} + \frac{\delta F_{\text{gd}}}{\delta \eta_p} + \frac{\delta F_{\text{fr}}}{\delta \eta_p} \right), \quad (3.16)$$

where  $L$  is the kinetic coefficient, and:

$$\begin{aligned} \frac{\delta F_{\text{el}}}{\delta \eta_p} = & \frac{1}{2} g(\phi) \varepsilon_{ij}^{\text{el}} (C_{ijkl}^{\text{M}} - C_{ijkl}^{\text{T}}) \varepsilon_{kl}^{\text{el}} - \frac{1}{2} g(\phi) C_{ijkl}(\eta_1, \eta_2, \dots, \eta_m) \varepsilon_{kl}^{\text{el}}(p) \varepsilon_{ij}^{\text{el}} \\ & - \frac{1}{2} g(\phi) C_{ijkl}(\eta_1, \eta_2, \dots, \eta_m) \varepsilon_{ij}^{\text{el}}(p) \varepsilon_{kl}^{\text{el}}, \end{aligned} \quad (3.17)$$

$$\frac{\delta F_{\text{ch}}}{\delta \eta_p} = \Delta G(2a\eta_p - 3b\eta_p^2 + 4c\eta_p \sum_{p=1}^m \eta_p^2), \quad (3.18)$$

$$\frac{\delta F_{\text{gd}}}{\delta \eta_p} = -\beta \nabla^2 \eta_p, \quad (3.19)$$

$$\frac{\delta F_{\text{fr}}}{\delta \eta_p} = 0. \quad (3.20)$$

Also, using the Ginzburg-Landau equation for PF fracture leads to:

$$\frac{\partial \phi}{\partial t} = M \left( \frac{\delta F_{\text{tot}}}{\delta \phi} \right) = M \left( \frac{\delta F_{\text{el}}}{\delta \phi} + \frac{\delta F_{\text{ch}}}{\delta \phi} + \frac{\delta F_{\text{gd}}}{\delta \phi} + \frac{\delta F_{\text{fr}}}{\delta \phi} \right), \quad (3.21)$$

where  $M$  is called the fracture mobility coefficient, and:

$$\frac{\delta F_{\text{el}}}{\delta \phi} = -(1 - \phi) C_{ijkl}(\eta_1, \eta_2, \dots, \eta_m) \varepsilon_{kl}^{\text{el}} \varepsilon_{ij}^{\text{el}}, \quad (3.22)$$

$$\frac{\delta F_{\text{ch}}}{\delta \phi} = 0, \quad (3.23)$$

$$\frac{\delta F_{\text{gd}}}{\delta \phi} = 0, \quad (3.24)$$

$$\frac{\delta F_{\text{fr}}}{\delta \phi} = G_c \left( \frac{\phi}{k} - k \nabla^2 \phi \right). \quad (3.25)$$

Examination of Eq.(3.3) and Eq.(3.17) reveals that MPT can have a blunting effect on the crack initiation and propagation through reducing the available elastic energy. Meanwhile, based on Eq.(3.22), fracture halts the propagation of MPT by reducing elastic strain energy in the cracked regions ( $\phi > 0$ ).

In addition, by neglecting the body forces, the equilibrium equations become:

$$\text{div } \boldsymbol{\sigma}(u_i, \phi) = 0. \quad (3.26)$$

### 3.5 The difference between linear and quadratic OP-strain relations

As it was mentioned before, in this paper we use the linear OP-strain relation. We chose the linear relation over the quadratic relation because the quadratic relation can become invalid in some situations explained below.

Using the linear relation, the OPs' evolution equation (Eq.(3.16)) without considering the effect of fracture, will become:

$$\begin{aligned} \frac{\partial \eta_p}{\partial t} = L & \left( \frac{1}{2} \varepsilon_{ij}^{\text{el}} (C_{ijkl}^{\text{M}} - C_{ijkl}^{\text{T}}) \varepsilon_{kl}^{\text{el}} - \frac{1}{2} C_{ijkl}(\eta_1, \eta_2, \dots, \eta_m) \varepsilon_{kl}^{\text{el}}(p) \varepsilon_{ij}^{\text{el}} \right. \\ & - \frac{1}{2} C_{ijkl}(\eta_1, \eta_2, \dots, \eta_m) \varepsilon_{ij}^{\text{el}}(p) \varepsilon_{kl}^{\text{el}} + \Delta G(2a\eta_p - 3b\eta_p^2 + 4c\eta_p \sum_{p=1}^m \eta_p^2) \\ & \left. - \beta \nabla^2 \eta_p \right). \end{aligned} \quad (3.27)$$

The quadratic relation ( $\varepsilon_{ij}^{\text{tr}} = \sum_{p=1}^m \varepsilon_{ij}^{\text{el}}(p) \eta_p^2$ ) leads to the following equation for the OPs' evolution:

$$\begin{aligned} \frac{\partial \eta_p}{\partial t} = L & \left( \frac{1}{2} \varepsilon_{ij}^{\text{el}} (C_{ijkl}^{\text{M}} - C_{ijkl}^{\text{T}}) \varepsilon_{kl}^{\text{el}} \right. \\ & - \eta_p C_{ijkl}(\eta_1, \eta_2, \dots, \eta_m) \varepsilon_{kl}^{\text{el}}(p) \varepsilon_{ij}^{\text{el}} - \eta_p C_{ijkl}(\eta_1, \eta_2, \dots, \eta_m) \varepsilon_{ij}^{\text{el}}(p) \varepsilon_{kl}^{\text{el}} \\ & \left. + \Delta G(2a\eta_p - 3b\eta_p^2 + 4c\eta_p \sum_{p=1}^m \eta_p^2) - \beta \nabla^2 \eta_p \right). \end{aligned} \quad (3.28)$$

In Eq.(3.28), all terms except the first term are zero when the initial value of  $\eta_p = 0$ . Then if  $(C_{ijkl}^{\text{M}} - C_{ijkl}^{\text{T}})$  is zero (e.g. if MPT in polycrystalline samples [107] or if ferroelastic domain switching [106] is studied) Eq.(3.28) becomes zero and consequently  $\eta_p$  never grows. Therefore, Eq.(3.28) loses its generality and validity and cannot accurately predict MPT. This problem does not occur when the linear OP-strain relation is considered since the second term in

Eq.(3.27) is not zero and starts to increase upon the start of loading and never loses its generality and validity. Therefore, we use the linear OP-strain relation in this paper.

### **3.6 Solution scheme**

The governing equations presented in the previous section are solved in a finite element framework using the solid mechanics and mathematics modulus of COMSOL Multiphysics. All simulations are under displacement-controlled loading, and the boundary conditions and sample dimensions are shown in Figure 3.1a. Also, Figure 3.1b shows the applied displacement versus time. Furthermore, the plane stress condition is considered in all 2D simulations.

For all models, with and without fracture, quadrilateral elements are generated by the mapped mesh algorithm feature in COMSOL. A mesh study was conducted where we found that a mesh size of  $0.04 \mu\text{m}$  (or 2500 quadrilateral elements in the domain) were sufficient to resolve the interface of different phases. Discretizing the sample with more elements did not change the microstructure and mechanical response, therefore we used 2500 quadrilateral elements. The displacements are solved using “Solid Mechanics” module with quadratic shape functions. The crack PF and Martensite PF are solved using the “General Form PDE” module of COMSOL with linear shape functions. The staggered [126] scheme is used to solve the governing equations where nonlinear sub-problems are solved with Newton’s method. The time step of  $0.01\text{s}$  is used for all simulations.

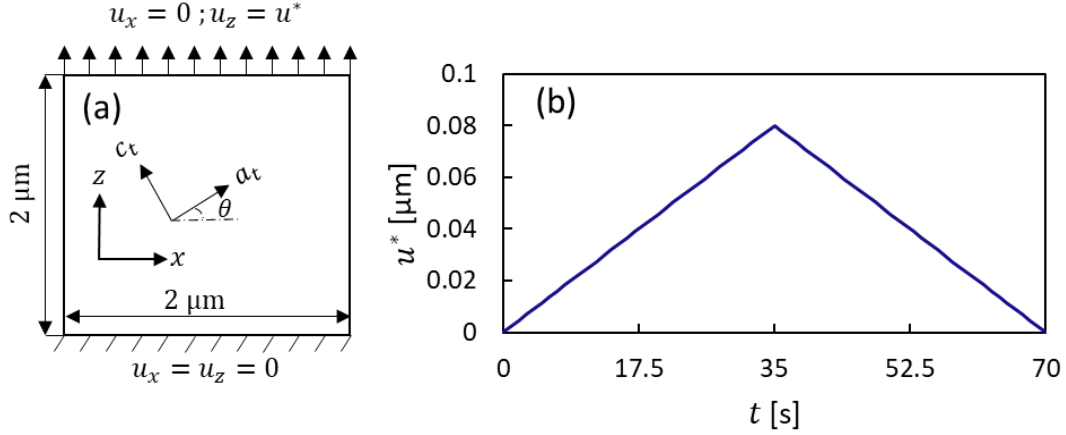


Figure 3.1 a) Dimensions and boundary conditions, and b) Applied displacement versus time for simulating forward and reverse transformation without fracture. x- axis represents  $a_t$  direction and z axis represent  $c_t$  of the tetragonal phase.

### 3.7 Results and Discussion

#### 3.7.1 Comparison of different $F_{ch}$ for modeling SE in 3Y-STZ

In this section, we compare three different forms of  $F_{ch}$  (double-well, concave and convex) for modeling SE in a 2D idealization of a 3Y-STZ single crystal sample without considering fracture. Table shows the values of  $a$ ,  $b$ , and  $c$  for each  $F_{ch}$ . These parameters are determined to ensure each  $F_{ch}$  has a minimum at  $\eta = 0$ . For the double-well case, the energy has a local minimum at  $\eta = 1$  as well. Also, in all three  $F_{ch}$ ,  $\Delta G$  (in Eq.(3.7)) is  $\sim 156 \text{ Jmol}^{-1}$  ( $7.2 \times 10^6 \text{ Jm}^{-3}$ ) which is obtained by Eq.(3.8) considering the temperature is constant at 905 K. This temperature is higher than the reported equilibrium temperature of 883 K for 3Y-STZ [16, 127, 128], therefore, the system will show SE behavior (i.e., strain recovery occurs after unloading without a need for increasing the temperature). Figure 3.2 shows the plot of these three forms of  $F_{ch}$ .

Table 3.1 Coefficients of different chemical free energies.

Coefficient	Double-Well	Concave	Convex
$a$	13.89	9.2	3.13
$b$	23.75	12.89	4.01
$c$	10.78	4.74	1.85

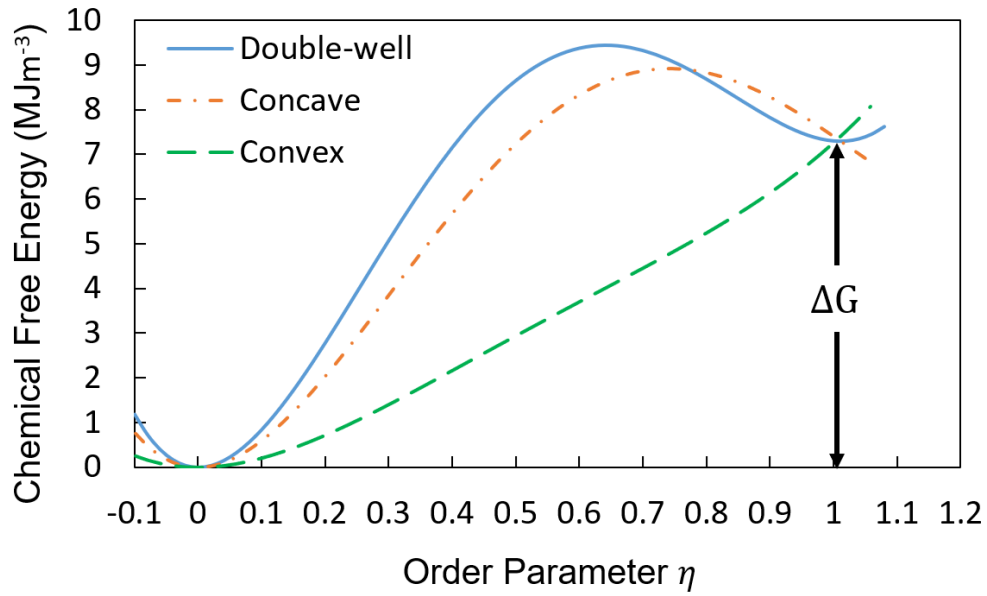


Figure 3.2 Three different  $F_{ch}$  used for modeling SE.

Eq.(3.29) and Eq.(3.30) show the stiffness tensor of tetragonal [129, 130] and monoclinic [130], respectively. In addition, two monoclinic variants exist in the  $a - c$  plane, and their stress-free strain tensors are given in Eq.(3.31) and Eq.(3.32) [14].

$$C_{ijkl}^T = \begin{bmatrix} 361 & 100 & 62 & 0 & 0 & 0 \\ 100 & 361 & 62 & 0 & 0 & 0 \\ 62 & 62 & 264 & 0 & 0 & 0 \\ 0 & 0 & 0 & 59 & 0 & 0 \\ 0 & 0 & 0 & 0 & 59 & 0 \\ 0 & 0 & 0 & 0 & 0 & 64 \end{bmatrix} \text{GPa}, \quad (3.29)$$

$$\mathbf{C}_{ijkl}^M = \begin{bmatrix} 327 & 142 & 55 & 0 & 0 & -21 \\ 142 & 408 & 196 & 0 & 0 & 31 \\ 55 & 196 & 258 & 0 & 0 & -18 \\ 0 & 0 & 0 & 100 & -23 & 0 \\ 0 & 0 & 0 & -23 & 81 & 0 \\ -21 & 31 & -18 & 0 & 0 & 126 \end{bmatrix} \text{GPa}, \quad (3.30)$$

$$\varepsilon_{ij}^{00}(1) = \begin{bmatrix} 0.0049 & -0.0761 \\ -0.0761 & 0.0180 \end{bmatrix}, \quad (3.31)$$

$$\varepsilon_{ij}^{00}(2) = \begin{bmatrix} 0.0049 & 0.0761 \\ 0.0761 & 0.0180 \end{bmatrix}. \quad (3.32)$$

We consider the global coordinates when  $\theta = 0^\circ$ , to be aligned with those of the tetragonal phase where x- axis represents  $a_t$  direction and z axis represents  $c_t$  (see Figure 3.1a) and  $\theta = 0^\circ$  corresponds to [001] oriented crystal. The stress-free strain tensor and elastic stiffness tensor are transferred to the global coordinate system using the following rotation operations:

$$\varepsilon_{ij}^{G00}(p) = R_{ik}R_{jl}\varepsilon_{ij}^{00}(p), \quad (3.33)$$

$$C_{ijkl}^G = R_{im}R_{jn}R_{ko}R_{lp}C_{mnop}, \quad (3.34)$$

where  $\varepsilon_{ij}^{00}(p)$  and  $C_{mnop}$  are, respectively, the stress-free strain tensor and the elastic stiffness matrix in the local coordinate system.  $R_{ij}$  is the rotation matrix for a grain with an orientation angle of  $\theta$ , which in 2D is defined as:

$$R_{ij} = \begin{bmatrix} \cos(\theta) & \sin(\theta) \\ -\sin(\theta) & \cos(\theta) \end{bmatrix}. \quad (3.35)$$

$\theta$  measures positive counterclockwise. Table shows all other parameters used for running the simulations. It is worth mentioning, the kinetic coefficient ( $L$ ) in Eq.(3.16) can be arbitrary selected since there is not a report on the speed of PT in zirconia-based ceramics [105]

and a wide range value from  $2 \times 10^{-9} \frac{\text{m}^3}{\text{Js}}$  [22-24] to  $10 \frac{\text{m}^3}{\text{Js}}$  [16] has been used in the literature. In this paper we choose this value to be  $5 \times 10^{-8} \frac{\text{m}^3}{\text{Js}}$ . The gradient energy coefficient ( $\beta$ ) in Eq.(3.19) must be selected such that gives a reasonable interface thickness (few nanometers) [105, 131], we chose  $\beta = 1 \times 10^{-9} \frac{\text{J}}{\text{m}}$  and based on the our results gives a reasonable interface thickness between different phases. Furthermore, the initial values of  $\eta_p$  are set to  $10^{-6}$  to overcome the possibility of numerical artifacts. In addition, considering the crack length scale parameter ( $k$ ) in Eq.(3.12) to be 20 nm which is one percent of the domain length, is small enough to obtain a stable solution, a correct crack path, and an admissible diffusive area with a reasonable accuracy and computing cost [52, 79, 132].

Table 3.2 Simulation parameters.

Parameter	Value
Kinetic coefficient, $L$	$5 \times 10^{-8} \frac{\text{m}^3}{\text{Js}}$
Gradient energy coefficient, $\beta$	$1 \times 10^{-9} \frac{\text{J}}{\text{m}}$
Mobility coefficient, $M$ [52, 132]	$1 \frac{\text{m}^3}{\text{Js}}$
Critical energy release rate, $G_c$ [133]	$24 \frac{\text{J}}{\text{m}^2}$
Crack length scale parameter, $k$	20 nm

Figure 3.3 (I), (II), and (III) show the mechanical response and microstructure for [001] oriented sample predicted by convex, concave, and double-well  $F_{\text{ch}}$ , respectively. In Figure 3.3, the expression of  $\eta_1 + 2\eta_2$  is used to show the transformed regions, and if this expression is equal to 0, no transformation has occurred and the tetragonal phase exists, if this expression is 1, the first variant of the monoclinic phase exists, and if it is equal to 2, the second variant of the monoclinic phase exists. In addition, the stress and strain in the stress-strain curve are calculated

based on the reaction force and the displacement at the top edge of sample. Based on these figures both double-well and concave predict the experimentally observed twinned-martensite microstructure. However, the convex  $F_{ch}$  is not able to predict such a twinned-martensite microstructure, therefore it is not a proper  $F_{ch}$  for modeling microstructures of shape memory materials. There are several works, such the MPT model used by Simoes and Martínez-Pañeda [97] for simulating fracture in shape memory materials, that used a convex potential energy, which are unable to properly predict microstructures in shape memory materials and are appropriate for macroscopic length scales. The microstructures predicted by the concave  $F_{ch}$  is consistent with previously reported results, such as those reported by Esfahani et al. for SE in NiTi alloys [54]. Although, both double-well and concave  $F_{ch}$  predict admissible microstructures and mechanical response, we proceed with the double-well  $F_{ch}$  because it grants stability at both parent and product phases through having minima at both  $\eta_p = 0$  and 1.

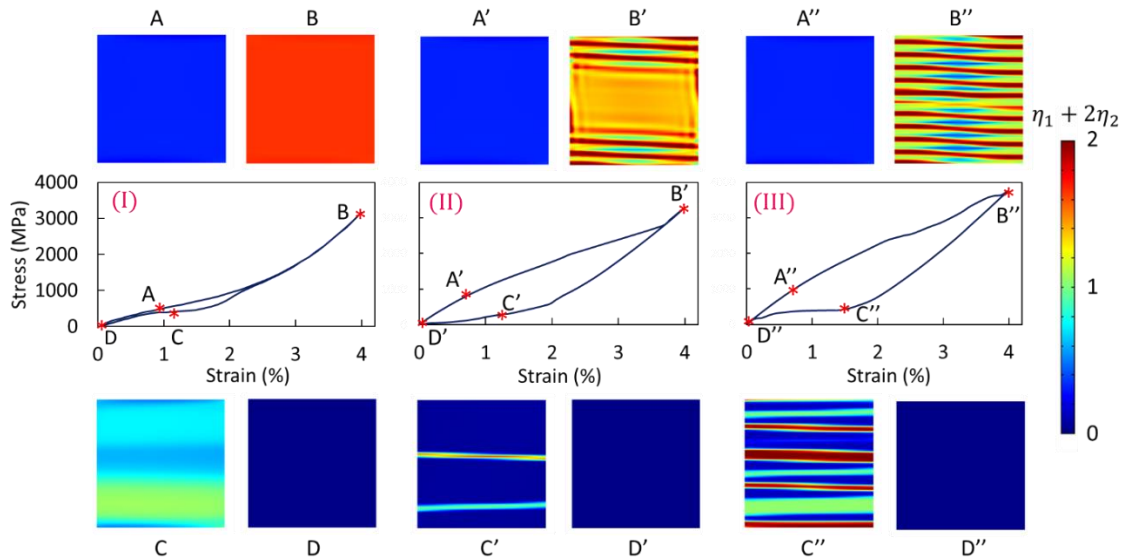


Figure 3.3 Predicted stress-strain curve and microstructure for [001] oriented sample by (I) Convex, (II) Concave, and (III) Double-well  $F_{ch}$ .

According to Figure 3.3, although all three forms of  $F_{ch}$  yield a hysteresis strain-strain curve, none of them predicts a plateau region when the transformation starts, while this is

observed in the experimental stress-strain curves for shape memory materials. Also, it is worth noting that the stress at each strain and the ultimate stress (the stress at the highest strain), is different in these three cases. This can be explained based on the fact that the first derivative of  $F_{\text{ch}}$  with respect to OPs determines the evolution rate of the OPs (Eq.(3.16)), and this determines the rate of the transformation strain tensor (Eq.(3.4)). On the other hand, the transformation strain rate directly affects the rate of subtraction of the stress-free strain tensor from the total strain tensor, and this consequently changes the elastic strain tensor rate (Eq.(3.3)). Also, since the stress tensor is calculated based on the elastic strain tensor (Eq.(3.14)), each  $F_{\text{ch}}$  leads to a different stress at each strain.

The elastic modulus in the beginning of the stress-strain curve should be close to 247 GPa which is the inverse of the second diagonal component of the compliance tensor of tetragonal phase (the  $c_t$  axis of the crystal is along the z-direction). Since we use the double-well  $F_{\text{ch}}$ , the elastic modulus based on Figure 3.3(III) is calculated to be 160 GPa, which is about 35% lower than 247 GPa . This means the elastic modulus is highly affected by MPT. The same issue appears in most of previous works, regardless of the choice of the chemical free energy or OP-strain relation [19, 108, 121, 134, 135]. To address this issue, we propose a modification to the  $F_{\text{ch}}$  in the following section.

### 3.7.2 Modification of the chemical free energy ( $F_{\text{ch}}$ )

In Figure 3.3, all three forms of  $F_{\text{ch}}$  yield a hysteresis stress-strain curve, but in all three stress-strain curves a plateau region (or a region with low or even negative hardening) is missing, and most importantly the elastic modulus is underestimated in the beginning of the stress-strain curve. This problem is rooted in the Eq.(3.16). This equation which expresses the evolution (the rate) of each OP, is dependent on the first derivative of the  $F_{\text{ch}}$  with respect to each OP

(Eq.(3.18)). On the other hand, the rate of OPs affects the rate of the elastic strain tensor (Eq.(3.3)), and the rate of the elastic strain tensor affects the stress (Eq.(3.26)). Therefore, by controlling the first derivate of  $F_{\text{ch}}$  with respect to OPs, the rate of OPs and subsequently the shape of the mechanical response can be controlled. Based on the above explanation, we propose the following modification to the  $F_{\text{ch}}$ :

$$F_{\text{ch}}(\eta_1, \eta_2, \dots, \eta_m) = \int_V \Delta G \left( a \sum_{p=1}^m \eta_p^2 - b \sum_{p=1}^m \eta_p^3 + c \left( \sum_{p=1}^m \eta_p^2 \right)^2 + d \sum_{p=1}^m |\eta_p|^n \right) dV; \quad (3.36)$$

$$1 < n < 2,$$

where  $d$  and  $n$  are new coefficients to be determined in addition to  $a$ ,  $b$ , and  $c$ . Parameter  $n$  takes a value between 1 to 2, and in this paper, we consider it to be equal to 1.1. This parameter should be small enough (close to 1) to keep the elastic modulus unaffected by the OP at the beginning of loading by approximating a linear term in  $F_{\text{ch}}$  (Eq.(3.36)). To elaborate more, the added term ( $d \sum_{p=1}^m |\eta_p|^n$ ), at the beginning of the loading (when the OPs are small) adds a considerable amount of positive energy to the system (see Eq.(3.16), Eq.(3.36), and Eq.(3.37)) which slows down the evolution rate of OPs. Therefore, at the beginning of loading, the material behaves elastically. It should be noted that we use absolute value of  $\eta_p$  to ensure that the modified double-well  $F_{\text{ch}}$  and its first derivative (shown in Figure 3.4b) are well defined around  $\eta_p = 0$ . Considering this modification, the Eq.(3.18) will change to:

$$\frac{\delta F_{\text{ch}}}{\delta \eta_p} = \Delta G ( 2a\eta_p - 3b\eta_p^2 + 4c\eta_p \sum_{p=1}^m \eta_p^2 + nd|\eta_p|^{n-1} \text{sign}(\eta_p) ). \quad (3.37)$$

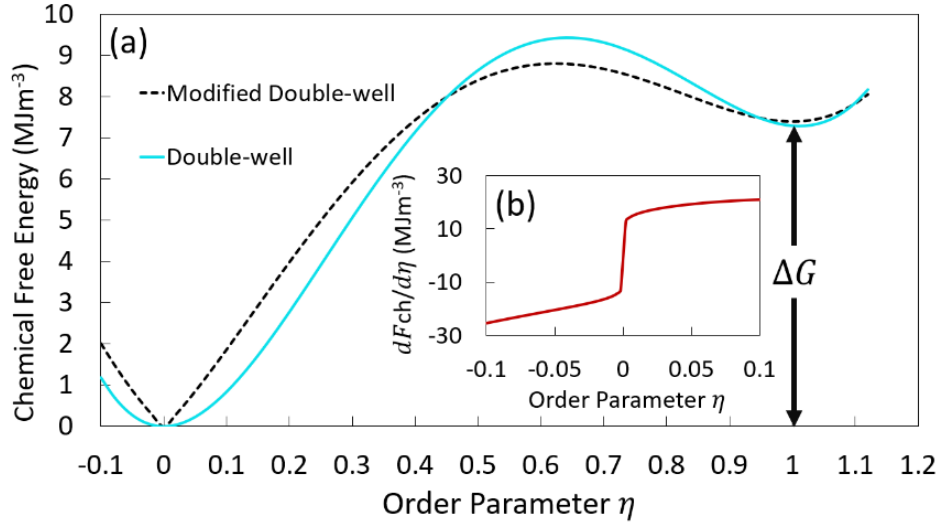


Figure 3.4 **a)** The modified double-well versus double-well form of  $F_{ch}$ , and **b)** The first derivative of the modified double-well form of  $F_{ch}$  with respect to  $\eta$  around  $\eta = 0$ .

Since the proposed modification is for controlling the rate of OPs by adding an extra term of  $d \sum_{p=1}^m |\eta_p|^n$ , it can be easily applied to 2-4-6 form of  $F_{ch}$  as well.

To examine the modified  $F_{ch}$  in terms of microstructure and mechanical response prediction, by choosing  $n = 1.1$  and considering the same  $\Delta G$ , we determine  $a$ ,  $b$ ,  $c$ , and  $d$  such that modified  $F_{ch}$  produces a double-well function close to the double-well  $F_{ch}$  seen in Figure 3.2. The values of these parameters are presented in Table .3. Also, the same domain and boundary conditions shown in Figure 3.1 are considered. Figure 3.4a shows the modified and unmodified double-well  $F_{ch}$ . In both cases,  $F_{ch}$  has two minima, one at  $\eta_p = 0$  and one at  $\eta_p = 1$ .

Table 3.3 Coefficients of the modified chemical free energy (Eq. (3.36)).

$a$	2.64
$b$	10.04
$c$	5.37
$d$	3.05
$n$	0.1

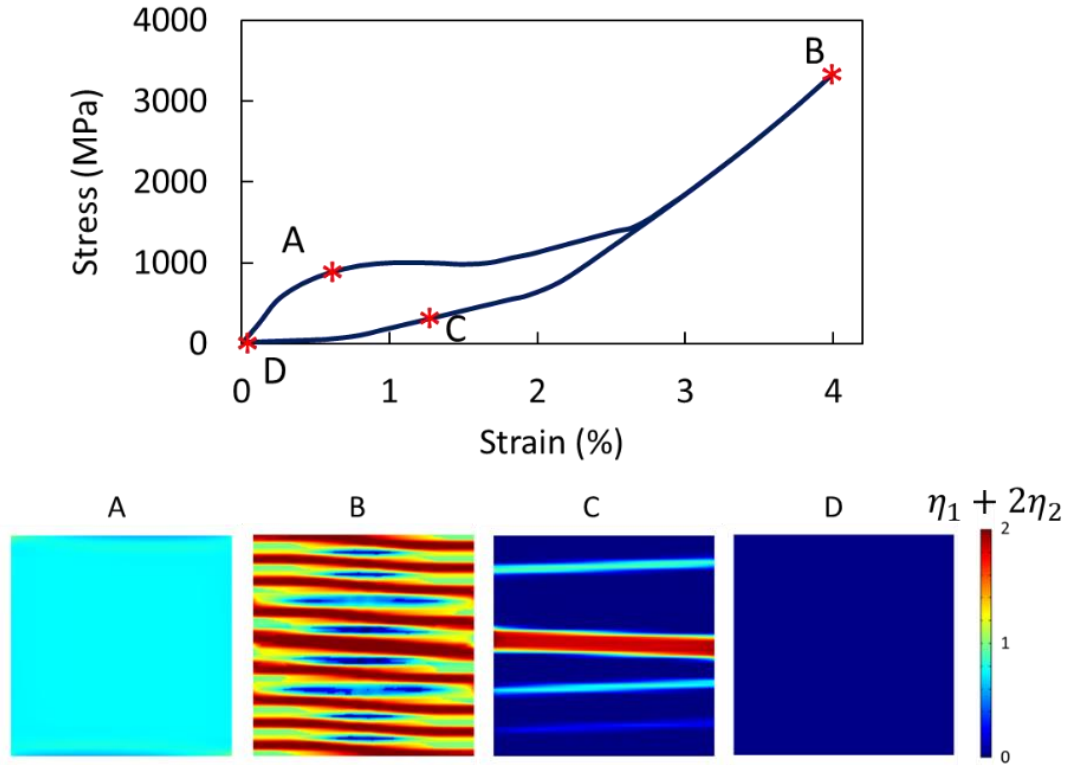


Figure 3.5 Predicted stress-strain curve and microstructure for [001] oriented smaple by modified  $F_{ch}$ .

In Figure 3.5, the modified  $F_{ch}$  predicts a plateau region in the stress-strain curve which is more realistic compared to the unmodified double-well. Additionally, it predicts the experimentally observed twin-martensite microstructures for zirconia-based ceramics [13].

Furthermore, the elastic modulus in the beginning of the stress-strain curve based on Figure 3.5, is about 235 GPa, which is 5% less than the 247 GPa. This shows that the modified PF model has a low effect on the elastic modulus in the beginning of the stress-strain curve and yields a realistic stress-strain curve. In addition, this low error shows that  $n = 1.1$  is an acceptable choice. In the following section we use the modified PF model to study the interaction of fracture and MPT.

### 3.7.3 Interaction of MPT and fracture

The modified  $F_{ch}$  is used to study the interaction between MPT and fracture in a pre-cracked 3Y-STZ single crystal. Three different crystal orientations of  $\theta = 0^\circ$  ([001]),  $+15^\circ$  ( $[\bar{1}04]$ ), and  $90^\circ$  ([100]) are considered. The domain of Figure 3.1 is considered with an initial center crack of  $0.2\mu\text{m}$  (10% of the domain width) which is modeled with a Dirichlet boundary condition of  $\phi = 1$  imposed on the initial crack length. A monotonically increasing displacement rate of  $\dot{u}^* = 2 \times 10^{-3} \frac{\mu\text{m}}{\text{s}}$  is imposed on the top surface. Linear quadrilateral elements with a maximum size of  $0.008\mu\text{m}$ , which is equal to  $0.4k$ , is used in the sample. This element size is chosen based on the element size suggested by Miehe et al. [66]. In their work they suggested that the maximum size of the quadrilateral elements must be less than 50 percent of the  $k$  to ensure accuracy and convergence. Additionally, to reduce the computational demand of the model, only the elements within  $\pm 0.2 \mu\text{m}$  of the horizontal centerline are given degree of freedom for the crack phase field.

Figure 3.6 shows the obtained stress-strain curve, MPT, crack path, and stress map (S33 is shown which is the z component of stress tensor and is in the direction of applied displacement) for four different points on the stress-strain curve. As it is expected, since the stress concentration is high around the crack tips, the transformation starts from the crack tips and then spreads to the other regions of the sample, similar to experimental observations [12]. Also, according to Figure 3.6, as the crack propagates, the reverse MPT (from monoclinic to tetragonal) occurs behind the crack tips (in the wake of the crack tips). This reverse MPT is in a good agreement with the experimental observation for crack propagation in the SE shape memory materials [136]. This reverse MPT occurs because in the SE regime, the reverse MPT occurs in the regions which experience unloading. This unloading is due to diminished load

bearing capability resulting from separation of crack faces in the wake of the crack tips. This unloading process is clearly shown in the stress map in the fourth row of Figure 3.6. The white triangles in the stress map indicate the regions behind the crack tips that unloading occurs at point *C* in Figure 3.6.

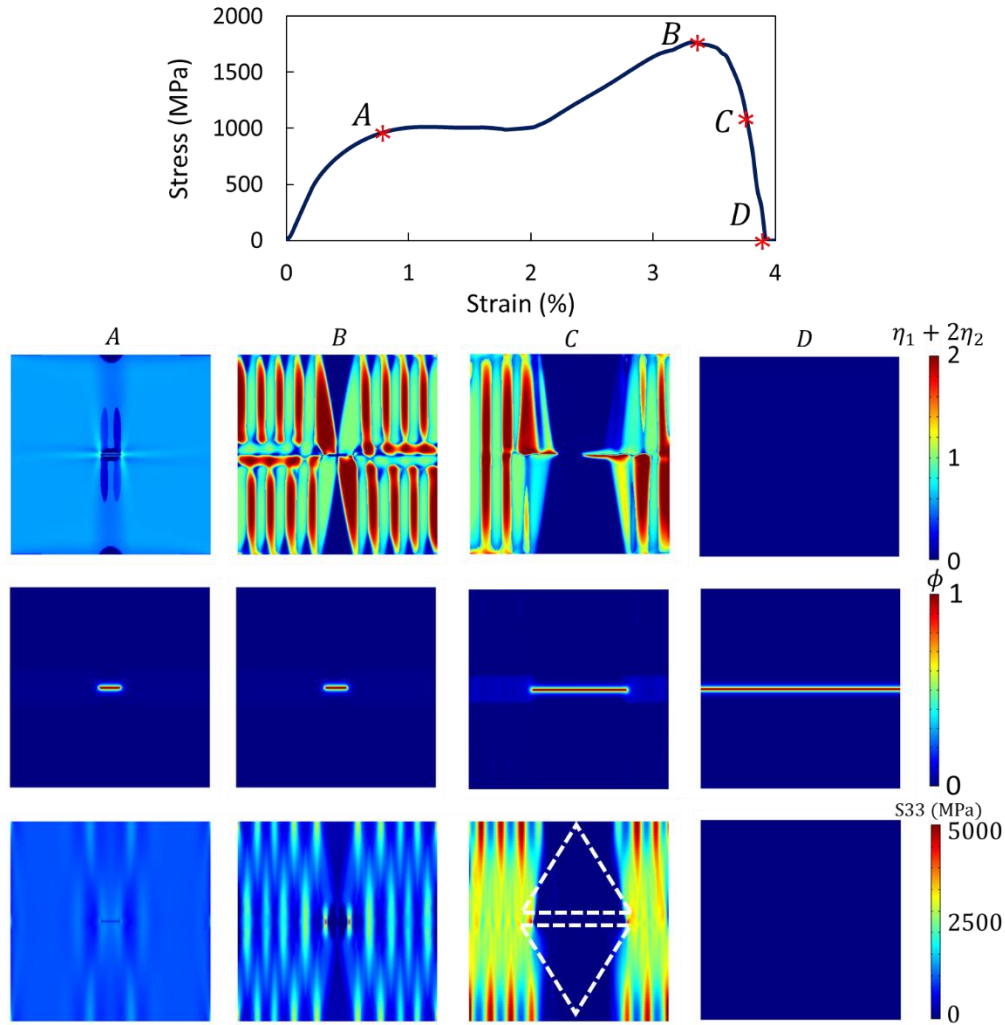


Figure 3.6 Stress-strain curve, MPT, crack path, and stress map for [001] oriented sample under uniaxial tension in the z direction.

In Figure 3.6, before the start of the plateau region in the stress-strain curve (before point *A*), the sample is mostly in tetragonal phase. After this point, the phase transformation starts from the crack tips and then propagates to the rest of the sample. Based on Figure 3.6, the

ultimate strain is 4%. In the experimental study by Lai et al. [5], a maximum bending strain of 8% was reported for a coarse-grained micropillar specimen. Therefore, a model prediction of the maximum strain for a cracked single crystal experiencing uniaxial tension is expected to be less than the reported maximum bending strain. Furthermore, our model predicts the stress drop observed in the displacement-controlled loading experiments due to the crack propagation (between point *B* and *D*) which was not captured in [22, 23] due to using the stress-controlled loading conditions.

Figure 3.7 depicts both the average volume fraction of the monoclinic variants and half crack length versus applied displacement. This figure shows that MPT starts as soon as the load is applied, and the crack starts to propagate after the applied displacement reaches to  $0.008 \mu\text{m}$  (point a). In addition, after the crack length reaches to about  $0.45 \mu\text{m}$  (point c), the average volume fraction of the monoclinic variants starts to decrease and will become zero after the crack is fully developed. The average volume fraction of the monoclinic variants decreases due to the reverse MPT happening beyond the crack tips.

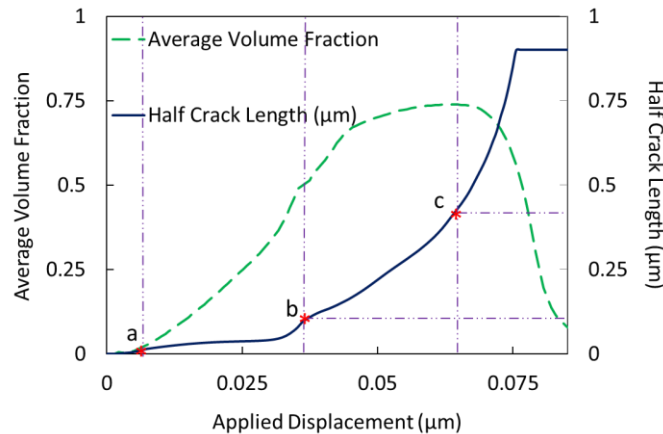


Figure 3.7 The average volume fraction of the monoclinic variants vs. half crack length versus applied displacement for [001] oriented sample.

In Figure 3.7, the crack advances at a low rate until its half-length grows to about 0.12  $\mu\text{m}$  (point B). The crack then grows at a very high rate until it propagates through the whole domain. This behavior is indicative of the rising R-curve behavior due to transformation toughening in yttria-stabilized zirconia ceramics [9, 10, 137] which is captured by our phase-field simulations.

In order to test the validity of microstructure prediction and crack path by the proposed phase-field model, we repeated the uniaxial tension simulation for  $[\bar{1}04]$  oriented sample. Figure 3.8 shows the obtained microstructure, crack path, and stress map (S33 component). The deformed shape of the domain is also provided in the fourth row. Figure 3.8b depicts the experimental microstructure and crack path for a zirconia based ceramic [11] with a similar crystal orientation with respect to crack direction. In this experiment, the material was in SE regime, and the reverse PT behind the crack tip and crack deflection due to PT were observed when crack propagated. As it can be seen in Figure 3.8 our model accurately captures the reverse PT and crack deflection due to MPT similar to the experimental results. By comparing Figure 3.6 and Figure 3.8a, it is evident that the crystal orientation affects the mechanical response, direction (distribution pattern) of transformed regions, and crack path. The rotation of the stiffness tensor and the stress-free strain tensor led to a different transformation stress (point A) and different fracture stress ( $\sigma_F$ ) (point B) for different crystal orientations. The predicted transformation and fracture stresses are 1000 MPa and 1800 MPa for [001] and 600 MPa and 1400 MPa for  $[\bar{1}04]$  oriented sample. According to the zirconia-based coarse-grained micropillar bending test [5], a transformation stress of about 1200 MPa and a fracture stress of about 2200 MPa were reported; therefore, we can conclude that our proposed modified model is

able to quantitatively predict the mechanical behavior of SE zirconia and effectively captures the effect of grain orientation on predicting the mechanical response and microstructure.

Finally, the case of  $\theta = 90^\circ$  ([100]) was considered. The results are not presented here as neither phase transformation nor crack deflection occurred in this case. For this crystal orientation under the applied displacement boundary condition, a very small elongation occurs in the [001] direction, MPT is not considerable, and only a straight fracture path is observed. The mechanical response and crack path are an indication of a purely brittle material behavior. This predictions are consistent with the previously reported results by PFM [16] and MD [30] simulations, showing the importance of crystal orientation on the overall behavior of SMCs.

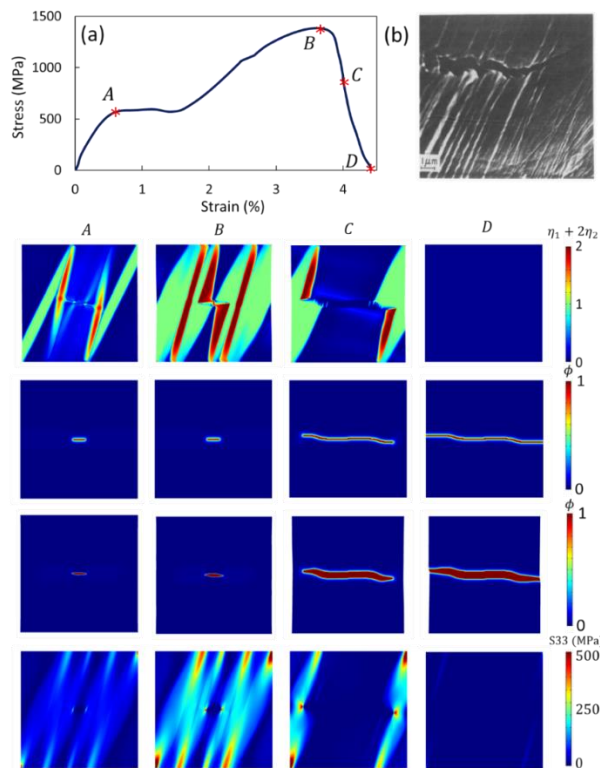


Figure 3.8 **a)** Stress-strain curve, MPT, crack path (deformed and undeformed), and stress map for  $[\bar{1}04]$  oriented sample under uniaxial tension in z direction, and **b)** Experimentally observed MPT and crack deflection due to PT in a zirconia-based ceramic [11].

### 3.8 Conclusion

We presented a modified phase-field model for studying interactions of MPT and cracking in a super-elastic 3 mol% yttria-stabilized tetragonal zirconia crystal. We identified the following shortcomings in previous PF studies coupling MPT and cracking:

The interaction between SE behavior due to MPT and crack propagation at the microscale were not studied previously. Therefore, the important features of reverse MPT due to crack propagation were not simulated before.

In many MPT models the elastic modulus is not recovered in the initial stages of the loading, and this is due to the high evolution rate of the order parameter(s) at the beginning of loading.

In previously reported stress-strain curves, stress drop due to crack propagation was not captured, therefore, a conclusion about the strength of the material could not be made. This shortcoming is typically due to the use of stress-controlled boundary conditions, which were used in most previous models.

In this paper, we addressed these shortcomings, by modifying the chemical free energy and enabling displacement-controlled boundary conditions. The modification included adding an extra term to the 2-3-4 chemical free energy to accurately predict the mechanical response and reversible tetragonal to monoclinic transformation. This added term gives more control on the phase transformation rate (evolution of order parameters) and solves the problem of underestimating the elastic modulus observed in other phase-field models. The obtained results for transformation assisted deformation showed that the modified model is capable of predicting a realistic mechanical response, the experimentally observed microstructure, and the forward and reverse phase transformation in shape memory ceramics.

In addition, we applied the modified phase-field to study transformation-fracture interactions under displacement-controlled loading condition. We also studied the effect of different crystal orientation with respect to loading direction. The model can predict a realistic mechanical response and fracture strain, the experimentally observed microstructure and crack path due to phase transformation, the effect of grain orientation on both microstructure and mechanical response, and the reverse phase transformation due to crack propagation in super-elastic shape memory ceramics. In addition, since we applied a displacement-controlled boundary condition, we were able to observe a final drop in the stress-strain curve due to crack propagation and establish a strength close to experimentally reported one for zirconia-based ceramics. Comparisons with experiments showed that the proposed modified model effectively captures accurate microstructures and crack deflection due to phase transformation and provides an admissible stress-strain curve. Such predictions are difficult to obtain from experiments which show the advantage of phase-field modeling in studying interactions of phase transformation and cracking.

CHAPTER 4  
LOCALIZED PLASTIC STRAIN ACCUMULATION IN SHAPE MEMORY CERAMICS  
UNDER CYCLIC LOADING

Reproduced from A. Lotfolahpour and M. Asle Zaeem, “*Localized plastic strain accumulation in shape memory ceramics under cyclic loading*”, International Journal of Mechanical Sciences 272 (2024): 109295.

#### **4.1 Abstract**

The premature failure of shape memory ceramics (SMCs) under cyclic loading is a critical issue limiting their applications as actuators and thermal protection layers. Martensitic phase transformation (MPT), essential for superelasticity and shape memory functionalities in SMCs, induces localized plastic deformations due to phase expansion. In polycrystalline materials, the accumulation of localized plastic strain serves as the primary mechanism for fatigue crack initiation under cyclic loading. In this research, a phase-field phase transformation model coupled with a viscoplasticity model is presented to study the effects of microstructural features, engineered pores, and sample size on plastic strain accumulation (PSA) during cyclic loading of SMCs. Our findings highlight that the GBs are critical regions with high PSA, with noticeable reductions observed by decreasing the grain boundary density. Additionally, we found that engineered pores effectively reduced cyclic PSA, however, we identified a threshold on the volume fraction of pores. Also, textured microstructures with certain characteristics demonstrate significant influence on cyclic PSA. A cross-correlation data analysis approach is employed to study the relationship between the studied microstructural features and PSA to facilitate the identification of the most important factors controlling the irreversible PSA during compressive cyclic loading. By mitigating the rate of PSA, significant enhancements in cyclic life before fatigue crack initiation can be achieved, enabling superior performance in practical applications.

## 4.2 Introduction

Zirconia based shape memory ceramics (SMC)s are a class of smart materials that can be used as actuators, sensors, thermal protection layers, and energy dampers in a variety of industries such as aerospace and biomedical [1-4]. The underlying mechanism of superelasticity (SE) and shape memory effect (SME) behaviors in these materials is governed by MPT between two different crystallographic phases of tetragonal (*T*) and monoclinic (*M*). The shape change during MPT is associated with a large shearing and normal strains which cause large mismatch stresses mainly at phase interfaces and grain boundaries (GBs) [5]. The material must be able to accommodate these strains, otherwise after a few loading cycles, in the regions with large mismatch stresses, microscopic fatigue cracks initiate and propagate which then lead to a macroscopic failure.

In the macroscopic scale, these ceramics fracture at strains as low as 2% which is lower than the full transformation strain about 7% [5]. However, in microscopic samples, under certain microstructure configurations, multiple SE or SME cycles with full forward and reverse transformation can be observed [5, 6]. For example, Lai et al. [5] made micropillars of ceria or yttria-stabilized zirconia ceramics with low number of grains and GBs through reducing the diameter of the micropillars, and in some of the samples they observed up to 55 complete SE cycles before fracture occurred. The underlying mechanism of crack initiation in these polycrystalline ceramics were reported to be the localized PSA mainly at GBs and phase interfaces [8, 138, 139]. SMCs are brittle and unable to fully accommodate the shape change due to MPT, and this can cause high mismatch stresses at GBs, phase interfaces, and around precipitates. The mismatch stresses cause local plastic strains originated from irreversible mechanisms such as GB sliding and dislocation activity [139]. In addition, both experimental [8]

and numerical studies [18, 30, 31] well establish that the occurrence of MPT and plasticity is highly dependent on the crystallographic orientations of grains with respect to the loading direction [8, 18, 30, 31]. Under cyclic loading, in the regions where plastic deformation originates, the PSA increases with each loading cycle and when it reaches a critical value, fatigue crack initiates [140-143]. Therefore, the PSA rate directly affects the fatigue life of materials and can be used as a fatigue indicator parameter to evaluate the number of loading cycles before fatigue crack initiation [32, 143, 144].

Computational studies can be used to further investigate the effects of the microstructural features such as grain orientation, grain boundary density (GBD), and grain size (GS), as well as engineered pores on the plastic strain localization and accumulation in polycrystalline SE zirconia-based SMCs. Computational studies enable investigation of the effects of each microstructural feature separately and collectively which is difficult, if not impossible, by experimental studies. Among the previous models for studying microstructure evolution in materials, the phase-field (PF) approach has emerged a powerful computational method that has been successfully applied to study MPT [31] and microstructure evolution in single crystal and polycrystalline shape memory alloys [34, 54, 145, 146] and SMCs [14-16, 53, 147]. In this approach the PF order parameters (OPs) represent the parent and product phases, and the shape change between parent and product phases is implemented through a stress-free strain tensor.

The PF approach or constitutive models coupled with plasticity models have been previously used to study the interaction between MPT and plastic deformations in shape memory materials, with a particular focus on NiTi alloys [38-41, 148-153]. Among these studies, Yu et al. [150], proposed a crystal plasticity-based model to simulate MPT and plastic deformation in NiTi single crystals. Similar to experimental observations, their model predicted a high residual

plastic strain during initial cycles and their model captured the effects of crystal orientation. Paranjape et al. [40] coupled a PF-MPT model with a crystal plasticity model to investigate the evolution of plastic deformation under cyclic thermal loadings. They studied the effects of plastic strain on MPT and transformation temperature. In a different study, Paranjape et al. [152] coupled PF-MPT with a rate-dependent crystal plasticity to simulate the interaction between slip plasticity and MPT in NiTi single crystal micropillars. They found a correlation between orientation of phase interface and dominating slip systems. Xie et al. [39], developed a crystal plasticity-based PF model and studied the cyclic behavior of a single crystal sample. They showed that plastic strain highly affects the stress-strain curve, and the accumulation occurs mainly along the phase interfaces. Xu et al. [41] coupled a PF-MPT model with a crystal plasticity model to study cyclic response of NiTi single crystals under thermal loads. They investigated the effects of plastic strain on forward and reverse MPT as well as martensite reorientation. Later on, Ju et al. [153] developed a comprehensive model that incorporates MPT and different types of plasticity, including slip. They predicted cyclic degradation in NiTi single crystal samples, and the obtained hysteresis loop and PSA was in good agreement with experiment.

The above studies on coupling MPT and plasticity in shape memory materials were focused on single crystal samples, limiting their ability to capture the effects of microstructural features such as GBs and grain size on the interaction between MPT and PSA. It is important to note that there have been some attempts to model the interaction between MPT and plasticity in polycrystalline samples [34-37, 154-157]. For example, Xie et al. [34] utilized a crystal plasticity-based PF model and studied the cyclic behavior of polycrystalline NiTi samples under different loading rates. Additionally, Cisse and Asle Zaeem [35] studied the mechanical response

and PSA in Cu-based SMAs under thermal loading. They predicted the stress-strain stabilization as well as cyclic plastic accumulation at GB triple junctions. In addition, they showed that plastic strain prevents complete shape recovery of the SMA in both SME and SE regimes. Xu et al. [36] proposed a crystal plasticity PF based model to study the cyclic degradation in polycrystalline NiTi samples. They observed an increasing irrecoverable cyclic plastic strain and examined the impact of plastic strain on the mechanical response of samples. Additionally, they studied the effects of strain rates and applied constant stress on the cyclic PSA. Chaugule and B.Le Graverend [37] developed a crystal plasticity-based model that incorporated mechanisms of MPT, transformation induced plasticity (TRIP), and viscoplasticity. They investigated the coupling between these mechanisms in single and polycrystal samples of a high temperature shape memory alloy (HTSMA). They successfully observed the progressive accumulation of viscoplastic strain versus number of thermal loading cycles similar to experimental observation. Kan et al. [157] developed a micromechanical model which included a viscoplasticity model to simulate cyclic response of HTSMAs. They applied cyclic thermal loadings and identified viscoplasticity as a primary irreversible mechanism in HTSMAs. Furthermore, their analysis revealed that viscoplasticity has a larger impact on the cyclic response under lower loading rates.

None of the studies investigating the interplay between MPT and plasticity in polycrystalline shape memory materials offer insights into the correlation between microstructural features, PSA, and fatigue crack initiation. Furthermore, these studies did not explore the influence of microstructural features on reducing PSA to enhance cyclic life prior to fatigue crack initiation. A recent study investigated the fatigue crack initiation and propagation in shape memory materials [143] by developing a TRIP-based fatigue model which incorporated TRIP accumulation as a fatigue indicator parameter for predicting low-cycle fatigue crack

initiation in polycrystalline NiTi samples. They validated their model against experimental data. However, their study did not examine the effects of microstructural features on TRIP, and also it did not offer any strategies to reduce TRIP accumulation.

There have been studies on fatigue crack propagation modeling in macroscopic domains [97, 158-162]. However, the majority of these studies lacked the inclusion of PSA which is a crucial phenomenon leading to fatigue crack initiation. Even when plasticity is considered, similar to microscale studies, none of previous studies provided insights into the fatigue crack initiation process or offered approaches to increase cyclic life before fatigue crack initiation by mitigating PSA.

In summary, previous works on coupling MPT with plasticity have not investigated the effects of microstructural features on the interaction between MPT and PSA in shape memory alloys and ceramics. Furthermore, none of these studies provided strategies to mitigate PSA to enhance cyclic life before fatigue crack initiation. In this research we aim to address these gaps by presenting a PF-based framework coupling PF-MPT with a viscoplasticity model to investigate the effects of the microstructural features on the plastic strain localization and accumulation in polycrystalline SMCs. To derive the viscoplasticity governing equations, we start from the total energy of the system and treat the plastic multiplier as an OP and minimize the total energy with respect to this OP. Then we demonstrate that with this approach we can recover the Bingham [163] viscoplasticity model. This approach yields a simple viscoplasticity model and we show that it predicts acceptable cyclic PSA that agrees with experimental results. The ideas and simulations presented in this work for reducing PSA have not been investigated in previous experimental or computational studies. The primary objective of this study is to provide guidance on mitigating PSA in order to enhance the cyclic life of SMCs.

### 4.3 Phase-Field Model

This section first details the coupling between PF modeling of MPT and viscoplasticity. We start the formulation from the total energy of the system ( $F_{\text{tot}}$ ) that includes all potential source and sink energies and proceed to elaborate on each energy term in detail. Subsequently, we express the governing equations and derive the OPs evolution equations using the Ginzburg-Landau relation and energy minimization principles. In subsection 4.3.2, we explain the PF approach to generate polycrystals and discuss the advantages of this approach compared to other approaches to create polycrystalline microstructures.

#### 4.3.1 Coupling the PF of MPT and Viscoplasticity

In PF model of MPT,  $\eta_i$  are used as the order parameters representing different phases in the system.  $\eta_i = 0$  represents the tetragonal phase and  $\eta_i = 1$  represents each of the two monoclinic variants in the c-a plane of zirconia. The  $F_{\text{tot}}$  can be written as:

$$F_{\text{tot}}(u_i, \eta_1, \eta_2, \dots, \eta_m) = F_{\text{el}} + F_{\text{ch}} + F_{\text{gd}} + F_{\text{pl}}, \quad (4.1)$$

where  $F_{\text{el}}$  is the elastic strain energy,  $F_{\text{ch}}$  is the chemical free energy,  $F_{\text{gd}}$  is the gradient energy of the tetragonal-monoclinic or monoclinic-monoclinic interfaces, and  $F_{\text{pl}}$  is the energy dissipation due to plastic deformation. These energies are explained in detail in the following.

- *Elastic strain energy* ( $F_{\text{el}}$ ):  
 $F_{\text{el}}$  can be written as:

$$F_{\text{el}}(u_i) = \int_V \frac{1}{2} C_{ijkl} \varepsilon_{kl}^{\text{el}} \varepsilon_{ij}^{\text{el}} dV, \quad (4.2)$$

where  $u_i$  is the displacement,  $C_{ijkl}$  is the elastic tensor, and  $\varepsilon_{ij}^{\text{el}}$  is the elastic strain which is defined as the difference between the total strain ( $\varepsilon_{ij}^{\text{tot}}$ ), transformation strain ( $\varepsilon_{ij}^{\text{tr}}$ ), and plastic strain ( $\varepsilon_{ij}^{\text{pl}}$ ):

$$\varepsilon_{ij}^{\text{el}} = \varepsilon_{ij}^{\text{tot}} - \varepsilon_{ij}^{\text{tr}} - \varepsilon_{ij}^{\text{pl}}. \quad (4.3)$$

Considering a linear relation between the OPs and strains [53, 107, 109, 121],  $\varepsilon_{ij}^{\text{tr}}$  is defined as:

$$\varepsilon_{ij}^{\text{tr}} = \sum_{p=1}^m \varepsilon_{ij}^{00}(p) \eta_p, \quad (4.4)$$

where  $\varepsilon_{ij}^{00}$  is the stress-free strain tensor which represents the change in microstructure between parent and product phases [16]. The small strain assumption is considered and is defined as:

$$\varepsilon_{ij}^{\text{tot}} = \frac{1}{2} (u_{i,j} + u_{j,i}). \quad (4.5)$$

The difference between elastic constants in tetragonal and monoclinic phases is represented by the following linear relation [16]:

$$C_{ijkl}(\eta_1, \eta_2, \dots, \eta_m) = C_{ijkl}^T + \sum_{p=1}^m \eta_p (C_{ijkl}^M - C_{ijkl}^T), \quad (4.6)$$

where  $C_{ijkl}^T$  and  $C_{ijkl}^M$  are elastic constants of the tetragonal and monoclinic phases, respectively.  $m$  is the number of product phases (monoclinic variants in this study). The elastic energy defined in Eq. (4.2) is based on the Hooke's law, therefore the stress tensor is related to elastic strain tensor through the following equation:

$$\sigma_{ij}(u_i, \eta_p) = C_{ijkl}(\eta_1, \eta_2, \dots, \eta_m) \varepsilon_{kl}^{\text{el}}. \quad (4.7)$$

- *Chemical free energy ( $F_{\text{ch}}$ ):*

$F_{\text{ch}}$  determines the system's energy dissipation due to MPT. The 2-3-4 or 2-4-6 Landau polynomials defined in terms of order parameters are the most common types of  $F_{\text{ch}}$  [31].

However, these chemical energies underestimate the elastic response in the beginning of the stress-strain curve. Lotfolahpour et al. [53] proposed a modification to the 2-3-4 polynomial to address the elastic modulus underestimation, which is used in this paper:

$$F_{\text{ch}}(\eta_1, \eta_2, \dots, \eta_m) = \int_V \Delta G \left( a \sum_{p=1}^m \eta_p^2 - b \sum_{p=1}^m \eta_p^3 + c \left( \sum_{p=1}^m \eta_p^2 \right)^2 + d \sum_{p=1}^m |\eta_p|^n \right) dV; \quad (4.8)$$

$$1 < n < 2,$$

where  $\Delta G$  is the chemical driving force and is the difference in the specific  $F_{\text{ch}}$  between the parent and the product. The following equation can be used to calculate  $\Delta G$  for 3Y-STZ at different temperatures [16, 123]:

$$\Delta G(T \rightarrow M) = -6159.18 + 6.98T, \quad (4.9)$$

where the energy is in  $\text{Jmol}^{-1}$  (or  $\text{Jm}^{-3}$ ) and the temperature (T) is in Kelvin (K). In addition,  $a$ ,  $b$ ,  $c$ ,  $d$ , and  $n$  are coefficients that should be chosen in a way that maintains the value of the interfacial energy within the physical reasonable range [53] and at  $\eta_p = 1$  result in  $F_{\text{ch}} = \Delta G(T \rightarrow M)$ .

- *Gradient free energy ( $F_{\text{gd}}$ ):*

$F_{\text{gd}}$  represents the interfacial energy between tetragonal-monoclinic or monoclinic-monoclinic phases and ensures a smooth transition of the OPs between different phases. It is expressed as:

$$F_{\text{gd}}(\eta_1, \eta_2, \dots, \eta_m) = \int_V \frac{B_{ij}}{2} \sum_{p=1}^m \nabla_i \eta_p \nabla_j \eta_p dV, \quad (4.10)$$

where  $\nabla$  is the gradient operator and  $B_{ij}$  is gradient energy tensor. We assume that the gradient energy coefficient is isotropic ( $B_{ij} = B\delta_{ij}$ ) [16]. Therefore the Eq. (4.10) becomes:

$$F_{gd}(\eta_1, \eta_2, \dots, \eta_m) = \int_V \frac{B}{2} \sum_{p=1}^m (\nabla \eta_p)^2 dV. \quad (4.11)$$

- *Plastic energy ( $F_{pl}$ ):*

$F_{pl}$  represents the system's energy dissipation due to plastic deformation, and it can be expressed as [164]:

$$F_{pl} = \int_V \int_0^{\varepsilon_{eq}^{pl}} \sigma_y(\varepsilon_{eq}^{pl}) d\varepsilon_{eq}^{pl} dV \quad (4.12)$$

where  $\sigma_y$  is the yield stress which is dependent on the equivalent plastic strain ( $\varepsilon_{eq}^{pl}$ ) and is defined as:

$$\sigma_y = \sigma_{y0} + H\varepsilon_{eq}^{pl}. \quad (4.13)$$

$\sigma_{y0}$  is the initial yield stress.  $H$  is the hardening coefficients.

- *Governing equations*

The evolution of the OPs representing the MPT can be obtained through Ginzburg-Landau relation [124, 125]:

$$\frac{\partial \eta_p}{\partial t} = L \left( \frac{\delta F_{tot}}{\delta \eta_p} \right) = L \left( \frac{\delta F_{el}}{\delta \eta_p} + \frac{\delta F_{ch}}{\delta \eta_p} + \frac{\delta F_{gd}}{\delta \eta_p} + \frac{\delta F_{pl}}{\delta \eta_p} \right), \quad (4.14)$$

where  $L$  is the mobility parameter and controls the evolution rate of the OP  $\eta_p$ . The expansion of the above equation is:

$$\begin{aligned} \frac{\delta F_{el}}{\delta \eta_p} = & \frac{1}{2} \varepsilon_{ij}^{el} (C_{ijkl}^M - C_{ijkl}^T) \varepsilon_{kl}^{el} - \frac{1}{2} C_{ijkl}(\eta_1, \eta_2, \dots, \eta_m) \varepsilon_{kl}^{00}(p) \varepsilon_{ij}^{el} \\ & - \frac{1}{2} C_{ijkl}(\eta_1, \eta_2, \dots, \eta_m) \varepsilon_{ij}^{00}(p) \varepsilon_{kl}^{el}, \end{aligned} \quad (4.15)$$

$$\frac{\delta F_{ch}}{\delta \eta_p} = \Delta G(2a\eta_p - 3b\eta_p^2 + 4c\eta_p \sum_{p=1}^m \eta_p^2 + nd|\eta_p|^{n-1} \text{sign}(\eta_p)) \quad (4.16)$$

$$\frac{\delta F_{gd}}{\delta \eta_p} = -B\nabla^2 \eta_p, \quad (4.17)$$

$$\frac{\delta F_{pl}}{\delta \eta_p} = 0. \quad (4.18)$$

It is worth noting that in Eq.(4. 15), the  $\varepsilon_{kl}^{el}$  is dependent on plastic strains (Eq.(4.3)). In other words, this equation shows how plasticity affects the evolution rate of  $\eta_p$ . In this paper to model plasticity, we consider an associative rate-dependent plasticity model. The plastic strain tensor is defined as:

$$\varepsilon_{ij}^{pl} = \int_0^t \varepsilon_{ij}^{\dot{pl}} dt = \lambda N_{ij} ; N_{ij} = \frac{d\sigma_{mises}}{d\sigma_{ij}}, \quad (4.19)$$

where  $\lambda$  is the plastic multiplier and  $N_{ij}$  are the plastic flow directions [165]. The rate of the  $\lambda$  can be found through minimizing the  $F_{tot}$  with respect to  $\lambda$ . It should be noted that this approach is similar to deriving the evolution rate of OPs based on the Ginzburg-Landau relation in PF approach.

$$\frac{\partial \lambda}{\partial t} = \mu \left( \frac{\delta F_{tot}}{\delta \lambda} \right) = \mu \left( \frac{\delta F_{el}}{\delta \lambda} + \frac{\delta F_{ch}}{\delta \lambda} + \frac{\delta F_{gd}}{\delta \lambda} + \frac{\delta F_{pl}}{\delta \lambda} \right), \quad (4.20)$$

where  $\mu$  is the viscosity coefficient which controls the plastic strain evolution rate and plays the same role as  $L$  in Eq.(4.14), and the expansion of the above equation leads to:

$$\frac{\delta F_{el}}{\delta \lambda} = -\frac{1}{2} C_{ijkl}(\eta_1, \eta_2, \dots, \eta_m) N_{kl} \varepsilon_{ij}^{el} - \frac{1}{2} C_{ijkl}(\eta_1, \eta_2, \dots, \eta_m) N_{ij} \varepsilon_{kl}^{el}, \quad (4.21)$$

$$\frac{\delta F_{ch}}{\delta \lambda} = 0, \quad (4.22)$$

$$\frac{\delta F_{gd}}{\delta \lambda} = 0, \quad (4.23)$$

$$\frac{\delta F_{pl}}{\delta \lambda} = \sigma_{yo} + H\lambda|N|. \quad (4.24)$$

The Eq.(4. 21) presents the source terms for plastic strain evolution. In this equation the elastic constants are dependent on the tetragonal and monoclinic variants ( $\eta_p$ ). In addition, the

$\varepsilon_{ij}^{el}$  is dependent on the transformation strain ( $\varepsilon_{ij}^{tr}$ ) and consequently on  $\eta_p$ . These dependencies reveal the coupled relationship between plasticity and MPT and shows that the evolution of the  $\eta_p$  affects the elastic constants and elastic strain and consequently the evolution of plastic strain. In addition, in Eq.(4. 24),  $\lambda$  is  $\varepsilon_{eq}^{pl}$ . In order to make the plastic strain evolve only when stresses exceed the yield stress, we impose the Kuhn-Tucker conditions [166]:

$$\frac{\delta F_{tot}}{\delta \lambda} \leq 0, \quad \frac{\partial \lambda}{\partial t} \geq 0, \quad \left( \frac{\delta F_{tot}}{\delta \lambda} \right) \left( \frac{\partial \lambda}{\partial t} \right) = 0. \quad (4.25)$$

The plastic strain rate can be expressed as:

$$\dot{\varepsilon}_{ij}^{pl} = \frac{\partial \lambda}{\partial t} \mathbf{N}. \quad (4.26)$$

This expression can be inserted in Eq.(4.19) to calculate the  $\varepsilon_{ij}^{pl}$ . It is worth mentioning, this associative rate-dependent plasticity model resembles Bingham viscoplasticity model [163, 165]. Furthermore, the average plastic strain at time  $t$  is calculated through:

$$|\overline{\varepsilon^{pl}}| = \frac{1}{A_{total}} \int_0^t \varepsilon_{eq}^{pl} dA \quad (4.27)$$

where  $A_{total}$  is the total domain area. In addition, by neglecting the body forces, the mechanical equilibrium equations lead to:

$$\text{div } \boldsymbol{\sigma}(u_i, \eta_i) = 0. \quad (4.28)$$

### 4.3.2 Generating polycrystals

This subsection explains our approach to creating polycrystals with different grain sizes. In addition, we explain the advantages of this approach in terms of discretization compared to other methods for creating polycrystals. To generate polycrystals, we use the PF grain growth model [167]. In this approach, a polycrystalline microstructure can be described by many field variables which each variable represents a grain and its orientation, and these variables are

continuous in space. The temporal evolution of these field variables is described by the Ginzburg-Landau relation. This approach can create realistic polycrystals and overcomes the difficulties of generating high quality mesh due to the presence of lines (GBs) and GBs junctions when the grains and GBs are drawn manually or when the topology of the microstructure is directly imported to the numerical model.

We first create polycrystals without considering MPT, plasticity or any other physics. In this approach an OP  $\xi_i$  represents the  $i$ th grain in the domain. The total energy of the system can be expressed as following [167]:

$$F(\xi_i) = G \int_V \left( f + \sum_{i=1}^s \frac{k_i}{2} (\nabla \xi_i)^2 \right) dV, \quad (4.29)$$

$$f = \sum_{i=1}^s \left( -\frac{\alpha}{2} (\xi_i)^2 + \frac{\beta}{4} (\xi_i)^4 \right) + \gamma \sum_{i=1}^s \sum_{j \neq i}^s \xi_i^2 \xi_j^2, \quad (4.30)$$

where  $V$  is the domain volume,  $\alpha$ ,  $\beta$  and  $\gamma$  are the model constants,  $G$  is the energy barrier,  $k_i$  are the gradient energy coefficients which directly determine the width of smeared interface between grains, and  $s$  is the total number of the grain orientations. It worth mentioning that the number of grains in the domain could be higher or lower than  $s$  depending on the initial conditions and the model parameters. The evolution equations of the OPs are obtained based on the Ginzburg-Landau relation [124, 125] and are provided below:

$$\frac{d\xi_i}{dt} = \vartheta G \left( -\alpha \xi_i + \beta \xi_i^3 + 2\gamma \sum_{i=1}^s \sum_{j \neq i}^s \xi_i \xi_j^2 + k_i \nabla^2 \xi_i \right); i \& j = 1, 2, \dots, s; i \neq j, \quad (4.31)$$

where  $\vartheta$  is the mobility parameter and controls the evolution rate of the OPs.

## 4.4 Solution Scheme and Model Parameters

In this section, first the details of the solution scheme are presented. Then, we describe the boundary conditions, the second and fourth order tensors rotation, and the model parameters.

### 4.4.1 Solution scheme and boundary conditions

The governing equations presented in the previous section are solved in a finite element framework using the solid mechanics and mathematics modulus of COMSOL Multiphysics. First, we only solve the PF polycrystal equations to produce the polycrystalline models (grain geometries). In this step, mechanical loads are not applied. We consider the number of OPs  $s$  ( $s$  in Eq.(4.29)) to be 30. In addition, to have a non-zero solution, we apply an initial randomly distributed value between 0 and 0.1 for each OP. After obtaining the polycrystalline structure, we assign an orientation to each grain and use the model for studying MPT under cyclic loading.

The governing equations of MPT, plasticity model, and mechanical equilibrium are solved by applying a cyclic displacement-controlled loading. Furthermore, the plane stress condition is considered in all these 2D simulations. The dimensions of the models and their boundary conditions are shown in Figure 4.1. Based on this figure, rollers are applied on the bottom and left edges to avoid PSA at the boundaries.

For all models, quadrilateral elements are generated by the mapped mesh algorithm feature in COMSOL. A mesh study is conducted, a mesh size of 0.04  $\mu\text{m}$  (or 10,000 quadrilateral elements in the domain) is found to be sufficient to resolve the interface of different OPs. Discretizing the samples with more elements did not noticeably change the microstructure, PT, PSA rate, and mechanical response, therefore we used 10,000 quadrilateral elements. The polycrystalline PF equations and the martensite PF and plasticity equations are solved using the “General Form PDE” module of COMSOL with linear shape functions. The displacements are

solved using the Solid Mechanics module with quadratic shape functions. The staggered scheme [126] is used to solve the governing equations where nonlinear sub-problems are solved with Newton's method. A time step of 0.1s is used for all simulations.

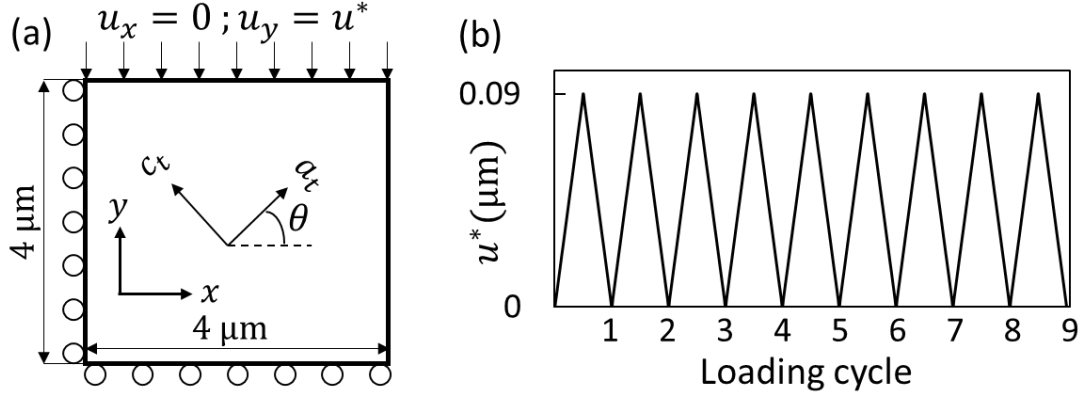


Figure 4.1 a) domain dimensions and boundary conditions, and b) applied displacement versus loading cycle.

It should be noted that in Figure 4.1a)  $\theta$  defines the grain orientation with respect to the global coordinates and measures positive counterclockwise. When  $\theta = 0^\circ$ , the  $a_t$  axis and  $c_t$  axis of the tetragonal phase are aligned with  $x$  axis and  $y$  axis respectively. In addition, in this paper,  $\theta = 0^\circ$  corresponds to  $[010]$  oriented crystal. The following equations will be used to transfer the local stress-free strain tensor ( $\varepsilon_{ij}^{00}(p)$ ) and local elastic stiffness tensor

( $C_{mnop}(\eta_1, \eta_2, \dots, \eta_m)$ ) to the global coordinate system:

$$\varepsilon_{ij}^{G00}(p) = R_{ik}R_{jl}\varepsilon_{ij}^{00}(p), \quad (4.32)$$

$$C_{ijkl}^G = R_{im}R_{jn}R_{ko}R_{lp}C_{mnop}, \quad (4.33)$$

$R_{ij}$  is the rotation matrix for a grain with an orientation angle of  $\theta$ , which in 2D is defined as:

$$R_{ij} = \begin{bmatrix} \cos(\theta) & \sin(\theta) \\ -\sin(\theta) & \cos(\theta) \end{bmatrix}. \quad (4.34)$$

#### 4.4.2 Material properties and model parameters

This subsection details the mechanical properties of the material under investigation, model parameters, and the methodology for calculating the energy difference between the  $T$  and  $M$  phases. It is worth mentioning that the rationale behind selecting the value of  $\mu$  in the viscoplasticity model is discussed in Section 4.4. 3Y-STZ, which is a SMC [138, 168], is the material of study in this work. The equilibrium temperature of 3Y-STZ is reported to be  $\sim 883$  K [16]. We consider the temperature of the system is constant and equal to 905 K and we use this temperature to calculate  $\Delta G$  in Eq.(4. (4.9) which yields  $\Delta G = 156 \text{ Jmol}^{-1}$  ( $7.2 \times 10^6 \text{ Jm}^{-3}$ ). It is worth noting that the considered temperature is higher than the equilibrium temperature, therefore, the system is in SE regime (strain recovery occurs after unloading without a need for temperature change). Eq. (4.35) and (4.36) show the stiffness tensor of tetragonal and monoclinic phases, respectively [130, 169]. In addition, the stress-free strain tensors of two monoclinic variants in  $a - c$  plane are given in Eq. (4.37) and (38) [18, 24]:

$$\mathbf{C}_{ijkl}^T = \begin{bmatrix} 361 & 100 & 62 & 0 & 0 & 0 \\ 100 & 361 & 62 & 0 & 0 & 0 \\ 62 & 62 & 264 & 0 & 0 & 0 \\ 0 & 0 & 0 & 59 & 0 & 0 \\ 0 & 0 & 0 & 0 & 59 & 0 \\ 0 & 0 & 0 & 0 & 0 & 64 \end{bmatrix} \text{GPa}, \quad (4.35)$$

$$\mathbf{C}_{ijkl}^M = \begin{bmatrix} 327 & 142 & 55 & 0 & 0 & -21 \\ 142 & 408 & 196 & 0 & 0 & 31 \\ 55 & 196 & 258 & 0 & 0 & -18 \\ 0 & 0 & 0 & 100 & -23 & 0 \\ 0 & 0 & 0 & -23 & 81 & 0 \\ -21 & 31 & -18 & 0 & 0 & 126 \end{bmatrix} \text{GPa}, \quad (4.36)$$

$$\varepsilon_{ij}^{00}(1) = \begin{bmatrix} 0.0419 & -0.0761 \\ -0.0761 & -0.0181 \end{bmatrix}, \quad (4.37)$$

$$\varepsilon_{ij}^{00}(2) = \begin{bmatrix} 0.0419 & 0.0761 \\ 0.0761 & -0.0181 \end{bmatrix}. \quad (4.38)$$

Table 4.1 shows the other model parameters used in the simulations.

Table 4.1 Model parameters.

Parameters	Values
$a, b, c, d,$ and $n$ in Eq.(4. 8)	2.64, 10.04, 5.37, 3.05, and 1.1 [53]
$\sigma_{y0}$ and $H$ in Eq.(4. 13)	3000 MPa and 10 GPa, and 1 [16]
$B$ in Eq.(4. (11)	$1 \times 10^{-9} \text{ Jm}^{-1}$ [16]
$L$ in Eq.(4. 14) and $\mu$ in Eq.(4. 20)	$5 \times 10^{-9} \text{ Pa}^{-1}\text{s}^{-1}$ [53]
$\alpha, \beta, \gamma, k_i,$ and $G$ in Eq.(4. 29) and Eq.(4. 30)	1, 1, 1, $2 \times 10^{-16} \text{ m}^2$ , and 1 Pa
$\vartheta$ in Eq.(4. 31)	$2 \text{ Pa}^{-1}\text{s}^{-1}$

It should be noted that we select  $\alpha, \beta, \gamma$  in the PF polycrystal model in a way that the shape of the source energy,  $f$  in Eq.(4. 29), is a double well, and the value of  $f$  at  $\zeta = 1$  is negative and lower than  $f$  at  $\zeta = 0$ . This makes  $\zeta = 1$  the most stable phase in the system and  $\zeta$ s start to evolve upon starting the simulation if the initial value is slightly larger than zero. In addition, the  $k_i$  determine the interface thickness and must be selected small enough to guarantee a reasonable and physical thickness for the interfaces (the transition thickness from one OP to another OP). In appendix B , the interface thickness calculation for a 1D steady state case is explained in detail.

## 4.5 Results and Discussion

First, the cyclic stress-strain curves and the PSA for a polycrystalline model with random grain orientations are presented. The findings from this initial model serve as the primary reference for evaluating the results of other models with different microstructural features. In the subsequent subsections, different strategies to mitigate PSA are investigated. At the end of this

section and to further elucidate the findings of this research, we conduct a cross-correlation data analysis to demonstrate the correlation between microstructural features, PSA, and MPT fraction.

To create the polycrystalline models, we only solve the polycrystal PF equation (Eq.(4.29)), and Figure 4.2(a) depicts the obtained microstructure. To make the OPs ( $\zeta_i$ ) evolve, we consider a random distribution of initial values larger than zero and smaller than 0.1 for each OP. The average GS is 0.35  $\mu\text{m}$ . A range of 0.2  $\mu\text{m}$  to 2  $\mu\text{m}$  has been reported for 3Y-STZ GS experimentally [170]. After obtaining the microstructure, a random orientation (RO) between 0° and 90° is assigned to each OP  $\zeta_i$ . The total length of GBs in this microstructure is about 84  $\mu\text{m}$ , and we calculate the GBD by dividing the total length of GBs by the total area of 16  $\mu\text{m}^2$ , which yields 5.3  $\mu\text{m}^{-1}$ . For more details on the GB length and GBD calculation see appendix B. It is worth mentioning that by changing  $\vartheta$  in Eq.(4. 31), the number of grains and the average GS can be controlled. The microstructure obtained from this step is used in the simulations where the effects of microstructural features on the MPT, mechanical response, and PSA are studied. To study the texture effects, models with different grain orientations are built, which are described later in this section.

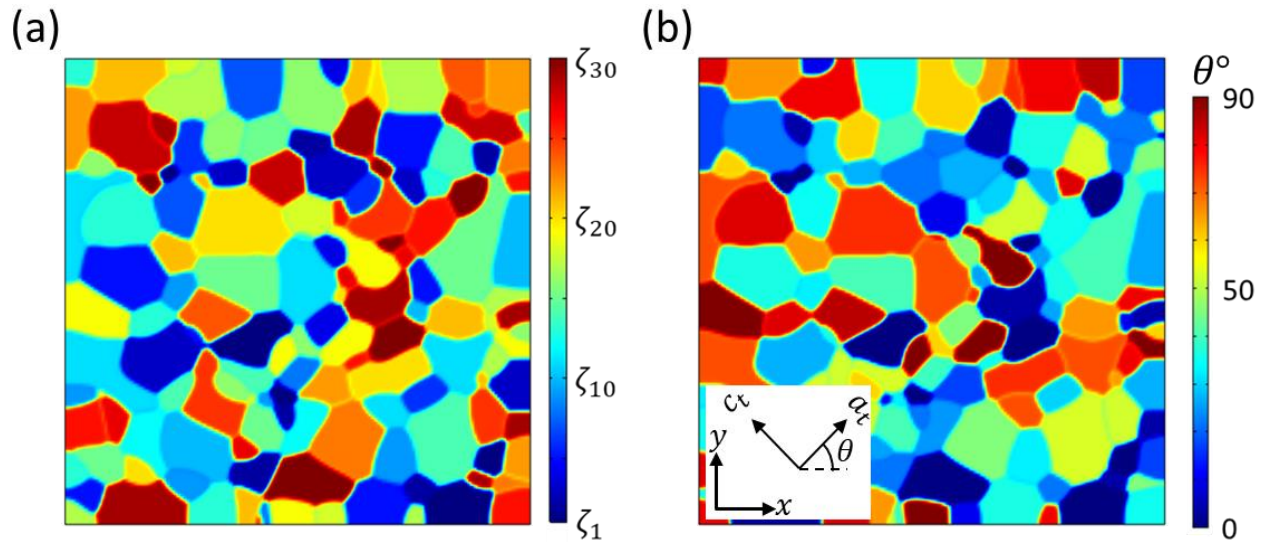


Figure 4.2 a) The obtained microstructure using 30 OPs in Eq.(4. 29, and b) Random orientations are assigned to grains.

We start with the initial model shown in Figure 4.2(a) to study the effects of grain orientation, GBD and pores on the PT and PSA under cyclic compressive loading. The mechanical response for cycle 1 (C1), 3 (C3), 7 (C7), and 9 (C9) is presented in Figure 4.3. In the stress-strain plot, the stress refers to the absolute value of average stress in the loading direction ( $\sigma_y$ ) and the strain refers to absolute value of engineering strain in the loading direction ( $\varepsilon_y$ ). From C1 to C7, after each cycle the forward transformation starting stress decreases and the hysteresis loop becomes narrower. However, there is not a notable difference between hysteresis loops of C7, C8 (not plotted) and C9. In other words, the system stabilizes (known as training effect [6, 171]) after 7 cycles. This behavior was experimentally observed in other shape memory materials [171]. Depending on the material properties and boundary conditions, the number of cycles after which stabilization happens can widely change. Lai et al [5], reported 10 cycles for a coarse-grained zirconia-based SE SMC micropillar under compressive loading. Du et. al [6], reported 81 cycles before the stabilized hysteresis loop was observed in a single crystal zirconia-based spherical sample under compression loading.

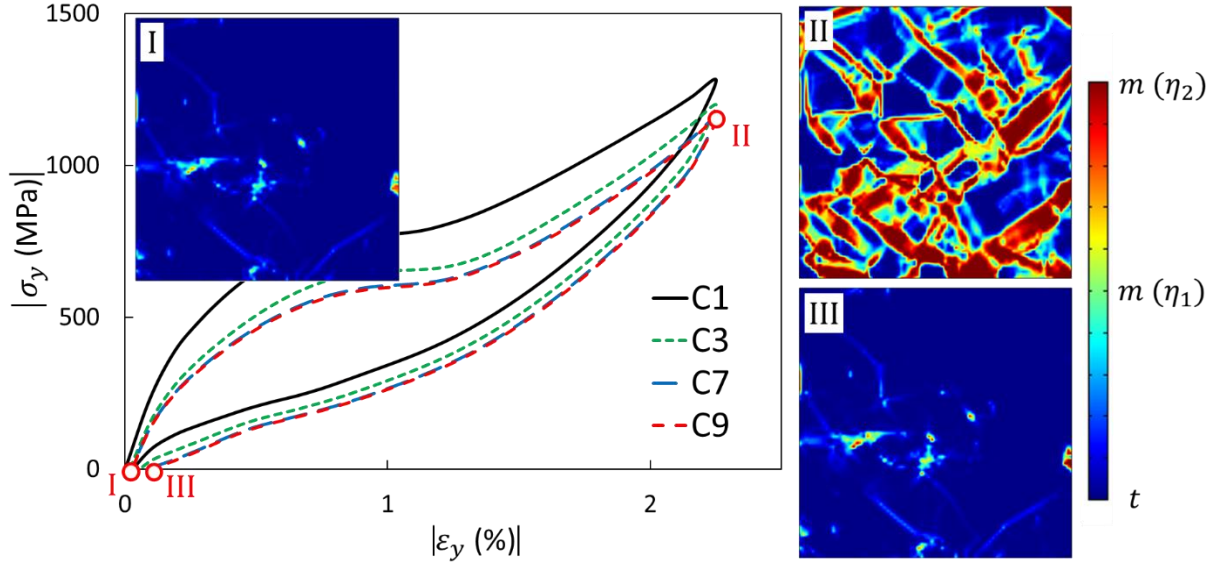


Figure 4.3 Mechanical response ( $|\sigma_y|$  vs.  $|\varepsilon_y|$ ) of C1, C3, C7, and C9; MPT map at the beginning (I), end of loading (II), and end of unloading (III) of C9.

Figure 4.3 also displays the MPT at the beginning of loading (I), end of loading (II), and the end of unloading (III) of C9. Both monoclinic variants are present at the end of loading (II), and since the system is in the SE regime, after unloading most of the transformed regions transform back to the tetragonal phase. However, there are some regions that do not transform back. This occurs due to PSA near or at GBs. The plastic strain causes the accumulation of residual stress upon unloading and consequently, pockets of martensite are left behind. This process occurs in each cycle. In addition, at the end of loading, the grains with an angle between  $10^\circ$  and  $60^\circ$  show MPT and grains with an angle outside this range do not show noticeable MPT.

Figure 4.4 presents the plot of average PSA ( $|\overline{\varepsilon^{pl}}|$  Eq. (4.27)) in percent over the entire domain. There is a PSA of 0.047% after C1, and the accumulation rate decreases in each additional cycle. This observation is consistent with experimental results of PSA in polycrystalline materials under cyclic loadings [154].  $|\overline{\varepsilon^{pl}}|$  keeps on accumulating in each cycle even after C7 ( $|\overline{\varepsilon^{pl}}| = 0.074\%$ ) after which the mechanical response stabilizes. This explains the

fatigue failure in these materials. In other words, when polycrystalline materials including ceramics are under cyclic loading, with each additional cyclic loading not only new plastic sites emerge, but also in the regions that already experienced plastic deformation, the plastic strain keeps on increasing until it locally reaches a critical value after which microscopic fatigue cracks can initiate. Then the microscopic fatigue cracks start to grow until total failure happens. In addition, the cyclic plastic strain in these ceramics is a result of the accumulation of irreversible mechanisms such as slip [8] and GB sliding [147] which we model these mechanisms by a general von mises based viscoplasticity model. Since SMCs are brittle, the number of cycles from fatigue crack initiation to total failure is very limited [6], and if the fatigue crack initiation is delayed by reducing the PSA, their lifetime can increase significantly. It is worth mentioning that the PSA starts from 0.047% after C1 and reaches 0.094% at the end of C9. These values are in good agreement with the residual strain shown in experimental cyclic stress-strain curves [5]. This also confirms that the value of  $\mu$  in the viscoplasticity model is reasonable. It is worth mentioning, to find a proper value for  $\mu$ , we used stress-strain curves reported by deformation experiments of few grains micropillars [5]. We ran few grains simulations and tried different  $\mu$  to produce reasonable stress-strain curves with a focus on values of cyclic PSA.

Figure 4.4 also shows the equivalent plastic strain distribution ( $\varepsilon_{eq}^{pl}$ ) in the domain at the end of C1, C3, and C9. The PSA is highest in triple junctions of GBs and keeps on increasing in each cycle. This cyclic increase of plastic strain is consistent with experimental materials [154] and numerical [151] studies on cyclic response of polycrystalline shape memory materials. This means triple junctions are critical sites that fatigue cracks possibly initiate from and lead to intergranular cracks. These results are consistent with experimental observation of fracture in SMCs [6, 7]. The PSA can be used as a parameter to compare the cyclic life before fatigue crack

initiation in different cases [32, 144]. In the following, we aim to study different microstructural features such as grain orientation, GBD, and pores in order to reduce the overall PSA in the polycrystalline samples.

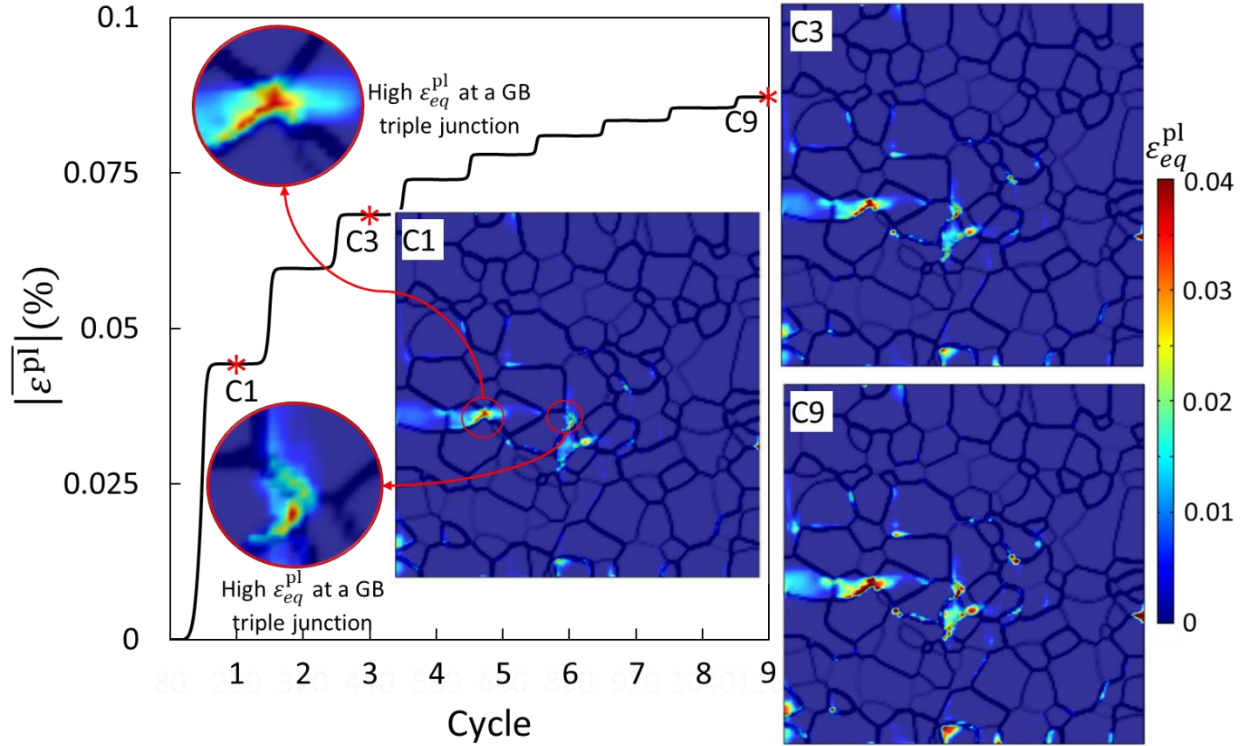


Figure 4.4 PSA plot; Equivalent plastic strain maps are shown at the end of unloading of C1, C3 and C9.

#### 4.5.1 Effects of grain boundary density

Based on the results presented in Figure 4.4, GBs are critical sites at which plastic strain is highest. Therefore, through reducing the GBD, the PSA can be mitigated. In this subsection, we explore the effects of GBD through two different approaches. In the first approach, we reduce the GBD by cutting two small sub domains (S1 and S2) of  $1\mu\text{m} \times 2\mu\text{m}$  from the initial model. These sub domains are shown in Figure 4.5. In these sub domains the average GS remains the same as the initial model, which is  $0.35\mu\text{m}$ . In addition, the grain orientations remain random in

both S1 and S2. The calculation of the GBD leads to  $3.8 \mu\text{m}^{-1}$  and  $3 \mu\text{m}^{-1}$  for S1 and S2, respectively. Figure 4.5 shows the comparison of the  $|\overline{\varepsilon}^{\text{pl}}|$  in these sub domains with the initial model. The inset figures in the bottom of Figure 4.5 (a) show the MPT in both sub domains at the end of loading of C9. In both S1 and S2, the  $|\overline{\varepsilon}^{\text{pl}}|$  is predicted to be lower than the initial model ( $4\mu\text{m} \times 4\mu\text{m}$ ). This result suggests that by reducing the GBD through making the sample size smaller,  $|\overline{\varepsilon}^{\text{pl}}|$  can be mitigated noticeably. One can also expect that for larger samples, a lower GBD will result in lower  $|\overline{\varepsilon}^{\text{pl}}|$ .

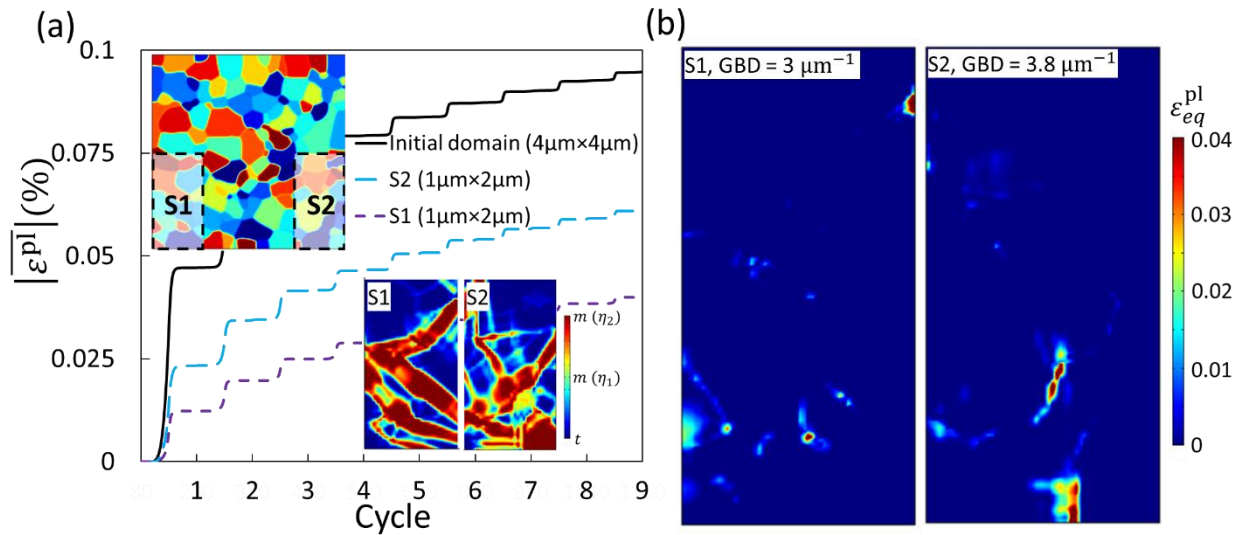


Figure 4.5 a) The PSA in the initial model, S1, and S2 sub domains; Inset-Top) the location of sub domains S1 and S2 in the initial model; Inset-Bottom) the MPT in S1 and S2 at the end of loading of C9; b) the equivalent plastic strain in S1 and S2 at the end of C9.

Few experimental studies also investigated the effects of GBD on the fatigue life zirconia-based SMCs. Lai et al. [5] produced ceria and yttria stabilized zirconia micropillars with fewer grains and GBs by reducing the diameter of micropillars, and they applied cyclic compressive and bending loadings to the samples. They observed large strains up to 7% and the ability to cycle reversibly through the MPT up to 50 cycles before failure occurs. Furthermore, Du et al. [6] produced oligocrystalline and single crystal spherical samples to mitigate the

cracking problems in cyclic loading of polycrystalline zirconia-based SMCs. The reduced number of grains and GBs as well as lowering the diameter of the spherical samples resulted in lowering the GBD. They were able to observe up to 110 SE cycles in some samples with a diameter less than 4  $\mu\text{m}$  under cyclic compressive loading. We can conclude that model prediction is consistent with experimental observations and the PSA is an effective indicator of cyclic life in polycrystalline materials.

In the second approach for studying the effect of GBD, we produced coarse-grained microstructure by increasing the GS to reduce GBD. To increase the average GS, we increased the mobility parameter in Eq.(4. 31) to  $30 \text{ Pa}^{-1}\text{s}^{-1}$ . Figure 4.6(b, top row) shows the obtained microstructure and grain orientations, where the average GS is  $\sim 1 \mu\text{m}$ , the total length of the GBs is  $\sim 33 \mu\text{m}$ , and the GBD is  $2.03 \mu\text{m}^{-1}$ . We study two different cases: RO ( $\theta$  between  $0^\circ$  and  $90^\circ$ ) and texture 1 (TX1) ( $\theta$  between  $0^\circ$  and  $30^\circ$ ). Figure 4.6(a) shows plots of  $|\overline{\varepsilon^{\text{pl}}}|$  for the initial model (GS =  $0.35\mu\text{m}$ , GBD =  $5.3 \mu\text{m}^{-1}$ , RO), coarse-grained microstructure with RO (GS =  $1\mu\text{m}$ , GBD =  $2.06 \frac{1}{\mu\text{m}}$ , RO), and coarse-grained microstructure with texture (GS =  $1\mu\text{m}$ , GBD =  $2.06 \mu\text{m}^{-1}$ , TX1). Figure 4.6(b, bottom row) shows the plastic strain distribution throughout the domain for both coarse-grained cases. The inset figures show the MPT for both coarse-grained cases. Figure 4.6 results indicates that by reducing the number of GBs and GBD through increasing the GS,  $|\overline{\varepsilon^{\text{pl}}}|$  can be significantly mitigated. This observation can be explained based on two concepts; first, by reducing the number of grains in the domain, the number of triple junctions, GBs, and GBD decreases, and this leads to a lower PSA. Second, the GBs are non-transforming regions, and they halt MPT. Therefore, by reducing the number of GBs, the MPT develops larger bands and occurs easier without being stopped at the GBs and this

makes the MPT the dominant energy dissipation mechanism in the system, therefore reduces the energy dissipation through plastic deformation.

The TX1 results shows that by reducing the number of GBs as well as tailoring the grains orientation,  $|\overline{\varepsilon^{pl}}|$  can be drastically lowered, and this will lead to a significant higher cyclic life. This result can be used as a guide for future experimental studies and design of SMCs.

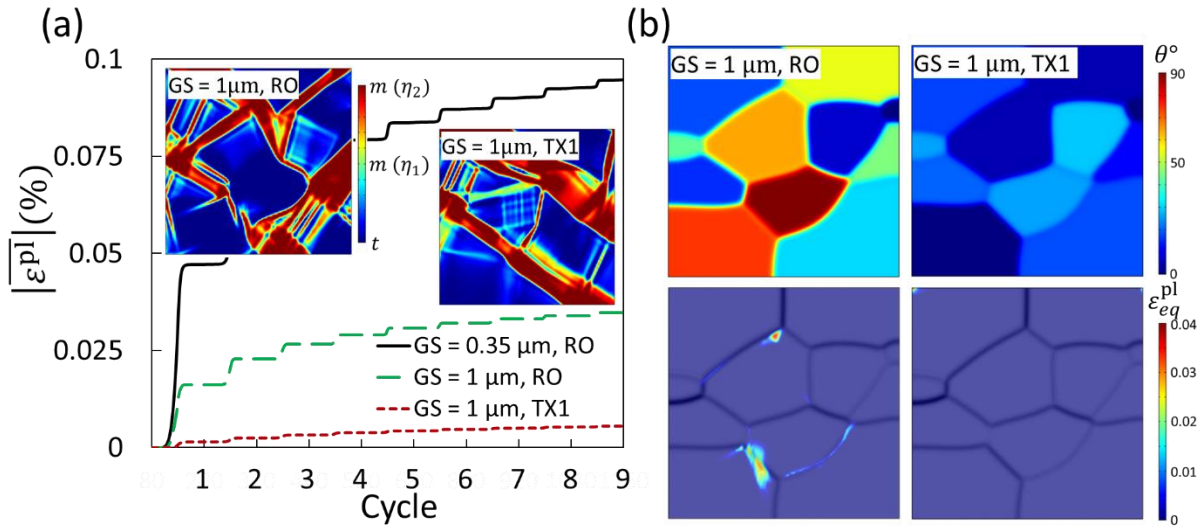


Figure 4.6 (a) The PSA versus number of loading cycles; Inset) MPT for RO and TX1 cases at the end of loading of C9; (b) the microstructure and grains orientation (top row), and the equivalent plastic strain in the domains at the end of C9 (bottom row).

#### 4.5.2 Effects of grain orientations

The result of TX1 revealed that the grain orientation has a large impact on the PSA. This result guides us to investigate the effects of textures in more detail. In this subsection we investigate the effects of strong textures by considering three different textures in the initial domain (GS = 0.35  $\mu\text{m}$ ) and compare the results with the case where grains have random orientations between  $\theta = 0^\circ$  and  $\theta = 90^\circ$ , presented in Figure 4.3 and Figure 4.4. In texture 2 (TX2) a random orientation between  $\theta = 0^\circ$  and  $\theta = 30^\circ$ , in texture 3 (TX3) a random orientation between  $\theta = 35^\circ$  and  $\theta = 45^\circ$ , and in TX4 a random orientation between  $\theta = 60^\circ$

and  $\theta = 90^\circ$ , all with respect to the loading direction, is considered for each grain. The same polycrystal microstructure used in previous simulations is considered.

Figure 4.7 (a) displays the PSA for different grain orientations of RO, TX2, TX3, and TX4. The inset figures present the MPT map for these textures. By comparing these results to Figure 4.4, we can conclude that grain orientation plays a drastic role in PSA and MPT. TX2 leads to a noticeable lower  $|\overline{\varepsilon^{pl}}|$ , and TX4 leads to a drastically higher  $|\overline{\varepsilon^{pl}}|$  compared to RO. In addition,  $|\overline{\varepsilon^{pl}}|$  is the lowest in TX2 among all textures. In TX2 and TX3 cases, since most grains are oriented in a direction that MPT happens, a large portion of the elastic energy is dissipated through MPT and not plastic deformation. In addition, both TX2 and TX3 have a lower plastic deformation than the RO case, therefore, a higher cyclic life is expected compared to RO. In TX4 case, the transformed domains are smaller, and they are limited to limited number of grains with angles between  $60^\circ$  to  $70^\circ$ . The main mechanism of energy dissipation is plastic deformation, and this leads to a higher PSA and consequently a lower cyclic life before fatigue crack initiation is expected.

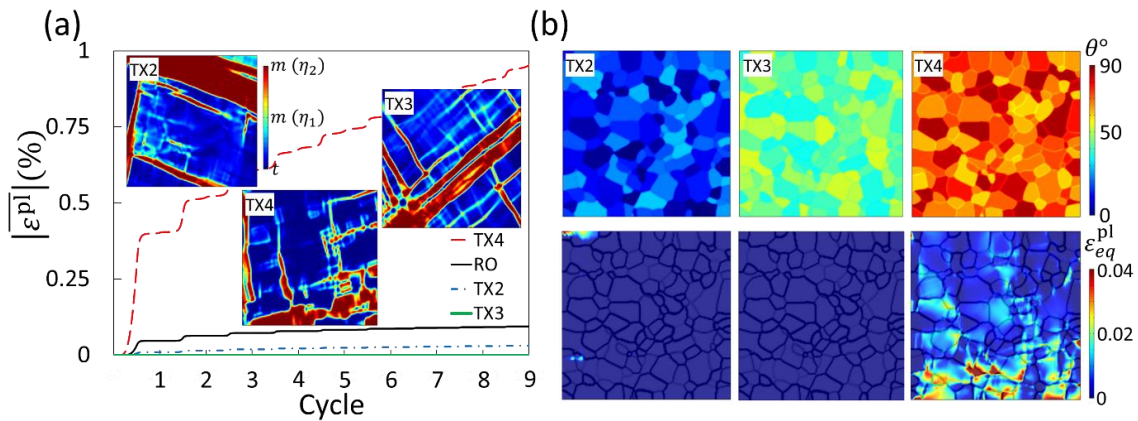


Figure 4.7 (a) PSA plots; Inset) MPT for TX2, TX3 and TX4 at the end of loading of C9; (b) TX2 and TX3 grains orientation (top row), and equivalent plastic strain in TX2, TX3 and TX4 cases at the end of C9 (bottom row).

### 4.5.3 Effects of engineered pores

MPT in zirconia-based SMCs is accompanied by large localized deformations due to phase expansion. If the material is not able to accommodate the large deformations and mismatch stresses, cracks will emerge after few cycles of loading [5-7, 138]. In this section, we study the effect of pores on plastic deformation. We first consider a random distribution of pores and then we investigate the effects of pores located closer to GBs. These pores can generate during manufacturing processing or service as a result of volume change due to MPT or high localized stress mainly at GB junctions or around material inclusions [18, 172]. Different manufacturing techniques and inclusions can be used to engineer the GBs and inclusions' sites and consequently the location of possible pores [172]. Engineered pores may provide space for phase expansion when the material undergoes MPT and consequently decrease the plastic deformation. We study this hypothesis by considering five different PVF of 0.5%, 1%, 1.5% , 2% , and 2.5%. For PVF of 0.5% and 1% two different pore radiuses ( $r$ ) of 0.04  $\mu\text{m}$  and 0.06  $\mu\text{m}$  are considered, and for PVF of 1.5%, 2% , and 2.5% only pores with a radius of 0.06  $\mu\text{m}$  are considered. The same microstructure and grain orientation distribution as initial model (Figure 4.3) is considered for all cases with pores. Figure 4.8(a) shows the plot of  $|\overline{\varepsilon^{pl}}|$  for different PVF and pore radiuses; the case labeled "without pores" refers to the initial model shown in Figure 4.3 and Figure 4.4. Figure 4.8(b) presents the plastic strain distribution in the domains with PVF of 0.5% and 1% with different radiuses of 0.04  $\mu\text{m}$  and 0.06  $\mu\text{m}$ . There is not a noticeable difference in the MPT pattern with pores compared to the initial model shown in Figure 4.4. Based on Figure 4. 8(a), in the most studied cases, the existence of pores reduces  $|\overline{\varepsilon^{pl}}|$ , therefore leads to a higher cyclic life. This can be explained based on the fact that pores provide more room for the system to accommodate the expansion due to the MPT and this

alleviates the mismatch stresses and reduced the PSA at GBs. However, for the PVF higher than 2%,  $|\overline{\varepsilon^{pl}}|$  increases with a high slope rather than staying flat after cycle 3. Based on Figure 4.8(a), for cases with PVF of 2% and 2.5%,  $|\overline{\varepsilon^{pl}}|$  even becomes higher than the case with PVF of 1.5% at the end of C9, and the difference is expected to become larger after C9. These results suggest that pores can reduce the  $|\overline{\varepsilon^{pl}}|$ , however there is a threshold for the PVF.

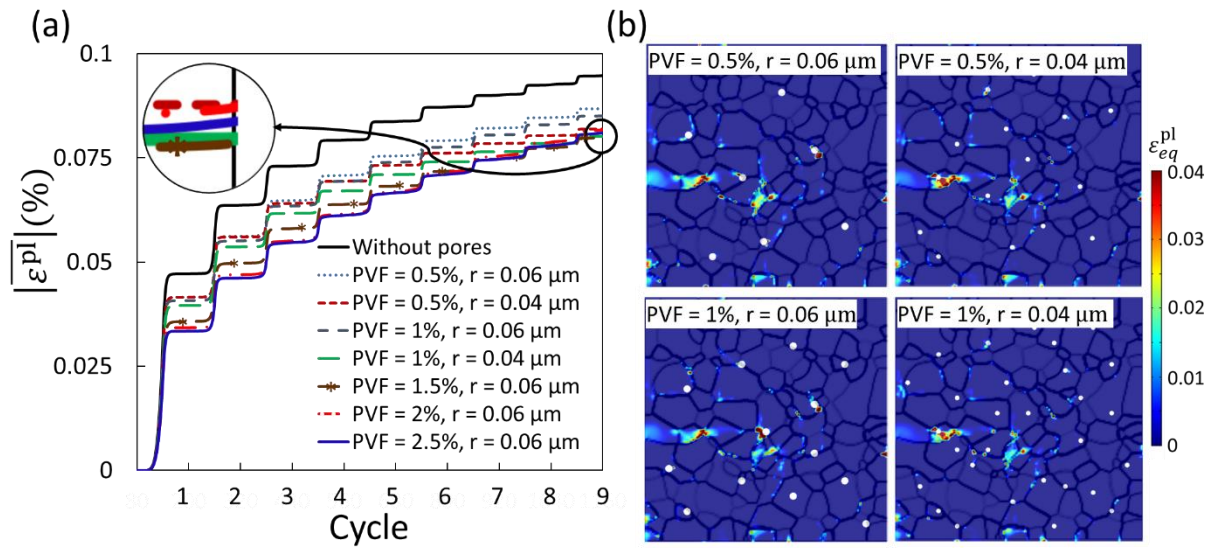


Figure 4.8 (a) PSA plots for different PVF and pore size, and (b) equivalent plastic strain in the domains with randomly distributed pores at the end of C9 for 4 different cases.

As far as pore radius, the smaller radius leads to a lower  $|\overline{\varepsilon^{pl}}|$  for the same PVF. This result shows that the number of pores plays a pivotal role. For the same PVF, a smaller pore radius leads to a higher number of pores, which means in more locations over the domain the phase expansion due to MPT can be accommodated and this leads to a lower  $|\overline{\varepsilon^{pl}}|$ . In addition, these results show that pore radius of 0.04 μm is still large enough to accommodate the shape change due to the MPT. In Figure 4.8 for all seven cases, pores are randomly distributed over the domain. Since GBs are crucial regions with the highest PSA, we conduct new studies by locating

the pores on the GBs with the highest plastic strain. A PVF of 0.5% at GBs (PVFGBs) and two different pores radiuses of  $r = 0.04 \mu\text{m}$  and  $r = 0.06 \mu\text{m}$  are considered.

Figure 4.9(a) shows the plots of  $|\overline{\varepsilon}^{\text{pl}}|$  for the new cases against the case without pores (the initial model) and the case with PVF = 0.5% of randomly distributed pores. By locating pores on the GBs,  $|\overline{\varepsilon}^{\text{pl}}|$  decreases significantly compared to the case with randomly distributed pores. The case of PVFGBs = 0.5% with  $r = 0.04 \mu\text{m}$  reduces  $|\overline{\varepsilon}^{\text{pl}}|$  by 30% with respect to PVF = 0.5% and  $r = 0.04 \mu\text{m}$ , and 38% with respect to the case without pores. These results confirm that GBs are critical regions and by providing space near GBs to accommodate the phase expansion due to the MPT, the cyclic life before fatigue crack initiation can be increased.

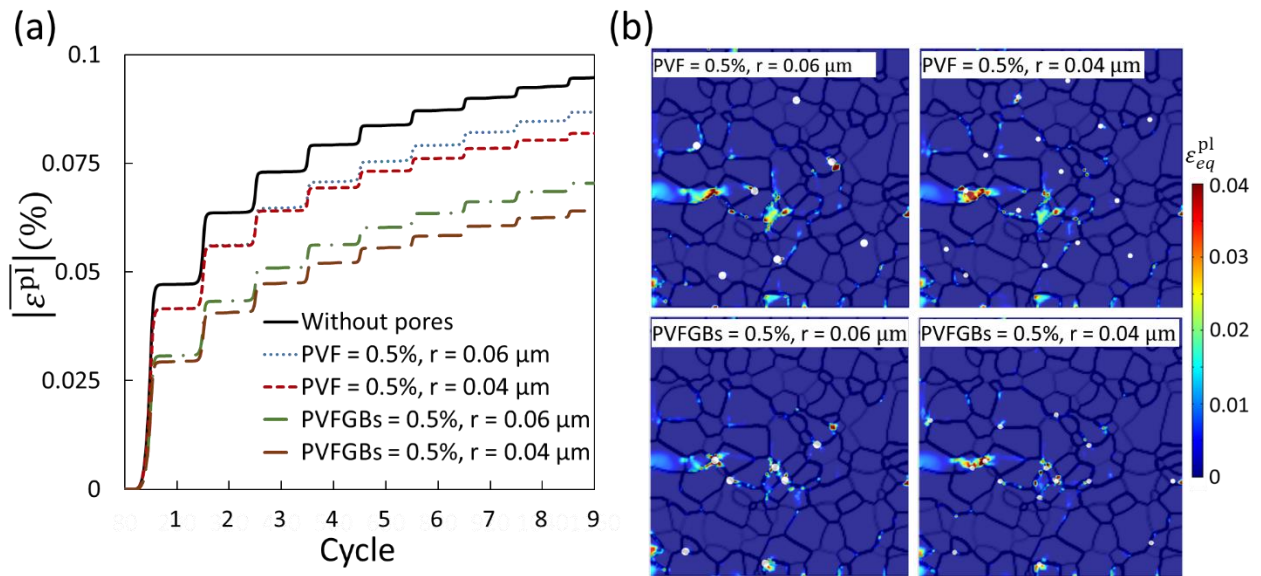


Figure 4.9 (a) PSA plot; (b) the equivalent plastic strain distribution in the domains with randomly distributed pores at the end of C9 (top row) and in the domains with pores located at GBs at the end of C9 (bottom row).

#### 4.5.4 Analysis of parameters controlling PSA

In this section, we apply a cross-correlation data analysis approach to study the relationship between the microstructural features, the PSA and the MPT fraction (at the end of

loading of C9) through a heatmap. To calculate the MPT fraction we use the equation of

$$\frac{1}{A_{total}} \sum_{i=1}^2 \eta_i A_i$$

where  $A_i$  is the area of  $i$ th monoclinic variant and  $A_{total}$  is the total area of the

domain. The correlation matrix is calculated based on the Pearson approach [173, 174] using a correlation coefficient ( $r$ ) which can vary between  $-1$  and  $1$ . If the value is positive, then it means there is a direct correlation between two variables, meaning by increasing one variable the other variable increases as well. If the value is negative, it means there is an inverse correlation, meaning when one variable increases the other variable decreases. If the value is zero, there is no correlation between the two variables. In addition, if the value is closer to  $1$  or  $-1$  there is a stronger positive or negative correlation, respectively. The correlation is calculated based on the below equation:

$$r = \frac{\sum(x_i - \bar{x})(y_i - \bar{y})}{\sqrt{\sum(x_i - \bar{x})^2 \sum(y_i - \bar{y})^2}} \quad (4.39)$$

where  $x_i$  are different values of variable  $x$  in a sample,  $\bar{x}$  is the mean of  $x_i$ ,  $y_i$  are different values of variable  $y$  in a sample, and  $\bar{y}$  is the mean of  $y_i$ .

We consider two target variables of  $|\overline{\varepsilon^{pl}}|$  (at C9) and MPT fraction (at the end of loading of C9), and four attribute variables of pores size (PS), PVF, average grain orientations of textured samples (AGOTX) with respect to loading direction, and GBD. Figure 4.10 shows the obtained heatmap.

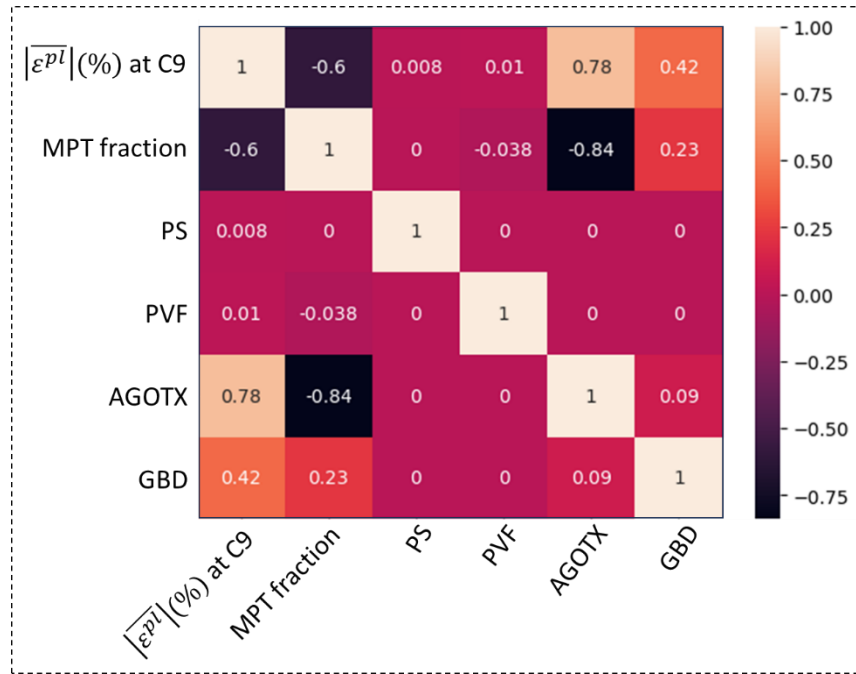


Figure 4.10 The correlation between the studied microstructural features and two target variables of  $|\overline{\varepsilon}^{pl}|$  (at C9) and MPT fraction (at the end of loading of C9).

The plastic deformation and MPT are two energy dissipation mechanisms, and the high negative correlation of -0.6 indicates that only one of them can be the dominant energy dissipation mechanism in a system. The heatmap also shows that the highest correlation is between MPT fraction and the average grain orientations with respect to the loading direction in a textured sample (AGOTX). The correlation is negative (-0.84) which means by increasing the average grain orientation in the textured cases, MPT decreases and therefore MPT would not be the dominant source of energy dissipation and plastic deformation will be the main source of energy dissipation. This is why the heatmap predicts a high positive correlation of 0.78 between AGOTX and  $|\overline{\varepsilon}^{pl}|$ . In addition, the heatmap shows a relatively high correlation of 0.42 between GBD and  $|\overline{\varepsilon}^{pl}|$ . As expected, this correlation is positive since in the previous sections, we showed that by reducing GBD,  $|\overline{\varepsilon}^{pl}|$  decreases noticeably. Furthermore, the heatmap presents a positive correlation between  $|\overline{\varepsilon}^{pl}|$  and PVF and PS. However, these correlations are small, and

this is because based on the results,  $|\overline{\varepsilon^{pl}}|$  can decrease more by changing the AGOTX and GBD compared to applying pores to the system. Based on the previous results in this paper and what the heatmap presents, the AGOTX has the highest effect in controlling  $|\overline{\varepsilon^{pl}}|$ , then the GBD plays the most effective role, and next is the pore volume fraction.

#### 4.6 Conclusions

We integrated a phase-field MPT model with a viscoplasticity model to investigate the effects of microstructural features, such as grains orientation, pores, GBs, as well as domain size on MPT and PSA in polycrystalline SMCs subjected to compressive cyclic loading. We used average PSA as an indicator of cyclic life, aiming to enhance the material's ability to withstand a higher number of cycles before fatigue crack initiation by reducing average PSA.

In these materials, the previous experimental and computational studies have established that the plastic strain originates from irreversible mechanisms such as slip and GB sliding. To simulate plastic strain, we employed a straightforward viscoplasticity model with a few constants that require determination. Our results showed that this model is capable of predicting cyclic plastic strains effectively, aligning quantitatively with available experimental reports.

Our simulations predicted a high plastic strain at the GBs particularly at triple junctions, and this result is consistent with experimental observations. Given that GBs are critical sites with the highest plastic strain, we studied the effects of GBD on PSA. The model predicts a lower PSA if GBD is lowered achieved by domain size reduction or increased average GS. The results on the domain size effects are in good agreement with existing experimental observations. Furthermore, our research reveals that engineered pores can play a more effective role in reducing the PSA when located close to the GBs. This can be attributed to pores offering space

to accommodate the expansion due to MPT. However, we have identified a threshold for PVF; if PVF exceeded 2%, additional porosity may play a negative role and increase PSA and consequently decrease the cyclic life. Our model also captures the impact of grain orientations effectively. Textured microstructures with grains oriented close to 45° with respect to the loading direction exhibited drastic reduction in PSA, primarily due to MPT becoming the dominant energy dissipation mechanism. This phenomenon could lead to significantly enhanced cyclic life in polycrystalline SMCs.

The ideas and simulations presented in this study for reducing PSA in polycrystalline shape memory materials represent novel contributions not explored in previous experimental or computational studies. The primary purpose of this study was to offer insights for future research on tailoring the microstructure to enhance the cyclic life of SMCs. In addition, the model presented in this research is extendable to other polycrystalline shape memory materials.

#### 4.7 Appendix B

Here we explain the approach used for calculating the GB length and GBD. With the solution to Eq.(4. 29) (the PF polycrystalline model) at hand, we assign a grain orientation to each grain according to Eq. (4.40).

$$\theta = \theta_1 \times \zeta_1 + \theta_2 \times \zeta_2 \dots \theta_{30} \times \zeta_{30}, \quad (4.40)$$

where  $\theta_i$  is the selected orientation for grain  $i$ .

Now, the GBs are identified with the following equation and dGB field is shown in Figure 4.40:

$$dGB = \sqrt{\left(\frac{d\theta}{dx}\right)^2 + \left(\frac{d\theta}{dy}\right)^2} m^{-1} \quad (4.41)$$

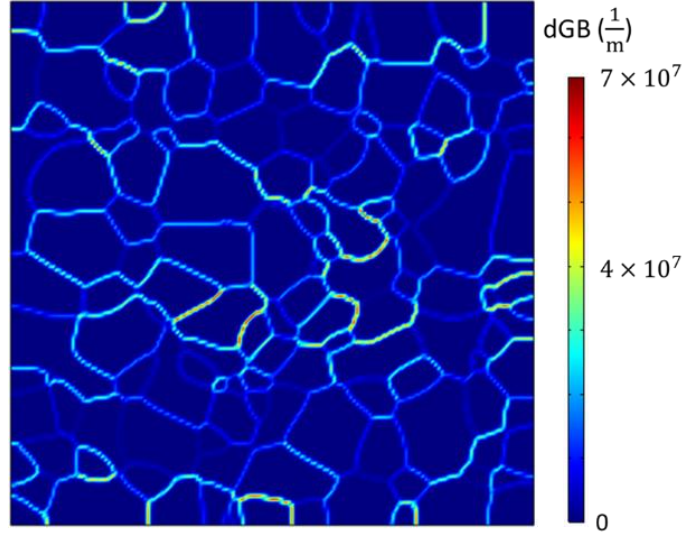


Figure 4.11 The distribution of dGB.

Eq. 4.41 calculates the magnitude of the gradient of  $\theta$  over the domain, and this equation yields different values for different GBs. The value of dGB depends on the misorientation angle between two neighboring grains. In addition, this number is  $\sim 0$  inside the grains.

Now, we calculate the minimum value for dGB which we consider representing a GB. First, we consider the steady state problem in a 1D domain with only one OP  $\zeta$ . Therefore the Eq. (4.29)-(4.31) become:

$$F(\zeta(x)) = G \int_V \left( f + \frac{k}{2} (\nabla \zeta(x))^2 \right) dV, \quad (4.42)$$

$$f = \sum_{i=1}^s \left( -\frac{\alpha}{2} \zeta(x)^2 + \frac{\beta}{4} \zeta(x)^4 \right), \quad (4.43)$$

$$0 = -\alpha \zeta(x) + \beta \zeta(x)^3 - k \nabla^2 \zeta(x) \quad (4.44)$$

Considering  $G = 1\text{Pa}$ ,  $\alpha$  and  $\beta$  equal to 1 (see Table 4.1), the Eq. 4.44 recovers the steady state Allen-Cahn equation [125]. It is worth mentioning that we consider  $k = 2 \times 10^{-16} \text{ m}^2$  (Table 4.1). Applying the boundary conditions of  $\zeta(+\infty) = +1$  and  $\zeta(-\infty) =$

$-1$  yields an analytical solution of  $\zeta(x) = \tanh\left(\frac{x}{\sqrt{2k}}\right)$  which is plotted in Figure 4.12 in a domain size of  $0.2 \mu\text{m}$ . From the profile shown in Figure 4.12, we define the width of the smeared interface as the intersection of the tangent line ( $\zeta_t$ ) at  $x = 0$  with  $\zeta = \pm 1$ . This yields an interface width of  $2\sqrt{2k} \approx 0.04 \mu\text{m}$ . It is worth noting that this GB thickness is small enough compared to the domain size, and for this microscale study, using a smaller GB thickness does not noticeably affect the results.

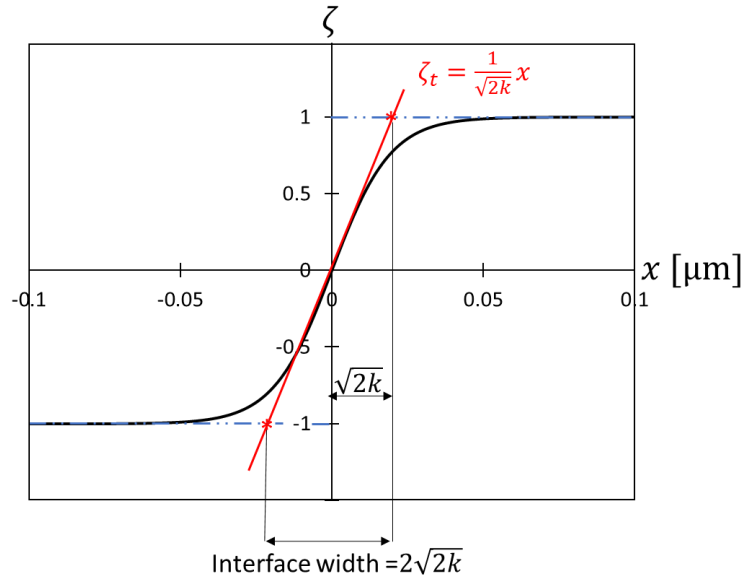


Figure 4.12 The analytical solution of Eq.(4.44) ( $\tanh\left(\frac{x}{\sqrt{2k}}\right)$ ) and the process of calculating the smeared interface width.

Now, we consider that two grains are separated when they are misoriented by at least  $\Delta\theta_{min} = 0.105$  radians over the width of the smeared interface. Therefore, the minimum value of dGB to define a GB is:

$$dGB_{min} = \frac{\Delta\theta_{min}}{2\sqrt{2k}} = 2.6 \times 10^6 \text{m}^{-1} \quad (4.45)$$

By applying the above constraint, the plot of dGB is shown in Figure 4.13.

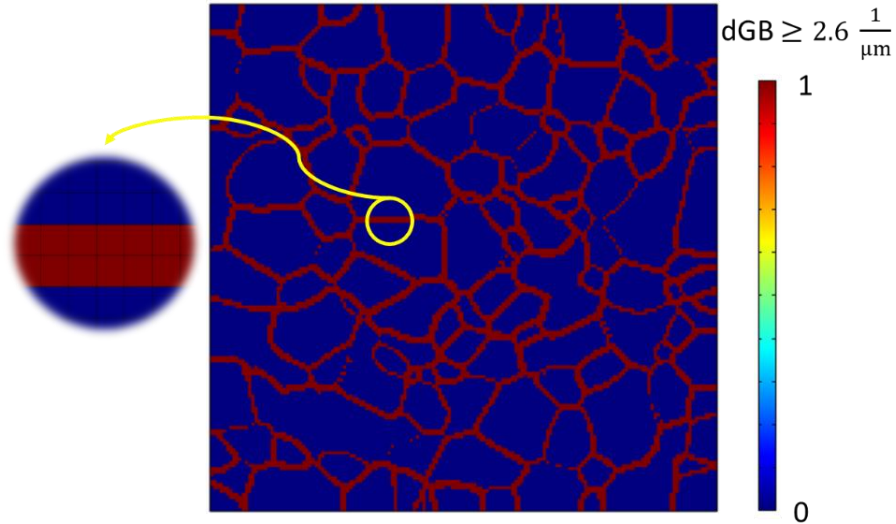


Figure 4.13 The distribution of  $dGB \geq 2.6 \times 10^6 \text{ m}^{-1}$

By integrating  $dGB$  over the entire domain we will obtain the total area of  $dGB$ . By dividing this area by the size of two elements (based on Figure 4.13, the  $dGB$  is over two elements for almost all GBs, the size of each element is  $0.02\mu\text{m}$ ), we can calculate the total length of GBs. To calculate the GBD, we divide the total length of GBs by the domain area. For example, for the case of Figure 4.13, the GB length calculation yields  $84 \mu\text{m}$  and GBD is calculated by dividing the GB length by the domain area ( $16 \mu\text{m}^2$ ) which yields  $5.3 \mu\text{m}^{-1}$ .

## CHAPTER 5

### A 3D PHASE-FIELD MODEL FOR PREDICTING ORIENTATION-DEPENDENT DEFORMATION AND FAILURE OF MICROPILLAR SHAPE MEMORY CERAMICS

#### 5.1 Abstract

Microscopic samples of zirconia-based shape memory ceramics (SMCs) have shown full martensitic phase transformation (MPT) over multiple loading cycles without cracking. However, it is crucial to note that the occurrence of MPT is highly influenced by grain orientation. Depending on the specific orientation of grains relative to the loading direction, alternative mechanisms such as plastic slip and fracture may emerge. We introduce a phase-field (PF) based framework coupling a PF-MPT, a PF fracture, and a crystal viscoplasticity model to examine how grain orientation impacts MPT, plastic slip, and fracture mechanisms in SMCs micropillars. We focused on single crystal micropillars to distinguish the orientations that facilitate each mechanism. We found a wide range of grain orientations in which micropillars predominantly exhibit MPT. Furthermore, micropillars with grain orientations close to (100) and (001) predominantly experience fracture, with minimal plastic slip observed. In addition, samples with (110) orientation show significant amount slip plasticity. The results obtained in this research are in good agreement with experimental data. We generated a pole figure to clarify our findings on the interplay between MPT, cracking, and slip under compressive loadings.

#### 5.2 Introduction:

Zirconia-based SMCs are a type of intelligent material known for their capacity of demonstrating either superelasticity or shape memory effect functionalities as a result of MPT. The MPT arises from phase change mainly between tetragonal (*T*) and monoclinic (*M*) phases. The shape change induced by MPT is large and due to the inherent brittleness of these ceramics,

they are often unable to accommodate such significant transformations. This is the main reason for their low fracture toughness and short cyclic life. Multiple experimental studies on microscopic samples of these ceramics have consistently highlighted GBs as critical sites for crack initiation. These investigations have demonstrated that by reducing the number of grains and consequently minimizing the presence of GBs and even generating single crystal samples, these ceramics can undergo complete MPT over numbers of loading cycles before experiencing fracture. For example, Lai et al. [5] produced micropillars with low number of grains and they observed that some samples can handle up to 55 cycles before they fractured. In addition, experimental studies have identified plastic slips as one primary irreversible mechanism in these ceramics. Zeng et al. [8] observed that depending on the crystal orientation in single crystal micropillars, these ceramics can exhibit MPT, plastic slip, fracture, or a combination of these three mechanisms.

MPT, plastic slip, and fracture are highly dependent on microstructural features and comprehensively understanding how these features influence the interplay between these mechanisms can be challenging, if not impossible, solely through experimental methods. In this case, numerical studies can be a reliable alternative to experiments. The PF method has emerged as a powerful approach for modeling both MPT and fracture in engineering materials including zirconia-based SMCs. Mamivand et al. [14] for the first time used PF method to model the transformation from T to M phase observed in zirconia-based SMCs. Their model successfully captured the crystal alternation between the two phases and accurately predicted the experimentally observed microstructure. The PF method has also been utilized to model the interaction between MPT and cracking in SMCs [20-24, 53]. For instance, Moshkelgosha and Mamivand conducted studies on fracture propagation in both single crystal [22] and

polycrystalline [23] zirconia-based SMCs using the PF method. They employed stress-controlled loading conditions. In a separate investigation by the same authors [24], they explored phase transformation and fracture in a three-dimensional single crystal SMC, observing the initiation and propagation of martensitic phase transformation (MPT) from the crack tip. Their predicted crack deflection due to MPT, consistent with experimental reports. Notably, none of these studies reported an ultimate stress or final stress drop in their stress-strain curves, primarily because of the stress-controlled loading conditions applied. Additionally, these studies focused only on SME behavior and in none the SE was considered. Furthermore, none of these models include plasticity, therefore they were not able to study the interplay between MPT, fracture, and slip. Later on, Lotfolahpour et al. [53] employed the PF method to investigate the interaction between MPT and cracking in the SE regime. They addressed a common issue of elastic modulus underestimation associated with most phase-field (PF) martensitic phase transformation (MPT) models by modifying the PF MPT formulation. They studied the effects of grain orientation on MPT and crack path and captured reverse MPT behind the crack tip. They successfully established an ultimate strength for the material under investigation by applying displacement-controlled loadings. Cisse and Asle Zaeem [16], coupled the PF MPT with a von mises based plasticity model to study the interaction between MPT and plasticity in SMCs under monolithic loading conditions. They identified GBs as critical sites with the highest plastic strain. In addition, they observed that plastic deformation impedes MPT and compromises the functionality of SMCs. There are additional studies that focus on coupling PF-MPT with plasticity, either general plasticity or crystal plasticity models, to examine the interaction between MPT and plastic deformation in shape memory materials, with a primary focus on NiTi [34, 143, 150]. However, none of previous studies have investigated MPT, plasticity, and

fracture simultaneously. Consequently, they have not been able to establish a comprehensive understanding of the interaction between these mechanisms.

In this study, for the first time we couple MPT, plastic slip, and fracture to investigate the interplay between these mechanisms in 3D domains. To achieve this, we utilize the PF method to model both MPT and fracture, while adopting a crystal viscoplasticity model to accurately represent plastic slip behavior in SMCs. We employ the model for predicting the orientation-dependent deformation and failure of micropillar SMCs. To better present our findings we illustrate the results in a pole figure.

### 5.3 Formulation

In this section, we explain the coupling of elasticity, PF MPT, and PF fracture. Then we add plastic strains, from slip systems to the inelastic strain expression and discuss the calculation of the plastic strains based on a crystal viscoplasticity model. We start the formulation by expressing the total energy of the system as:

$$F_{\text{tot}}(u_i, \eta_1, \eta_2, \dots, \eta_m) = F_{\text{el}} + F_{\text{ch}} + F_{\text{gd}} + F_{\text{fr}} \quad (5.1)$$

where  $F_{\text{el}}$  is the elastic strain energy,  $F_{\text{ch}}$  is the chemical free energy,  $F_{\text{gd}}$  is the gradient energy of the tetragonal-monoclinic or monoclinic-monoclinic interfaces, and  $F_{\text{fr}}$  is the fracture energy. These energies are explained in detail in the following.

- *Elastic strain energy* ( $F_{\text{el}}$ ):

$F_{\text{el}}$  can be written as:

$$F_{\text{el}}(u_i) = \int_V \frac{1}{2} \mathbf{g}(\phi) C_{ijkl} \varepsilon_{kl}^{\text{el}} \varepsilon_{ij}^{\text{el}} dV, \quad (5.2)$$

where  $u_i$  is the displacement,  $C_{ijkl}$  is the elastic tensor, and  $g(\phi)$  is the degradation function to account for the effects of fracture on the elastic energy. It should be noted  $g(\phi) = (1 - \phi)^2$  is one of the widely used degradation functions that we also use in this work. In addition,  $\varepsilon_{ij}^{el}$  is the elastic strain which is defined as the difference between the total strain ( $\varepsilon_{ij}^{tot}$ ), transformation strain ( $\varepsilon_{ij}^{tr}$ ), and plastic strain ( $\varepsilon_{ij}^{pl}$ ) (plastic strain calculation will be explained later in this section):

$$\varepsilon_{ij}^{el} = \varepsilon_{ij}^{tot} - \varepsilon_{ij}^{tr} - \varepsilon_{ij}^{pl}. \quad (5.3)$$

Considering a linear relation between the OPs and strains [53, 107, 109, 121],  $\varepsilon_{ij}^{tr}$  is defined as:

$$\varepsilon_{ij}^{tr} = \sum_{p=1}^m \varepsilon_{ij}^{00}(p) \eta_p, \quad (5.4)$$

where  $\varepsilon_{ij}^{00}$  is the stress-free strain tensor which represents the change in microstructure between parent and product phases [16]. The small strain assumption is considered and is defined as:

$$\varepsilon_{ij}^{tot} = \frac{1}{2} (u_{i,j} + u_{j,i}). \quad (5.5)$$

The difference between elastic constants in tetragonal and monoclinic phases is represented by the following linear relation [16]:

$$C_{ijkl}(\eta_1, \eta_2, \dots, \eta_m) = C_{ijkl}^T + \sum_{p=1}^m \eta_p (C_{ijkl}^M - C_{ijkl}^T), \quad (5.6)$$

where  $C_{ijkl}^T$  and  $C_{ijkl}^M$  are elastic constants of the tetragonal and monoclinic phases, respectively.  $m$  is the number of product phases (monoclinic variants in this study). The elastic energy defined in Eq. (5.2) is based on the Hooke's law, therefore the stress tensor is related to elastic strain tensor through the following equation:

$$\sigma_{ij}(u_i, \eta_p) = C_{ijkl}(\eta_1, \eta_2, \dots, \eta_m) \varepsilon_{kl}^{el}. \quad (5.7)$$

- *Chemical free energy ( $F_{ch}$ ):*

$F_{ch}$  determines the system's energy dissipation due to MPT. The 2-3-4 or 2-4-6 Landau polynomials defined in terms of order parameters are the most common types of  $F_{ch}$  [31].

However, these chemical energies underestimate the elastic response in the beginning of the stress-strain curve. Lotfolahpour et al. [53] proposed a modification to the 2-3-4 polynomial to address the elastic modulus underestimation, which is used in this paper:

$$F_{ch}(\eta_1, \eta_2, \dots, \eta_m) = \int_V |\Delta G| \left( a \sum_{p=1}^m \eta_p^2 - b \sum_{p=1}^m \eta_p^3 + c \left( \sum_{p=1}^m \eta_p^2 \right)^2 + d \sum_{p=1}^m |\eta_p|^n \right) dV; \quad (5.8)$$

$$1 < n \ll 2,$$

where  $\Delta G$  is the chemical driving force and is the difference in the specific  $F_{ch}$  between the parent and the product. The following equation can be used to calculate  $\Delta G$  for 3Y-STZ at different temperatures [16, 123]:

$$\Delta G(T \rightarrow M) = -6159.18 + 6.98T, \quad (5.9)$$

where the energy is in  $\text{Jmol}^{-1}$  (or  $\text{Jm}^{-3}$ ) and the temperature (T) is in Kelvin (K). In addition,  $a$ ,  $b$ ,  $c$ ,  $d$ , and  $n$  are coefficients that should be chosen in a way that maintains the value of the interfacial energy within the physical reasonable range [53] and at  $\eta_p = 1$  result in  $F_{ch} = \Delta G(T \rightarrow M)$ .

- *Gradient free energy ( $F_{gd}$ ):*

$F_{gd}$  represents the interfacial energy between tetragonal-monoclinic or monoclinic-monoclinic phases and ensures a smooth transition of the OPs between different phases. It is expressed as:

$$F_{\text{gd}}(\eta_1, \eta_2, \dots, \eta_m) = \int_V \frac{B_{ij}}{2} \sum_{p=1}^m \nabla_i \eta_p \nabla_j \eta_p dV, \quad (5.10)$$

where  $\nabla$  is the gradient operator and  $B_{ij}$  is gradient energy tensor. We assume that the gradient energy coefficient is isotropic ( $B_{ij} = B\delta_{ij}$ ) [16]. Therefore the Eq. (5.10) becomes:

$$F_{\text{gd}}(\eta_1, \eta_2, \dots, \eta_m) = \int_V \frac{B}{2} \sum_{p=1}^m (\nabla \eta_p)^2 dV. \quad (5.11)$$

- *Fracture energy ( $F_{\text{fr}}$ ):*

$F_{\text{fr}}$  presents the fracture energy in the system and is defined as [65, 74, 80]:

$$F_{\text{fr}}(\phi) = \int_V G_c \left( \frac{\phi^2}{2k} + \frac{k}{2} |\nabla \phi|^2 \right) dV, \quad (5.12)$$

where  $G_c$  is the fracture surface energy in Griffith's theory, and  $k$  is a positive regularization parameter with the dimension of length to regulate the width of the crack phase field. In this paper, we use the method proposed by Miehe et al. [81] to ensure irreversibility of crack (crack healing prevention):

$$F_{\text{el}}(u_i, t) = \max_{s \in [0, t]} F_{\text{el}}(u_i, s). \quad (5.13)$$

## 5.4 Governing equations

The evolution of both MPT and PF fracture are obtained by Ginzburg-Landau equation [124]. This equation relates the rate of each OP to the variational derivative of total free energy with respect to the same OP. Using Ginzburg-Landau equation for MPT yields following equation:

$$\frac{\partial \eta_p}{\partial t} = L \left( \frac{\delta F_{\text{tot}}}{\delta \eta_p} \right) = L \left( \frac{\delta F_{\text{el}}}{\delta \eta_p} + \frac{\delta F_{\text{ch}}}{\delta \eta_p} + \frac{\delta F_{\text{gd}}}{\delta \eta_p} + \frac{\delta F_{\text{fr}}}{\delta \eta_p} \right), \quad (5.14)$$

where  $L$  is the kinetic coefficient, and:

$$\begin{aligned} \frac{\delta F_{\text{el}}}{\delta \eta_p} &= \frac{1}{2} g(\phi) \varepsilon_{ij}^{\text{el}} (C_{ijkl}^{\text{M}} - C_{ijkl}^{\text{T}}) \varepsilon_{kl}^{\text{el}} - \frac{1}{2} g(\phi) C_{ijkl}(\eta_1, \eta_2, \dots, \eta_m) \varepsilon_{kl}^{\text{00}}(p) \varepsilon_{ij}^{\text{el}} \\ &\quad - \frac{1}{2} g(\phi) C_{ijkl}(\eta_1, \eta_2, \dots, \eta_m) \varepsilon_{ij}^{\text{00}}(p) \varepsilon_{kl}^{\text{el}}, \end{aligned} \quad (5.15)$$

$$\frac{\delta F_{\text{ch}}}{\delta \eta_p} = \Delta G (2a\eta_p - 3b\eta_p^2 + 4c\eta_p \sum_{p=1}^m \eta_p^2), \quad (5.16)$$

$$\frac{\delta F_{\text{gd}}}{\delta \eta_p} = -B \nabla^2 \eta_p, \quad (5.17)$$

$$\frac{\delta F_{\text{fr}}}{\delta \eta_p} = 0. \quad (5.18)$$

In addition, using the Ginzburg-Landau equation for PF fracture leads to:

$$\frac{\partial \phi}{\partial t} = M \left( \frac{\delta F_{\text{tot}}}{\delta \phi} \right) = M \left( \frac{\delta F_{\text{el}}}{\delta \phi} + \frac{\delta F_{\text{ch}}}{\delta \phi} + \frac{\delta F_{\text{gd}}}{\delta \phi} + \frac{\delta F_{\text{fr}}}{\delta \phi} \right), \quad (5.19)$$

where  $M$  is called the fracture mobility coefficient, and:

$$\frac{\delta F_{\text{el}}}{\delta \phi} = -(1 - \phi) C_{ijkl}(\eta_1, \eta_2, \dots, \eta_m) \varepsilon_{kl}^{\text{el}} \varepsilon_{ij}^{\text{el}}, \quad (5.20)$$

$$\frac{\delta F_{\text{ch}}}{\delta \phi} = 0, \quad (5.21)$$

$$\frac{\delta F_{\text{gd}}}{\delta \phi} = 0, \quad (5.22)$$

$$\frac{\delta F_{\text{fr}}}{\delta \phi} = G_c \left( \frac{\phi}{k} - k \nabla^2 \phi \right). \quad (5.23)$$

In addition, by neglecting the body forces, the equilibrium equations become:

$$\text{div } \boldsymbol{\sigma}(u_i, \phi) = 0. \quad (5.24)$$

## 5.5 Crystal viscoplasticity

Experimental observations well established plastic slip as the predominant irreversible mechanism in single crystal zirconia-based SMCs [8]. To incorporate slip in our formulation, we employ crystal viscoplasticity. Slip systems are defined by two vectors: normal vector of the slip

plane ( $\vec{p}$ ) and the slip direction vector ( $\vec{d}$ ). Plastic strain tensor of the  $n$ th slip systems is expressed as [175]:

$$\varepsilon_{ij}^{\text{pl}} = \sum_{n=1}^N \dot{\gamma}_n P_{nij} \quad (5.25)$$

where  $N$  is the total number of slip systems,  $\dot{\gamma}_n$  is the plastic slip evolution rate, and  $P_{ij}$  are the components of the orientation tensor ( $\mathbf{P}_n$ ), also known as symmetrized Schmid tensor, of the  $n$ th slip system and is calculated as:

$$\mathbf{P}_n = \frac{1}{2} (\vec{p}_n \otimes \vec{d}_n + \vec{d}_n \otimes \vec{p}_n) \quad (5.26)$$

In addition, the accumulated plastic slip and the magnitude of plastic slip at time  $t$  are defined as follows [175]:

$$\dot{\gamma} = \sum_{n=1}^N |\dot{\gamma}_n| \quad (5.27)$$

$$|\gamma| = \int_0^t \dot{\gamma} dt \quad (5.28)$$

The slip systems become active when the resolved shear stress on the slip plane and in the slip direction reaches a critical or yield stress threshold ( $\tau_{cr}$ ). The resolved shear stress in the slip direction, a scalar quantity, is computed as follows:

$$\tau_n = \boldsymbol{\sigma}(u_i, \phi) \cdot \mathbf{P}_n \quad (5.29)$$

There are various flow rules to calculate the  $\dot{\gamma}_n$ . In this study, we adopt a Chaboche-type potential defined as follows [175]:

$$\dot{\gamma}_n = \vartheta \operatorname{sgn}(\tau_n) \left\langle \frac{|\tau_n| - \tau_{crn}}{\tau_{Dn}} \right\rangle_+^{m_n} \quad (5.30)$$

where  $\vartheta$  is viscosity coefficient,  $m$  and  $\tau_D$  are model constants, and the Macaulay brackets is defined as  $\langle * \rangle_+ = \max(0, *)$ .  $\tau_{crn}$  is a function of  $|\gamma|$  and is defined to take the following form:

$$\begin{cases} \tau_{crn} = \sigma_{yo_n} + H_n |\gamma|^{\xi_n} & \text{if } \tau_{crn} > \sigma_{yo_{minn}} \\ \tau_{crn} = \sigma_{yo_{minn}} & \text{if } \tau_{crn} \leq \sigma_{yo_{minn}} \end{cases} \quad (5.31)$$

where  $\sigma_{yo_n}$  is the initial yield,  $H_n$  is the hardening modulus, and  $\sigma_{yo_{minn}}$  is the lowest yield stress, respectively, of  $n$ th slip system.

## 5.6 Solution Scheme, boundary conditions, model and material constants:

The governing equations presented in the previous section are solved in a finite element framework using the solid mechanics and mathematics modulus of COMSOL Multiphysics. All simulations are under load-controlled loading conditions unless otherwise stated. The boundary conditions and sample dimensions are shown in Figure 5.1. For all models, quadrilateral 3D elements are generated by the swept mesh algorithm feature in COMSOL. A mesh study was conducted where we found that a mesh size of 0.07  $\mu\text{m}$  (or 18200 quadrilateral elements in the domain) were sufficient to resolve the interface of different phases and PF fracture profile. The displacements are solved using ‘‘Solid Mechanics’’ module with linear shape functions. The crack PF and Martensite PF are solved using the ‘‘General Form PDE’’ module of COMSOL with linear shape functions. In addition, the crystal plasticity strains are calculated using the ‘‘domain ODEs’’ module with linear shape functions. The staggered scheme [126] is used to solve the governing equations where nonlinear problems are solved with Newton’s method. The time step of 0.05s is used for all simulations.

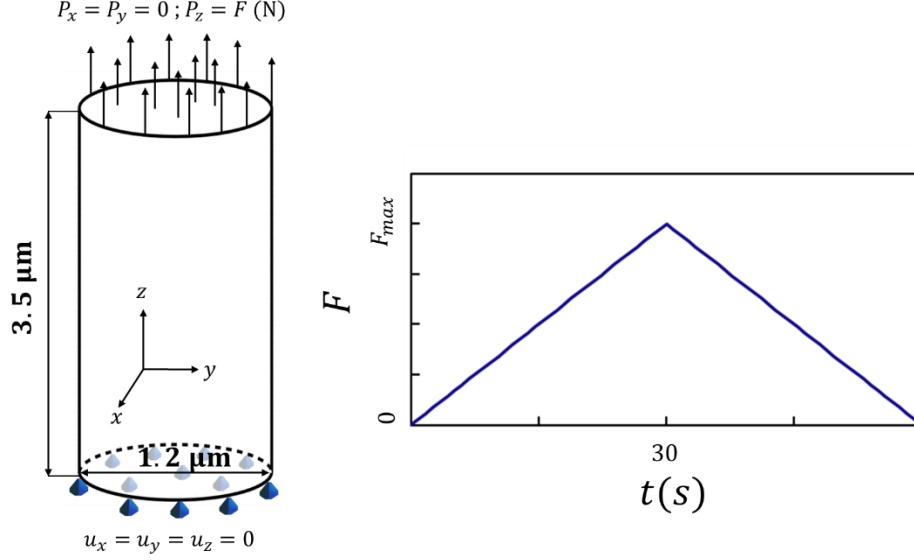


Figure 5.1 Micropillar dimensions and boundary conditions.

## 5.7 Material properties and model parameters

3Y-STZ, which is a SMC [138, 168], is the material of study in this work. The equilibrium temperature of 3Y-STZ is reported to be  $\sim 883$  K [16]. We consider the temperature of the system is constant and equal to 820 K and we use this temperature to calculate  $\Delta G$  in Eq. (5.9) which yields  $\Delta G = -433 \text{ Jmol}^{-1}$  ( $-20 \times 10^6 \text{ Jm}^{-3}$ ). It is worth noting that the considered temperature is lower than the equilibrium temperature, therefore, the system is in SME regime (strain recovery does not occur after unloading). Eq. (5.32) and Eq. (5.33) show the stiffness tensor of tetragonal and monoclinic phases, respectively [130, 169]. In addition, 3Y-STZ has 12 different M variants, and the stress-free strain tensor of each variant is expressed in Eq. (5.34) [24].

$$C_{ijkl}^T = \begin{bmatrix} 361 & 100 & 62 & 0 & 0 & 0 \\ 100 & 361 & 62 & 0 & 0 & 0 \\ 62 & 62 & 264 & 0 & 0 & 0 \\ 0 & 0 & 0 & 59 & 0 & 0 \\ 0 & 0 & 0 & 0 & 59 & 0 \\ 0 & 0 & 0 & 0 & 0 & 64 \end{bmatrix} \text{GPa}, \quad (5.32)$$

$$\mathbf{C}_{ijkl}^M = \begin{bmatrix} 327 & 142 & 55 & 0 & 0 & -21 \\ 142 & 408 & 196 & 0 & 0 & 31 \\ 55 & 196 & 258 & 0 & 0 & -18 \\ 0 & 0 & 0 & 100 & -23 & 0 \\ 0 & 0 & 0 & -23 & 81 & 0 \\ -21 & 31 & -18 & 0 & 0 & 126 \end{bmatrix} \text{GPa}, \quad (5.33)$$

$$\begin{aligned} \varepsilon_{ij}^{00}(1) &= \begin{bmatrix} 0.0418 & -0.0769 & 0 \\ -0.0769 & 0.0048 & 0 \\ 0 & 0 & -0.0114 \end{bmatrix} & \varepsilon_{ij}^{00}(2) &= \begin{bmatrix} 0.0418 & 0.0769 & 0 \\ 0.0769 & 0.0048 & 0 \\ 0 & 0 & -0.0114 \end{bmatrix} \\ \varepsilon_{ij}^{00}(3) &= \begin{bmatrix} 0.0049 & 0 & -0.0769 \\ 0 & 0.0117 & 0 \\ -0.0769 & 0 & 0.0180 \end{bmatrix} & \varepsilon_{ij}^{00}(4) &= \begin{bmatrix} 0.0049 & 0 & 0.0769 \\ 0 & 0.0117 & 0 \\ 0.0769 & 0 & 0.0180 \end{bmatrix} \\ \varepsilon_{ij}^{00}(5) &= \begin{bmatrix} 0.0117 & 0 & 0 \\ 0 & 0.0049 & -0.0760 \\ 0 & -0.0760 & 0.0180 \end{bmatrix} & \varepsilon_{ij}^{00}(6) &= \begin{bmatrix} 0.0117 & 0 & 0 \\ 0 & 0.0049 & 0.0760 \\ 0 & 0.0760 & 0.0180 \end{bmatrix} \\ \varepsilon_{ij}^{00}(7) &= \begin{bmatrix} 0.0048 & -0.0769 & 0 \\ -0.0769 & 0.0418 & 0 \\ 0 & 0 & -0.0114 \end{bmatrix} & \varepsilon_{ij}^{00}(8) &= \begin{bmatrix} 0.0048 & 0.0769 & 0 \\ 0.0769 & 0.0418 & 0 \\ 0 & 0 & -0.0114 \end{bmatrix} \\ \varepsilon_{ij}^{00}(9) &= \begin{bmatrix} 0.0117 & 0 & 0 \\ 0 & 0.0419 & -0.0760 \\ 0 & -0.0760 & -0.0180 \end{bmatrix} & \varepsilon_{ij}^{00}(10) &= \begin{bmatrix} 0.0117 & 0 & 0 \\ 0 & 0.0419 & -0.0760 \\ 0 & -0.0760 & -0.0180 \end{bmatrix} \\ \varepsilon_{ij}^{00}(11) &= \begin{bmatrix} 0.0419 & 0 & -0.0769 \\ 0 & 0.0117 & 0 \\ -0.0769 & 0 & -0.0181 \end{bmatrix} & \varepsilon_{ij}^{00}(12) &= \begin{bmatrix} 0.0419 & 0 & 0.0769 \\ 0 & 0.0117 & 0 \\ 0.0769 & 0 & -0.0181 \end{bmatrix} \end{aligned} \quad (5.34)$$

Table 5.1 shows the other model parameters used in the simulations.

Table 5.1 Model parameters

Parameters	Values
$a, b, c, d,$ and $n$	2.15, 11.95, 7.5, 1.25, and 1.1
$\sigma_{y0_n}, \sigma_{y0_{min_n}}, H_n, \xi_n, \tau_{D_n},$ and $m_n$	0.550 GPa, 0.275 GPa, -150 GPa, 1, 1, and 1
$B$	$1 \times 10^{-6} \text{ Jm}^{-1}$
$L$	$1 \times 10^{-9} \text{ Pa}^{-1}\text{s}^{-1}$ [53]
$\vartheta$	$1 \times 10^4 \text{ Pa}^{-1}\text{s}^{-1}$
$G_c, k$	200 $\text{Nm}^{-1}$ [13], 0.15 $\mu\text{m}$

$a, b, c, d,$  and  $n$  are calculated in a way that the  $F_{ch}$  plot is a double-well [16] and the value of  $F_{ch}$  is equal to  $-20 \times 10^6 \text{ Jm}^{-3}$  at  $\eta_p = 1$ . Plastic slip, similar to MPT, forms localized small bands. Incorporating stress softening into the yield stress is crucial for accurately modeling this phenomenon, which necessitates selecting a negative value for the hardening coefficient  $H$  [176]. The chosen value is notably large and negative, a decision informed by molecular dynamics (MD) findings that report a sharp decline in the stress-strain curve upon slip initiation [177]. In addition, it's important to note that the yield stress never reaches zero or becomes negative, after slip initiation. Consequently, we must establish a minimum yield stress ( $\sigma_{yomin_n}$ ) to account for this behavior. Based on the observed trend in MD simulations, we set  $\sigma_{yomin_n}$  to be 50% of the initial slip yield stress [177]. Also, the approach to find  $\sigma_{y0_n}$  value, is discussed in section 5.9 . We chose  $B = 1 \times 10^{-6} \frac{\text{J}}{\text{m}}$  and based on our results gives a reasonable interface thickness between different phases and choosing smaller value did not affect the results noticeably. It is worth mentioning, we considered the family of  $\{110\}\langle 110\rangle$  as the slip systems of the tetragonal phase [139] . This system encompasses four distinct slip systems, therefore  $N$  is Eq. (5.25) is 4. In addition, the Euler angles of the studied micropillars are given in table 5.2. It is important to highlight that orientation of (100) indicates alignment of the a-axis, b-axis, and c-axis of the tetragonal phase with the z-axis, y-axis, and x-axis respectively of the global coordinate system (Figure 5.1), while an orientation of (001) denotes alignment of the a-axis, b-axis, and c-axis of the tetragonal phase with the x-axis, y-axis, and z-axis respectively of the global coordinate system.

Table 5.2 Pillars ID and orientations

Pillar ID	Euler Angles (in degrees)		
	E1	E2	E3
p1	0	0	0
p2	190	45	230
p3	285	45	320
p5	300	60	350
p6	30	75	340
p7	0	90	45
p8	0	90	0
p9	68	104	305
p10	245	35	200
p11	265	63	16

## 5.8 Results and Discussion:

We investigated 11 grain orientations, as detailed in Table 5.2. To visually represent our findings, we constructed a pole figure with three vertices corresponding to orientations of (100), (110), and (001) as shown in Figure 5.2. To differentiate between MPT, slipping, and cracking, we followed a systematic approach. Initially, a load ranging between 1.5mN to 2mN was applied, and simulations were run for one cycle. If MPT occurred, we classified the pillar as a transforming pillar. In cases where MPT did not occur, we increased the load to approximately 3mN and observed the results after one cycle. If slipping was observed, we designated the pillar as having undergone plastic slip. If plastic slip was not observed, we further increased the load to approximately 5mN or higher until cracking was observed. This step-by-step process allowed us to categorize the behavior of each pillar accurately.

Figure 5.2 illustrates that a broad range of tested pillars exhibits full MPT. However, pillar p8 displays fracture with minimal MPT and slipping. In pillar p1, a combination of fracture

and MPT is observed with a minor plastic slip. In this pillar, MPT initiates at a high load, explaining the extended plateau before complete fracture development.

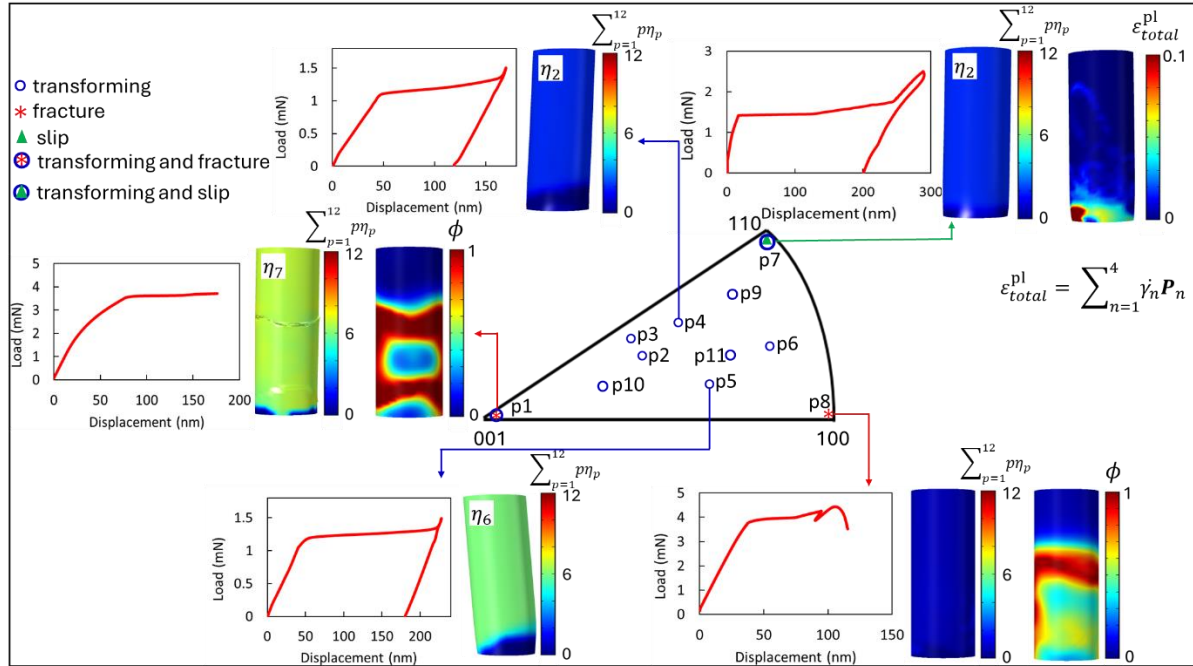


Figure 5.2 Pole figure presenting the effects of grain orientation on the interplay between MPT, cracking, and slip in micropillars.

Furthermore, pillar p7 demonstrates both MPT and a considerable amount of plastic slip. Our findings highlight that the slip systems characterized by  $p = \langle 110 \rangle$  and  $d = \langle 110 \rangle$  and  $p = \langle 1\bar{1}0 \rangle$  and  $d = \langle 110 \rangle$  exhibit the highest accumulation of plastic slip among all four slip systems considered. The plastic slip is particularly pronounced at the bottom edge of the pillar. This can be attributed to the fully fixed boundary conditions, which induce high stress concentrations, consequently leading to significant plastic deformation. However, it's worth noting that plastic slip also occurs within the middle section of the pillar, as depicted in Figure 5.2. It is worth noting that in an experimental report, pillars with similar grain orientations have been observed to exhibit only plastic slip without MPT [8].

The pole figure presented in Figure 5.2, agrees well with a similar experimental test conducted on zirconia-based SMCs [8]. The discrepancy in MPT start load and residual displacement between p7 in this study and the experimental data could be due to high variations in the mechanical properties of the materials under examination. While we utilized properties of 3-YSZ, the material in [8] the material was different and was  $2Y_2O_3-5TiO_2-ZrO_2$  (mol%).

In addition, similar to experimental observations [8], our simulations revealed that in pillars exhibiting MPT, only one  $M$  variant out of the 12 possible variants develops; specifically, variant 2 ( $\eta_2$ ) and variant 6 ( $\eta_6$ ), with a predominant occurrence of  $\eta_2$ . This observation can be explained based on the deformation conditions described by  $\varepsilon_{ij}^{00}$  (2). A deformation exerting contraction along the c-axis and expansion along the a-axis and b-axis of the tetragonal crystal structure favors the formation of  $\eta_2$ . This deformation pattern aligns with the effects induced by a compressive load applied along the z-axis. However, the formation of an  $M$  variant depends on different factors such as grain orientation, loading direction, and boundary conditions, making it a complex and unpredictable phenomenon.

Figure 5.3 depicts the load-displacement plots of selected pillars with full MPT. From this figure, it can be deduced that grain orientation significantly impacts the elastic modulus in both loading and unloading paths, the critical stress for MPT initiation, and the duration of the plateau. Based on Figure 5.3, the critical MPT load (MPT start load) ranges from 0.9 mN (790 MPa) to 1.3 mN (1150 MPa). In addition, the residual displacement is also highly dependent on the grain orientation and ranges from 105 nm (3% strain) to 190 nm (5.4% strain).

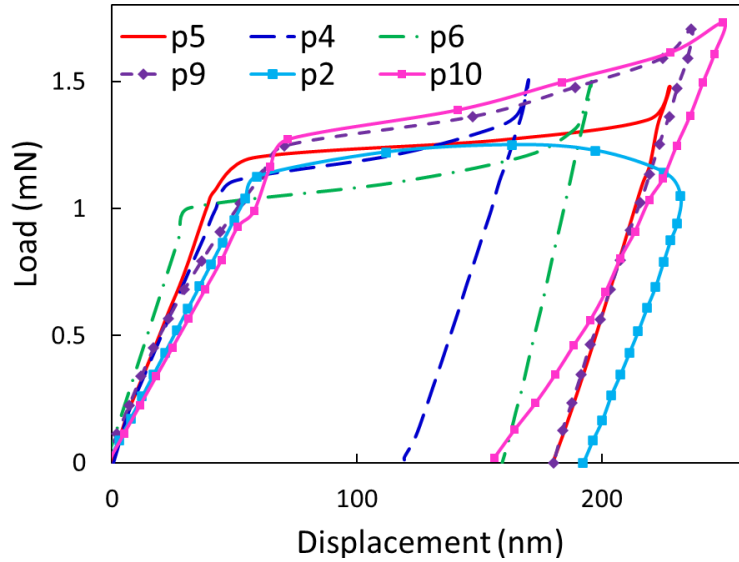


Figure 5.3 Load-displacement curve for selected pillar with full MPT.

It is important to note that simulations featuring fracture do not exhibit a final drop and diverge once the crack is fully developed, due to applied force-controlled loading. To observe the ultimate strength and achieve a final drop in the stress-strain curve, a displacement-controlled loading must be applied [53]. To obtain a final drop and establish an ultimate strength, displacement-controlled loading was applied to pillar p1, and the outcomes are presented in Figure 5.4.

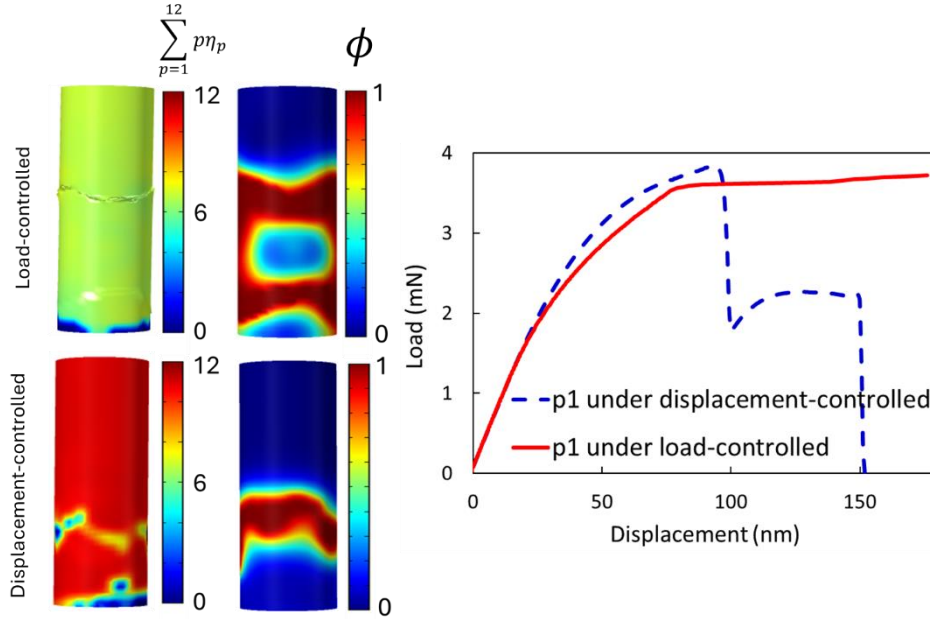


Figure 5.4 The crack path, MPT, and mechanical response of p1 under load-controlled and displacement-controlled loading conditions.

In this figure after the final drop in load, another plateau is observed. This is due to the MPT occurrence after crack initiates. This observation explains transformation toughening. In other words, when crack initiates, since stress becomes very high in front of the crack tip(s), MPT triggers and becomes a source of energy dissipation in addition to cracking. The energy dissipation due to MPT slows down the crack propagation. This phenomenon reflects as a plateau or strain hardening in the load-displacement plot. This result is consistent with MD observations on single crystal 3-YSZ [177]. Furthermore, the distinction in the nature of these two boundary conditions leads to differences in the crack path observed. While load-controlled simulations exhibit the occurrence of  $\eta_7$  in displacement-controlled conditions,  $\eta_{11}$  emerges as the only  $M$  phase. This observation can be explained by recognizing that cracks significantly affect the stress distribution within the domain, ultimately affecting the occurrence of different  $M$  phases. Therefore, variations in stress distribution resulting from different crack paths can lead to the occurrence of different  $M$  phases in the material.

## 5.9 Identification of $\sigma_{y0_n}$ in the crystal viscoplasticity model

In the slip system of  $\{110\}\langle 110\rangle$ , with consideration for the direction of the applied external load, the grain orientation of (110) (or Euler angles of  $(0^\circ, 90^\circ, 45^\circ)$ ) yields the highest resolved shear, as the slip directions closely align with the loading direction. To determine the critical resolved shear stress ( $\sigma_{y0_n}$ ), we first selected the average plastic yield stress to be 3000 MPa [16]. To generate this average stress, a load of 3.4 mN considering the micropillar's radius of  $1.2\mu\text{m}$ . We applied 3.5 mN to p7 and systematically decreased values for  $\sigma_{y0_n}$  starting from 3000 MPa until a slip band was observed. Throughout this process, the objective is to identify the maximum values of  $\sigma_{y0_n}$  that induce plastic slip, therefore the MPT function is turned off. The critical value of  $\sigma_{y0_n}$  is determined to be around 550 MPa. Figure 5.5 depicts the slip band and the load-displacement curve obtained during the identification of  $\sigma_{y0_n}$ . This figure shows that plastic slip localizes to a small band similar to experimental observations. Furthermore, once slip band forms, the viscosity coefficient ( $\vartheta$ ) influences the deformation and residual displacement. In Figure 5.5, the residual displacement falls within a reasonable and acceptable range, indicating that the value selected for  $\vartheta$  is suitable.

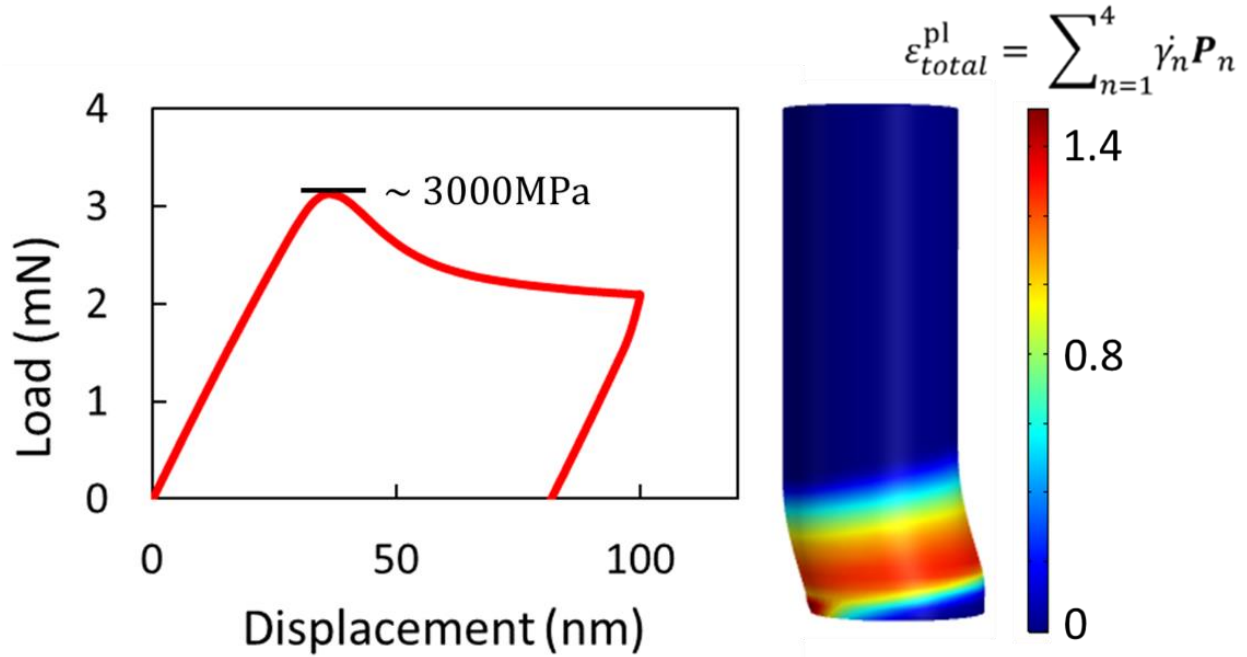


Figure 5.5 Slip band formation and load-displacement curve of p1 with  $\sigma_{y0_n} = 550$  MPa and with MPT turned off.

### 5.10 Conclusions:

We present a numerical framework combining PF fracture, PF-MPT, and crystal viscoplasticity to investigate the effects of grain orientation on the interplay of mechanisms of MPT, fracture, and plastic slip in SME SMCs under compressive loading conditions.

Our findings reveal that single crystal 3-YSZ micropillars exhibit complete MPT for a wide range of crystal orientations without experiencing irreversible mechanisms of fracture or plastic slip. We observed that the initiation load for MPT ranges between 0.9 mN (790 MPa) to 1.3 mN (1150 MPa) which is in good agreement with experimental data. Moreover, when the pillar's a-axis aligns with the loading direction (global z-axis) and its b and c axes align with the y and x directions, respectively, fracture emerges as the predominant mechanism, with both MPT and slip occurring minimally.

When examining the pillar with the (001) orientation, we observe a combination of both MPT and fracture mechanisms. In the simulation performed under displacement-controlled loading condition, we observed that fracture initiates first in this pillar, followed by the occurrence of MPT. The MPT induces a transformation toughening effect before the pillar experiences complete cracking. Such complex phenomena are challenging, if not impossible, to fully capture through experimental means alone. Additionally, this outcome shows the necessity of employing displacement-controlled loading for simulating fracture and capturing the complete process of crack propagation and establishing the ultimate strength of materials. Unlike load-controlled loading, displacement-controlled loading enables a more comprehensive understanding of fracture mechanisms and facilitates the observation of the entire crack propagation process.

For pillars oriented along the (110) direction, we observe a combination of MPT and significant plastic slip. Our model predicts that plastic slip accumulates predominantly on the slip systems with a normal vector  $p = \langle 110 \rangle$  and along  $d = \langle 110 \rangle$  and  $p = \langle 1\bar{1}0 \rangle$  and along  $d = \langle 110 \rangle$ . While other slip systems may also be activated, the amount of plastic slip observed is minimal.

The results of this investigation demonstrate the efficiency, predictiveness, and accuracy exhibited by the proposed numerical framework. Our results illustrate that the proposed numerical approach yields predictions in excellent agreement with experimental findings. Moreover, it enables the capture of phenomena that are challenging, if not impossible, to observe solely through experimental studies.

## CHAPTER 6

### CONCLUSIONS AND RECOMMENDATIONS FOR FUTURE WORK

#### **6.1 Conclusions**

SMCs, characterized by their ability to recover their original shape upon the application of heat or mechanical load, have gained significant attention across different engineering fields. These remarkable materials find application across a wide array of industries, including aerospace, healthcare, automotive, and consumer electronics. However, their practical applications have been hindered by challenges like low fracture toughness and limited fatigue life.

Studying fracture properties and fatigue behavior is a critical step in designing engineering structures composed of engineering materials, such as SMCs. Computational studies provide a means to investigate the intricate interactions between MPT, cracking, as well as plastic deformation; interactions that are challenging or impossible to investigate by experimental studies alone. In this Ph.D. research, we introduced a modified PF fracture model capable of accurately predicting crack paths and mechanical responses in brittle polycrystalline materials. Additionally, we proposed two distinct computational frameworks designed for precise prediction of crack propagation and cyclic responses in SMCs.

First, we explained that the ultimate stress predicted by the original PF fracture model does not include the material strength and is dependent on materials elastic modulus, critical energy release rate and the PF lengths scale parameter. We demonstrated that the original model yields unrealistic ultimate stress in microscopic domains, primarily due to the small length scale parameter. To address this limitation, we proposed a modification to the original PF formulation, which incorporates the material's strength. Furthermore, we integrated our modified model with

a PF fracture model that accounts for the effects of cleavage planes. Our results indicate that in  $ZrB_2$ , both transgranular and intergranular cracking are observed, with a higher inclination towards transgranular cracking. In addition, the proposed models effectively consider both material strength and cleavage planes, resulting in realistic mechanical responses and accurate predictions of crack paths in brittle polycrystalline materials.

Furthermore, we identified that the previous PF-MPT models underestimate the elastic modulus in the initial stage of stress-strain curve, leading to inaccuracies in mechanical response predictions. We addressed this issue by modifying the commonly used 2-3-4 chemical free energy formulation. This modification involved the addition of an extra term to the chemical free energy while maintaining its requisite characteristics. We demonstrated that our modified model is capable of predicting all stages of stress-strain curve accurately. We coupled the modified model with a PF fracture model to investigate the effects of grain orientation on the interactive evolution of MPT and cracking in SMCs operating in the SE regime under displacement-controlled loading conditions. Our results indicate that the model captures the effects of grain orientation accurately and predicts reverse MPT behind the crack tip. The results reveal that a slight change in the grain orientation exerts a significant impact on the MPT and crack path. Moreover, the MPT not only affects the crack path but also induces transformation toughening and crack deflection. Furthermore, the model yields a realistic stress-strain curve that exhibits all the features of a propagated cracked SMC, including a final drop in the stress-strain curve as well as a stress plateau due to MPT before crack propagation.

Additionally, we integrated our modified PF-MPT formulation with a straightforward viscoplasticity model to examine how microstructural features impact the cyclic response of polycrystalline SMCs. We utilized the PSA as a representative of cyclic life prior to fatigue crack

initiation. We explored various strategies aimed at mitigating PSAs to potentially enhance the cyclic life of these ceramics. Our investigation revealed that the adjustment of the microstructure can significantly reduce PSA, potentially leading to an extended cyclic life before fatigue crack initiation. We Employed cross-correlation data analysis to delineate the key microstructural features in controlling PSA under cyclic loading conditions. This research reveals that by creating textures with specific grain orientation relative to the loading direction, the cyclic life of these ceramics can be significantly extended by mitigating PSA. In addition, pores can also increase the cyclic life noticeably if placed at GBs.

Finally, we developed a comprehensive predictive 3D PF based numerical framework incorporating PF fracture, PF-MPT, and crystal viscoplasticity. We examined the effects of grain orientation on the interplay between MPT, fracture, and plastic slip in single crystal 3D micropillars. To visualize our findings, we generated a pole figure illustrating the dominant regions for each mechanism. Through a thorough comparison with experimental data, the model demonstrates its capability of predicting similar trends observed by experiment; however, there are some differences primarily stem from variations in material properties used in our model compared to those of the material used in the experimental setting. We found that grain orientation in single crystal micropillars has a large impact on activation of different mechanics of fracture, MPT, or slip or a combination of these mechanisms. In addition, we identify a large range of grain orientation resulting in full MPT. This study highlights the accuracy of a reliable numerical framework in predicting experimental observations, suggesting its potential as an alternative to experimental studies. A reliable numerical model not only does capture the experimental observations accurately, but it also demonstrates the capability to capture phenomena that are challenging or even impossible to investigate by experiments.

## 6.2 Recommendations for Future Work

The PF fracture model employed in this research is suitable for brittle materials. While the investigations outlined in this research are transferable to shape memory alloys like NiTi, a transition to NiTi necessitates the adoption of a ductile PF model. Unlike the PF brittle fracture model, a fracture model for ductile materials must include various factors such as triaxiality, lude angle effects, and void coherence to accurately capture the behavior of ductile materials like NiTi.

Furthermore, determining the appropriate yield surface for calculating the onset of MPT in large samples of shape memory materials, which predominantly exhibit isotropic behavior, poses a significant challenge. Unlike the simpler yield surfaces such as Mohr-Coulomb or Mises used in non-transforming materials, the yield surface in these materials is more complex and has unusual shape. To address this challenge, numerical studies can offer a viable solution. Initially, the PF polycrystal model employed in this study can generate polycrystals comprising a significant number of crystals, effectively representing nearly isotropic behavior. Subsequently, the modified PF-MPT model proposed in this research can be applied to determine the initiation of MPT under various loading conditions. By repeating this process, multiple points can be identified and plotted against applied stresses, resulting in a representation of the material's yield surface. Employing this methodology, only a few experiments are required to validate or refine the obtained plot, leading to substantial savings in both expense and time.

The accuracy of the PF fracture model is highly dependent on the resolution of the crack profile which is exponential. The accurate resolution of this profile necessitates a refined mesh, particularly within the fracture process zone, making the PF fracture model computationally expensive. To address this issue, a meshing algorithm can be developed to generate refined mesh

in front of the crack tip within the process zone while generating a coarser mesh behind the crack tip. By implementing such an algorithm, the efficiency of the PF fracture model can be significantly enhanced, thus facilitating its application in larger-scale 3D simulations.

## REFERENCES

- [1] K. Otsuka and C. M. Wayman, *Shape memory materials*. Cambridge university press, 1999.
- [2] Z. Du, H. Yu, C. A. Schuh, and C. L. Gan, "Shape memory ceramic particles and structures formed thereof," ed: Google Patents, 2020.
- [3] Z. Y. Hang, M. Hassani-Gangaraj, Z. Du, C. L. Gan, and C. A. Schuh, "Granular shape memory ceramic packings," *Acta Materialia*, vol. 132, pp. 455-466, 2017.
- [4] P. M. Kelly and L. F. Rose, "The martensitic transformation in ceramics—its role in transformation toughening," *Progress in Materials Science*, vol. 47, no. 5, pp. 463-557, 2002.
- [5] A. Lai, Z. Du, C. L. Gan, and C. A. Schuh, "Shape memory and superelastic ceramics at small scales," *Science*, vol. 341, no. 6153, pp. 1505-1508, 2013.
- [6] Z. Du, X. M. Zeng, Q. Liu, C. A. Schuh, and C. L. Gan, "Superelasticity in micro-scale shape memory ceramic particles," *Acta Materialia*, vol. 123, pp. 255-263, 2017.
- [7] Z. Du *et al.*, "Size effects and shape memory properties in ZrO<sub>2</sub> ceramic micro- and nano-pillars," *Scripta Materialia*, vol. 101, pp. 40-43, 2015.
- [8] X. M. Zeng, A. Lai, C. L. Gan, and C. A. Schuh, "Crystal orientation dependence of the stress-induced martensitic transformation in zirconia-based shape memory ceramics," *Acta Materialia*, vol. 116, pp. 124-135, 2016/09/01/ 2016, doi: <https://doi.org/10.1016/j.actamat.2016.06.030>.
- [9] D. Casellas, J. Alcalá, L. Llanes, and M. Anglada, "Fracture variability and R-curve behavior in yttria-stabilized zirconia ceramics," *Journal of materials science*, vol. 36, no. 12, pp. 3011-3025, 2001.
- [10] S. Y. Liu and I. W. Chen, "Fatigue of Yttria-Stabilized Zirconia: II, Crack Propagation, Fatigue Striations, and Short-Crack Behavior," *Journal of the American Ceramic Society*, vol. 74, no. 6, pp. 1206-1216, 1991.
- [11] A. G. Evans and R. Cannon, "Toughening of brittle solids by martensitic transformations," *Acta Metall.:(United States)*, vol. 34, no. 5, 1986.
- [12] S. Deville, H. El Attaoui, and J. Chevalier, "Atomic force microscopy of transformation toughening in ceria-stabilized zirconia," *Journal of the European Ceramic Society*, vol. 25, no. 13, pp. 3089-3096, 2005.
- [13] R. H. Hannink, P. M. Kelly, and B. C. Muddle, "Transformation toughening in zirconia-containing ceramics," *Journal of the American Ceramic Society*, vol. 83, no. 3, pp. 461-487, 2000.
- [14] M. Mamivand, M. Asle Zaeem, H. El Kadiri, and L.-Q. Chen, "Phase field modeling of the tetragonal-to-monoclinic phase transformation in zirconia," *Acta Materialia*, vol. 61, no. 14, pp. 5223-5235, 2013.
- [15] M. Mamivand, M. Asle Zaeem, and H. El Kadiri, "Shape memory effect and pseudoelasticity behavior in tetragonal zirconia polycrystals: A phase field study,"

- International Journal of Plasticity*, vol. 60, pp. 71-86, 2014/09/01/ 2014, doi: <https://doi.org/10.1016/j.ijplas.2014.03.018>.
- [16] C. Cissé and M. Asle Zaeem, "A phase-field model for non-isothermal phase transformation and plasticity in polycrystalline yttria-stabilized tetragonal zirconia," *Acta Materialia*, vol. 191, pp. 111-123, 2020/06/01/ 2020, doi: <https://doi.org/10.1016/j.actamat.2020.03.025>.
- [17] C. Cissé and M. Asle Zaeem, "A phase-field model for non-isothermal phase transformation and plasticity in polycrystalline yttria-stabilized tetragonal zirconia," *Acta Materialia*, vol. 191, pp. 111-123, 2020.
- [18] C. Cissé and M. Asle Zaeem, "Defect-induced asymmetrical mechanical behavior in shape memory zirconia: A phase-field investigation," *Journal of the European Ceramic Society*, vol. 42, no. 10, pp. 4296-4310, 2022.
- [19] J. Zhu, J. Luo, and Y. Sun, "Phase field study of the grain size and temperature dependent mechanical responses of tetragonal zirconia polycrystals: A discussion of tension-compression asymmetry," *Computational Materials Science*, vol. 172, p. 109326, 2020.
- [20] J. Zhu and J. Luo, "Study of transformation induced intergranular microcracking in tetragonal zirconia polycrystals with the phase field method," *Materials Science and Engineering: A*, vol. 701, pp. 69-84, 2017.
- [21] T. Zhao, J. Zhu, and J. Luo, "Study of crack propagation behavior in single crystalline tetragonal zirconia with the phase field method," *Engineering Fracture Mechanics*, vol. 159, pp. 155-173, 2016.
- [22] E. Moshkelgosha and M. Mamivand, "Phase field modeling of crack propagation in shape memory ceramics—Application to zirconia," *Computational Materials Science*, vol. 174, p. 109509, 2020.
- [23] E. Moshkelgosha and M. Mamivand, "Concurrent modeling of martensitic transformation and crack growth in polycrystalline shape memory ceramics," *Engineering Fracture Mechanics*, vol. 241, p. 107403, 2021.
- [24] E. Moshkelgosha and M. Mamivand, "Three-dimensional phase field modeling of fracture in shape memory ceramics," *International Journal of Mechanical Sciences*, vol. 204, p. 106550, 2021.
- [25] J. Zhu, J. Luo, and Y. Sun, "Study of the Fracture Behavior of Tetragonal Zirconia Polycrystal with a Modified Phase Field Model," *Materials*, vol. 13, no. 19, p. 4430, 2020.
- [26] M. Asle Zaeem, N. Zhang, and M. Mamivand, "A review of computational modeling techniques in study and design of shape memory ceramics," *Computational Materials Science*, vol. 160, pp. 120-136, 2019.
- [27] V. Mazanova, M. Heczko, and J. Polak, "On the mechanism of fatigue crack initiation in high-angle grain boundaries," *International Journal of Fatigue*, vol. 158, p. 106721, 2022.

- [28] N. Nayan, D. Roy, V. Buravalla, and U. Ramamurty, "Unnotched fatigue behavior of an austenitic Ni–Ti shape memory alloy," *Materials Science and Engineering: A*, vol. 497, no. 1-2, pp. 333-340, 2008.
- [29] Y. Chen, S. Pan, M. Zhou, D. Yi, D. Xu, and Y. Xu, "Effects of inclusions, grain boundaries and grain orientations on the fatigue crack initiation and propagation behavior of 2524-T3 Al alloy," *Materials Science and Engineering: A*, vol. 580, pp. 150-158, 2013.
- [30] N. Zhang and M. Asle Zaeem, "Competing mechanisms between dislocation and phase transformation in plastic deformation of single crystalline yttria-stabilized tetragonal zirconia nanopillars," *Acta Materialia*, vol. 120, pp. 337-347, 2016.
- [31] M. Mamivand, M. Asle Zaeem, and H. El Kadiri, "A review on phase field modeling of martensitic phase transformation," *Computational Materials Science*, vol. 77, pp. 304-311, 2013.
- [32] A. Manonukul and F. Dunne, "High–and low–cycle fatigue crack initiation using polycrystal plasticity," *Proceedings of the Royal Society of London. Series A: Mathematical, Physical and Engineering Sciences*, vol. 460, no. 2047, pp. 1881-1903, 2004.
- [33] C. Sweeney, W. Vorster, S. Leen, E. Sakurada, P. McHugh, and F. Dunne, "The role of elastic anisotropy, length scale and crystallographic slip in fatigue crack nucleation," *Journal of the Mechanics and Physics of Solids*, vol. 61, no. 5, pp. 1224-1240, 2013.
- [34] X. Xie, G. Kang, Q. Kan, and C. Yu, "Phase-field theory based finite element simulation on thermo-mechanical cyclic deformation of polycrystalline super-elastic NiTi shape memory alloy," *Computational Materials Science*, vol. 184, p. 109899, 2020.
- [35] C. Cissé and M. Asle Zaeem, "An asymmetric elasto-plastic phase-field model for shape memory effect, pseudoelasticity and thermomechanical training in polycrystalline shape memory alloys," *Acta Materialia*, vol. 201, pp. 580-595, 2020.
- [36] B. Xu, C. Yu, Q. Kan, and G. Kang, "Phase field study on the microscopic mechanism of the cyclic degradation of shape memory effect in nano-polycrystalline NiTi shape memory alloys," *European Journal of Mechanics-A/Solids*, vol. 93, p. 104544, 2022.
- [37] P. S. Chaugule and J.-B. le Graverend, "Crystal-plasticity modeling of phase transformation–viscoplasticity coupling in high-temperature shape memory alloys," *International Journal of Plasticity*, vol. 153, p. 103243, 2022.
- [38] X. Xie, G. Kang, Q. Kan, C. Yu, and Q. Peng, "Phase field modeling for cyclic phase transition of NiTi shape memory alloy single crystal with super-elasticity," *Computational Materials Science*, vol. 143, pp. 212-224, 2018.
- [39] X. Xie, G. Kang, Q. Kan, C. Yu, and Q. Peng, "Phase field modeling to transformation induced plasticity in super-elastic NiTi shape memory alloy single crystal," *Modelling and Simulation in Materials Science and Engineering*, vol. 27, no. 4, p. 045001, 2019.
- [40] H. M. Paranjape, S. Manchiraju, and P. M. Anderson, "A phase field–Finite element approach to model the interaction between phase transformations and plasticity in shape memory alloys," *International Journal of Plasticity*, vol. 80, pp. 1-18, 2016.

- [41] B. Xu, G. Kang, Q. Kan, C. Yu, and X. Xie, "Phase field simulation on the cyclic degeneration of one-way shape memory effect of NiTi shape memory alloy single crystal," *International Journal of Mechanical Sciences*, vol. 168, p. 105303, 2020.
- [42] G. R. Johnson and W. H. Cook, "Fracture characteristics of three metals subjected to various strains, strain rates, temperatures and pressures," *Engineering fracture mechanics*, vol. 21, no. 1, pp. 31-48, 1985.
- [43] A. L. Gurson, "Continuum theory of ductile rupture by void nucleation and growth: Part I—Yield criteria and flow rules for porous ductile media," 1977.
- [44] M. Elices, G. Guinea, J. Gomez, and J. Planas, "The cohesive zone model: advantages, limitations and challenges," *Engineering fracture mechanics*, vol. 69, no. 2, pp. 137-163, 2002.
- [45] T. Belytschko and T. Black, "Elastic crack growth in finite elements with minimal remeshing," *International journal for numerical methods in engineering*, vol. 45, no. 5, pp. 601-620, 1999.
- [46] H. Li, J. Li, and H. Yuan, "A review of the extended finite element method on macrocrack and microcrack growth simulations," *Theoretical and Applied Fracture Mechanics*, vol. 97, pp. 236-249, 2018.
- [47] M. Ambati, T. Gerasimov, and L. De Lorenzis, "A review on phase-field models of brittle fracture and a new fast hybrid formulation," *Computational Mechanics*, vol. 55, no. 2, pp. 383-405, 2015.
- [48] J.-Y. Wu, V. P. Nguyen, C. T. Nguyen, D. Sutula, S. Sinaie, and S. P. Bordas, "Phase-field modeling of fracture," *Advances in applied mechanics*, vol. 53, pp. 1-183, 2020.
- [49] G. Pijaudier-Cabot and Z. P. Bažant, "Nonlocal damage theory," *Journal of engineering mechanics*, vol. 113, no. 10, pp. 1512-1533, 1987.
- [50] M. Ambati, T. Gerasimov, and L. De Lorenzis, "Phase-field modeling of ductile fracture," *Computational Mechanics*, vol. 55, no. 5, pp. 1017-1040, 2015.
- [51] H. Emilio Martinez-Paneda. (2019). Phase field fracture implementation in FEniCS.
- [52] A. Emdadi, W. G. Fahrenholtz, G. E. Hilmas, and M. Asle Zaeem, "A modified phase-field model for quantitative simulation of crack propagation in single-phase and multi-phase materials," *Engineering Fracture Mechanics*, vol. 200, pp. 339-354, 2018.
- [53] A. Lotfolahpour, W. Huber, and M. Asle Zaeem, "A phase-field model for interactive evolution of phase transformation and cracking in superelastic shape memory ceramics," *Computational Materials Science*, vol. 216, p. 111844, 2023.
- [54] S. E. Esfahani, I. Ghamarian, V. I. Levitas, and P. C. Collins, "Microscale phase field modeling of the martensitic transformation during cyclic loading of NiTi single crystal," *International Journal of Solids and Structures*, vol. 146, pp. 80-96, 2018.
- [55] M. A. Meyers, A. Mishra, and D. J. Benson, "Mechanical properties of nanocrystalline materials," *Progress in materials science*, vol. 51, no. 4, pp. 427-556, 2006.
- [56] D. Salamon, "Chapter 6 - Advanced Ceramics," in *Advanced Ceramics for Dentistry*, J. Z. Shen and T. Kosmač Eds. Oxford: Butterworth-Heinemann, 2014, pp. 103-122.

- [57] F.-Z. Dai, Y. Zhou, and W. Sun, "Segregation of solute atoms (Y, Nb, Ta, Mo and W) in ZrB<sub>2</sub> grain boundaries and their effects on grain boundary strengths: A first-principles investigation," *Acta Materialia*, vol. 127, pp. 312-318, 2017/04/01/ 2017, doi: <https://doi.org/10.1016/j.actamat.2017.01.048>.
- [58] R. K. Wade and J. J. Petrovic, "Fracture modes in MoSi<sub>2</sub>," *Journal of the American Ceramic Society*, vol. 75, no. 6, pp. 1682-1684, 1992.
- [59] T. Watanabe and S. Tsurekawa, "The control of brittleness and development of desirable mechanical properties in polycrystalline systems by grain boundary engineering," *Acta Materialia*, vol. 47, no. 15, pp. 4171-4185, 1999/11/01/ 1999, doi: [https://doi.org/10.1016/S1359-6454\(99\)00275-X](https://doi.org/10.1016/S1359-6454(99)00275-X).
- [60] R. Ayres and D. Stein, "A dislocation dynamics approach to prediction of cleavage planes in BCC metals," *Acta Metallurgica*, vol. 19, no. 8, pp. 789-794, 1971.
- [61] Y.-F. Guo and C.-Y. Wang, "Atomistic study of lattice trapping behavior for brittle fracture in bcc-iron," *Computational materials science*, vol. 40, no. 3, pp. 376-381, 2007.
- [62] A. Deschamps, S. Peron, Y. Brechet, J.-C. Ehrström, and L. Poizat, "High temperature cleavage fracture in 5383 aluminum alloy," *Materials Science and Engineering: A*, vol. 319, pp. 583-586, 2001.
- [63] K. Matsunaga, S. Ii, C. Iwamoto, T. Yamamoto, and Y. Ikuhara, "In situ observation of crack propagation in magnesium oxide ceramics," *Nanotechnology*, vol. 15, no. 6, p. S376, 2004.
- [64] G. A. Francfort and J.-J. Marigo, "Revisiting brittle fracture as an energy minimization problem," *Journal of the Mechanics and Physics of Solids*, vol. 46, no. 8, pp. 1319-1342, 1998.
- [65] B. Bourdin, G. A. Francfort, and J.-J. Marigo, "Numerical experiments in revisited brittle fracture," *Journal of the Mechanics and Physics of Solids*, vol. 48, no. 4, pp. 797-826, 2000.
- [66] C. Miehe, F. Welschinger, and M. Hofacker, "Thermodynamically consistent phase-field models of fracture: Variational principles and multi-field FE implementations," *International journal for numerical methods in engineering*, vol. 83, no. 10, pp. 1273-1311, 2010.
- [67] A. Mesgarnejad, B. Bourdin, and M. Khonsari, "Validation simulations for the variational approach to fracture," *Computer Methods in Applied Mechanics and Engineering*, vol. 290, pp. 420-437, 2015.
- [68] A. Emdadi, J. Watts, W. G. Fahrenholtz, G. E. Hilmas, and M. Asle Zaeem, "Predicting effective fracture toughness of ZrB<sub>2</sub>-based ultra-high temperature ceramics by phase-field modeling," *Materials & Design*, vol. 192, p. 108713, 2020/07/01/ 2020, doi: <https://doi.org/10.1016/j.matdes.2020.108713>.
- [69] A. Abdollahi and I. Arias, "Numerical simulation of intergranular and transgranular crack propagation in ferroelectric polycrystals," *International journal of fracture*, vol. 174, no. 1, pp. 3-15, 2012.

- [70] D. Fan and L.-Q. Chen, "Computer simulation of grain growth using a continuum field model," *Acta Materialia*, vol. 45, no. 2, pp. 611-622, 1997.
- [71] J. Clayton and J. Knap, "Phase field modeling of directional fracture in anisotropic polycrystals," *Computational Materials Science*, vol. 98, pp. 158-169, 2015.
- [72] T.-T. Nguyen, J. Rethore, J. Yvonnet, and M.-C. Baietto, "Multi-phase-field modeling of anisotropic crack propagation for polycrystalline materials," *Computational Mechanics*, vol. 60, no. 2, pp. 289-314, 2017.
- [73] M. Paggi, M. Corrado, and J. Reinoso, "Fracture of solar-grade anisotropic polycrystalline Silicon: A combined phase field–cohesive zone model approach," *Computer Methods in Applied Mechanics and Engineering*, vol. 330, pp. 123-148, 2018.
- [74] N. Nguyen-Thanh, W. Li, J. Huang, and K. Zhou, "Adaptive higher-order phase-field modeling of anisotropic brittle fracture in 3D polycrystalline materials," *Computer Methods in Applied Mechanics and Engineering*, vol. 372, p. 113434, 2020.
- [75] A. Emdadi and M. Asle Zaeem, "Phase-field modeling of crack propagation in polycrystalline materials," *Computational Materials Science*, vol. 186, p. 110057, 2021/01/01/ 2021, doi: <https://doi.org/10.1016/j.commatsci.2020.110057>.
- [76] A. A. Griffith, "VI. The phenomena of rupture and flow in solids," *Philosophical transactions of the royal society of london. Series A, containing papers of a mathematical or physical character*, vol. 221, no. 582-593, pp. 163-198, 1921.
- [77] C. Kuhn, A. Schlüter, and R. Müller, "On degradation functions in phase field fracture models," *Computational Materials Science*, vol. 108, pp. 374-384, 2015.
- [78] J. M. Sargado, E. Keilegavlen, I. Berre, and J. M. Nordbotten, "High-accuracy phase-field models for brittle fracture based on a new family of degradation functions," *Journal of the Mechanics and Physics of Solids*, vol. 111, pp. 458-489, 2018.
- [79] H. Amor, J.-J. Marigo, and C. Maurini, "Regularized formulation of the variational brittle fracture with unilateral contact: Numerical experiments," *Journal of the Mechanics and Physics of Solids*, vol. 57, no. 8, pp. 1209-1229, 2009.
- [80] M. J. Borden, C. V. Verhoosel, M. A. Scott, T. J. Hughes, and C. M. Landis, "A phase-field description of dynamic brittle fracture," *Computer Methods in Applied Mechanics and Engineering*, vol. 217, pp. 77-95, 2012.
- [81] C. Miehe, M. Hofacker, and F. Welschinger, "A phase field model for rate-independent crack propagation: Robust algorithmic implementation based on operator splits," *Computer Methods in Applied Mechanics and Engineering*, vol. 199, no. 45-48, pp. 2765-2778, 2010.
- [82] W. T. Read and W. Shockley, "Dislocation models of crystal grain boundaries," *Physical review*, vol. 78, no. 3, p. 275, 1950.
- [83] D. Wolf, "A read-shockley model for high-angle grain boundaries," *Scripta metallurgica*, vol. 23, no. 10, pp. 1713-1718, 1989.

- [84] H. Kurishita, A. Ôishi, H. Kubo, and H. Yoshinaga, "Grain Boundary Fracture in Molybdenum Bicrystals with Various (110) Symmetric Tilt Boundaries," *Transactions of the Japan institute of metals*, vol. 26, no. 5, pp. 341-352, 1985.
- [85] T. Watanabe and S. Tsurekawa, "Toughening of brittle materials by grain boundary engineering," *Materials Science and Engineering: A*, vol. 387, pp. 447-455, 2004.
- [86] L. Lim and T. Watanabe, "Fracture toughness and brittle-ductile transition controlled by grain boundary character distribution (GBCD) in polycrystals," *Acta metallurgica et materialia*, vol. 38, no. 12, pp. 2507-2516, 1990.
- [87] T. Csanádi, S. Grasso, A. Kovalčíková, J. Dusza, and M. Reece, "Nanohardness and elastic anisotropy of ZrB<sub>2</sub> crystals," *Journal of the European Ceramic Society*, vol. 36, no. 1, pp. 239-242, 2016.
- [88] A. L. Chamberlain, W. G. Fahrenholtz, G. E. Hilmas, and D. T. Ellerby, "High-strength zirconium diboride-based ceramics," *Journal of the American Ceramic Society*, vol. 87, no. 6, pp. 1170-1172, 2004.
- [89] M. J. Gasch, D. T. Ellerby, and S. M. Johnson, "Ultra high temperature ceramic composites," in *Handbook of ceramic composites*: Springer, 2005, pp. 197-224.
- [90] H. Kinoshita *et al.*, "ZrB<sub>2</sub> substrate for nitride semiconductors," *Japanese Journal of Applied Physics*, vol. 42, no. 4S, p. 2260, 2003.
- [91] H. Li *et al.*, "Crystal structure and elastic properties of ZrB compared with ZrB<sub>2</sub>: A first-principles study," *Computational Materials Science*, vol. 49, no. 4, pp. 814-819, 2010.
- [92] P. K. Kristensen and E. Martínez-Pañeda, "Phase field fracture modelling using quasi-Newton methods and a new adaptive step scheme," *Theoretical and Applied Fracture Mechanics*, vol. 107, p. 102446, 2020.
- [93] A. Rezaie, W. G. Fahrenholtz, and G. E. Hilmas, "Effect of hot pressing time and temperature on the microstructure and mechanical properties of ZrB<sub>2</sub>-SiC," *Journal of Materials Science*, vol. 42, no. 8, pp. 2735-2744, 2007.
- [94] E. W. Neuman, "Elevated temperature mechanical properties of zirconium diboride based ceramics," 2014.
- [95] V. V. Skripnyak, A. M. Bragov, V. A. Skripnyak, A. K. Lomunov, E. G. Skripnyak, and I. K. Vaganova, "Fracture mechanisms of zirconium diboride ultra-high temperature ceramics under pulse loading," in *AIP Conference Proceedings*, 2017, vol. 1793, no. 1: AIP Publishing LLC, p. 100003.
- [96] K. Faber and A. G. Evans, "Intergranular crack-deflection toughening in silicon carbide," *Journal of the American ceramic society*, vol. 66, no. 6, pp. C-94-C-95, 1983.
- [97] M. Simoes and E. Martínez-Pañeda, "Phase field modelling of fracture and fatigue in Shape Memory Alloys," *Computer Methods in Applied Mechanics and Engineering*, vol. 373, p. 113504, 2021.
- [98] E. Jebellat, M. Baniassadi, A. Moshki, K. Wang, and M. Baghani, "Numerical investigation of smart auxetic three-dimensional meta-structures based on shape memory

- polymers via topology optimization," *Journal of Intelligent Material Systems and Structures*, vol. 31, no. 15, pp. 1838-1852, 2020.
- [99] N. Roudbarian, E. Jebellat, S. Famouri, M. Baniasadi, R. Hedayati, and M. Baghani, "Shape-memory polymer metamaterials based on triply periodic minimal surfaces," *European Journal of Mechanics-A/Solids*, p. 104676, 2022.
- [100] T. W. Coyle, W. S. Coblenz, and B. A. Bender, "Transformation Toughening in Large-Grain-Size CeO<sub>2</sub>-Doped ZrO<sub>2</sub> Polycrystals," *Journal of the American Ceramic Society*, vol. 71, no. 2, pp. C-88-C-92, 1988.
- [101] A. Lotfolahpour and M. Asle Zaeem, "Effects of cleavage plane and material strength on fracture of polycrystalline brittle materials: A phase-field modeling study," *Computational Materials Science*, vol. 197, p. 110642, 2021.
- [102] S. Rezaei, A. Harandi, T. Brepols, and S. Reese, "An anisotropic cohesive fracture model: advantages and limitations of length-scale insensitive phase-field damage models," *Engineering Fracture Mechanics*, p. 108177, 2022.
- [103] M. J. Borden, T. J. Hughes, C. M. Landis, A. Anvari, and I. J. Lee, "A phase-field formulation for fracture in ductile materials: Finite deformation balance law derivation, plastic degradation, and stress triaxiality effects," *Computer Methods in Applied Mechanics and Engineering*, vol. 312, pp. 130-166, 2016.
- [104] W. Gao, X. Yi, G. Song, Z. Wang, and X. Meng, "Zr<sub>50</sub>Cu<sub>25</sub>Ni<sub>7.5</sub>Co<sub>17.5</sub> high-temperature shape memory alloy with excellent thermal stability and large recovery strain, and the associated microstructural deformation mechanism," *Materials & Design*, vol. 196, p. 109108, 2020.
- [105] M. Mamivand, M. Asle Zaeem, and H. El Kadiri, "Shape memory effect and pseudoelasticity behavior in tetragonal zirconia polycrystals: A phase field study," *International Journal of Plasticity*, vol. 60, pp. 71-86, 2014.
- [106] Y. Sun, J. Luo, and J. Zhu, "Ferroelastic toughening of single crystalline yttria-stabilized t'zirconia: A phase field study," *Engineering Fracture Mechanics*, vol. 233, p. 107077, 2020.
- [107] B. Xu, G. Kang, C. Yu, and Q. Kan, "Phase field simulation on the grain size dependent super-elasticity and shape memory effect of nanocrystalline NiTi shape memory alloys," *International Journal of Engineering Science*, vol. 156, p. 103373, 2020.
- [108] B. Xu and G. Kang, "Phase field simulation on the super-elasticity, elastocaloric and shape memory effect of geometrically graded nano-polycrystalline NiTi shape memory alloys," *International Journal of Mechanical Sciences*, vol. 201, p. 106462, 2021.
- [109] Y. Zhong and T. Zhu, "Phase-field modeling of martensitic microstructure in NiTi shape memory alloys," *Acta materialia*, vol. 75, pp. 337-347, 2014.
- [110] S. Xi and Y. Su, "Phase field study of the microstructural dynamic evolution and mechanical response of NiTi shape memory alloy under mechanical loading," *Materials*, vol. 14, no. 1, p. 183, 2021.

- [111] K. Noguchi, M. Fujita, T. Masaki, and M. Mizushina, "Tensile strength of yttria-stabilized tetragonal zirconia polycrystals," *Journal of the American Ceramic Society*, vol. 72, no. 7, pp. 1305-1307, 1989.
- [112] J. Kondoh, H. Shiota, K. Kawachi, and T. Nakatani, "Yttria concentration dependence of tensile strength in yttria-stabilized zirconia," *Journal of alloys and compounds*, vol. 365, no. 1-2, pp. 253-258, 2004.
- [113] K. Noguchi, Y. Matsuda, M. Oishi, T. Masaki, S. Nakayama, and M. Mizushina, "Strength analysis of yttria-stabilized tetragonal zirconia polycrystals," *Journal of the American Ceramic Society*, vol. 73, no. 9, pp. 2667-2676, 1990.
- [114] M. Oishi, Y. Matsuda, K. Noguchi, and T. Masaki, "Evaluation of Tensile Strength and Fracture Toughness of Yttria-Stabilized Zirconia Polycrystals with Fracture Surface Analysis," *Journal of the American Ceramic Society*, vol. 78, no. 5, pp. 1212-1216, 1995.
- [115] K. Gall, N. Yang, H. Sehitoglu, and Y. I. Chumlyakov, "Fracture of precipitated NiTi shape memory alloys," *International journal of fracture*, vol. 109, no. 2, pp. 189-207, 2001.
- [116] L. Krone, E. Schüller, M. Bram, O. Hamed, H.-P. Buchkremer, and D. Stöver, "Mechanical behaviour of NiTi parts prepared by powder metallurgical methods," *Materials Science and Engineering: A*, vol. 378, no. 1-2, pp. 185-190, 2004.
- [117] S. Gollerthan, M. Young, A. Baruj, J. Frenzel, W. W. Schmahl, and G. Eggeler, "Fracture mechanics and microstructure in NiTi shape memory alloys," *Acta Materialia*, vol. 57, no. 4, pp. 1015-1025, 2009.
- [118] A. Creuziger, L. Bartol, K. Gall, and W. Crone, "Fracture in single crystal NiTi," *Journal of the Mechanics and Physics of Solids*, vol. 56, no. 9, pp. 2896-2905, 2008.
- [119] A. Dehghani and F. Aslani, "Crack recovery and re-centring performance of cementitious composites with pseudoelastic shape memory alloy fibres," *Construction and Building Materials*, vol. 298, p. 123888, 2021.
- [120] Z. Chen and H. L. Schreyer, "A numerical solution scheme for softening problems involving total strain control," *Computers & structures*, vol. 37, no. 6, pp. 1043-1050, 1990.
- [121] Y. Sun, J. Luo, J. Zhu, and K. Zhou, "A non-isothermal phase field study of the shape memory effect and pseudoelasticity of polycrystalline shape memory alloys," *Computational Materials Science*, vol. 167, pp. 65-76, 2019.
- [122] Y. Wen, Y. Wang, and L.-Q. Chen, "Effect of elastic interaction on the formation of a complex multi-domain microstructural pattern during a coherent hexagonal to orthorhombic transformation," *Acta materialia*, vol. 47, no. 17, pp. 4375-4386, 1999.
- [123] Y. Zhang, X. Jin, and T. Hsu, "Thermodynamic calculation of Ms in ZrO<sub>2</sub>-CeO<sub>2</sub>-Y<sub>2</sub>O<sub>3</sub> system," *Journal of the European Ceramic Society*, vol. 23, no. 5, pp. 685-690, 2003.
- [124] L. D. Landau, *Collected papers of LD Landau*. Pergamon, 1965.

- [125] S. M. Allen and J. W. Cahn, "A microscopic theory for antiphase boundary motion and its application to antiphase domain coarsening," *Acta metallurgica*, vol. 27, no. 6, pp. 1085-1095, 1979.
- [126] M. Hofacker and C. Miehe, "Continuum phase field modeling of dynamic fracture: variational principles and staggered FE implementation," *International journal of fracture*, vol. 178, no. 1, pp. 113-129, 2012.
- [127] J. Chevalier, L. Gremillard, A. V. Virkar, and D. R. Clarke, "The tetragonal-monoclinic transformation in zirconia: lessons learned and future trends," *Journal of the american ceramic society*, vol. 92, no. 9, pp. 1901-1920, 2009.
- [128] H. Scott, "Phase relationships in the zirconia-yttria system," *Journal of materials science*, vol. 10, no. 9, pp. 1527-1535, 1975.
- [129] E. H. Kisi and C. J. Howard, "Elastic constants of tetragonal zirconia measured by a new powder diffraction technique," *Journal of the American Ceramic Society*, vol. 81, no. 6, pp. 1682-1684, 1998.
- [130] X.-S. Zhao, S.-L. Shang, Z.-K. Liu, and J.-Y. Shen, "Elastic properties of cubic, tetragonal and monoclinic ZrO<sub>2</sub> from first-principles calculations," *Journal of nuclear materials*, vol. 415, no. 1, pp. 13-17, 2011.
- [131] M. Asle Zaeem, H. El Kadiri, S. D. Mesarovic, M. F. Horstemeyer, and P. T. Wang, "Effect of the compositional strain on the diffusive interface thickness and on the phase transformation in a phase-field model for binary alloys," *Journal of phase equilibria and diffusion*, vol. 32, no. 4, pp. 302-308, 2011.
- [132] A. Emdadi and M. Asle Zaeem, "Phase-field modeling of crack propagation in polycrystalline materials," *Computational Materials Science*, vol. 186, p. 110057, 2021.
- [133] A. Loganathan and A. S. Gandhi, "Effect of phase transformations on the fracture toughness of t' yttria stabilized zirconia," *Materials Science and Engineering: A*, vol. 556, pp. 927-935, 2012.
- [134] X. Li and Y. Su, "A phase-field study of the martensitic detwinning in NiTi shape memory alloys under tension or compression," *Acta Mechanica*, vol. 231, no. 4, pp. 1539-1557, 2020.
- [135] B. Xu, C. Yu, and G. Kang, "Phase field study on the microscopic mechanism of grain size dependent cyclic degradation of super-elasticity and shape memory effect in nanopolycrystalline NiTi alloys," *International Journal of Plasticity*, vol. 145, p. 103075, 2021.
- [136] S. Robertson, A. Mehta, A. Pelton, and R. Ritchie, "Evolution of crack-tip transformation zones in superelastic Nitinol subjected to in situ fatigue: A fracture mechanics and synchrotron X-ray microdiffraction analysis," *Acta Materialia*, vol. 55, no. 18, pp. 6198-6207, 2007.
- [137] J. Chevalier, C. Olagnon, and G. Fantozzi, "Crack propagation and fatigue in zirconia-based composites," *Composites Part A: Applied Science and Manufacturing*, vol. 30, no. 4, pp. 525-530, 1999.

- [138] E. Camposilvan and M. Anglada, "Size and plasticity effects in zirconia micropillars compression," *Acta Materialia*, vol. 103, pp. 882-892, 2016.
- [139] J. Lankford, R. Page, and L. Rabenberg, "Deformation mechanisms in yttria-stabilized zirconia," *Journal of materials Science*, vol. 23, pp. 4144-4156, 1988.
- [140] Q. Kan, Y. Zhang, W. Shi, Y. Xu, C. Yu, and G. Kang, "Functional fatigue of superelasticity and elastocaloric effect for NiTi springs," *International Journal of Mechanical Sciences*, vol. 265, p. 108889, 2024.
- [141] T. Zhao and G. Kang, "Experimental study and life prediction on fatigue failure of NiTi shape memory alloy under multi-axial one-way shape memory cyclic loadings," *International Journal of Fatigue*, vol. 155, p. 106609, 2022.
- [142] R. Sidharth, A. Mohammed, and H. Sehitoglu, "Functional fatigue of NiTi shape memory alloy: effect of loading frequency and source of residual strains," *Shape Memory and Superelasticity*, vol. 8, no. 4, pp. 394-412, 2022.
- [143] Y. Zhang, Z. Moumni, Y. You, W. Zhang, J. Zhu, and G. Anlas, "Multiscale TRIP-based investigation of low-cycle fatigue of polycrystalline NiTi shape memory alloys," *International Journal of Plasticity*, vol. 115, pp. 307-329, 2019.
- [144] V. Wan, D. MacLachlan, and F. Dunne, "A stored energy criterion for fatigue crack nucleation in polycrystals," *International Journal of Fatigue*, vol. 68, pp. 90-102, 2014.
- [145] C. Cissé and M. Asle Zaeem, "Design of NiTi-based shape memory microcomposites with enhanced elastocaloric performance by a fully thermomechanical coupled phase-field model," *Materials & Design*, vol. 207, p. 109898, 2021.
- [146] C. Cissé and M. Asle Zaeem, "An Asymmetric Elasto-Plastic Phase-Field Model for Shape Memory Effect, Pseudoelasticity and Thermomechanical Training in Polycrystalline Shape Memory Alloys," *Acta Materialia*, vol. 201, pp. 580-595, 2020/12/01/ 2020, doi: <https://doi.org/10.1016/j.actamat.2020.10.034>.
- [147] M. Asle Zaeem, N. Zhang, and M. Mamivand, "A review of computational modeling techniques in study and design of shape memory ceramics," *Computational Materials Science*, vol. 160, pp. 120-136, 2019/04/01/ 2019, doi: <https://doi.org/10.1016/j.commatsci.2018.12.062>.
- [148] C. Yu, G. Kang, Q. Kan, and D. Song, "A micromechanical constitutive model based on crystal plasticity for thermo-mechanical cyclic deformation of NiTi shape memory alloys," *International Journal of Plasticity*, vol. 44, pp. 161-191, 2013.
- [149] C. Yu, G. Kang, and Q. Kan, "Crystal plasticity based constitutive model of NiTi shape memory alloy considering different mechanisms of inelastic deformation," *International Journal of Plasticity*, vol. 54, pp. 132-162, 2014.
- [150] C. Yu, G. Kang, and Q. Kan, "A micromechanical constitutive model for anisotropic cyclic deformation of super-elastic NiTi shape memory alloy single crystals," *Journal of the Mechanics and Physics of Solids*, vol. 82, pp. 97-136, 2015.
- [151] C. Yu, G. Kang, Q. Kan, and X. Xu, "Physical mechanism based crystal plasticity model of NiTi shape memory alloys addressing the thermo-mechanical cyclic degeneration of shape memory effect," *Mechanics of Materials*, vol. 112, pp. 1-17, 2017.

- [152] H. M. Paranjape, M. L. Bowers, M. J. Mills, and P. M. Anderson, "Mechanisms for phase transformation induced slip in shape memory alloy micro-crystals," *Acta Materialia*, vol. 132, pp. 444-454, 2017.
- [153] X. Ju *et al.*, "A multi-physics, multi-scale and finite strain crystal plasticity-based model for pseudoelastic NiTi shape memory alloy," *International Journal of Plasticity*, vol. 148, p. 103146, 2022.
- [154] Z. Bo and D. C. Lagoudas, "Thermomechanical modeling of polycrystalline SMAs under cyclic loading, Part III: evolution of plastic strains and two-way shape memory effect," *International Journal of Engineering Science*, vol. 37, no. 9, pp. 1175-1203, 1999.
- [155] J. Wang, Z. Moumni, and W. Zhang, "A thermomechanically coupled finite-strain constitutive model for cyclic pseudoelasticity of polycrystalline shape memory alloys," *International Journal of Plasticity*, vol. 97, pp. 194-221, 2017.
- [156] P. Ebrahimi, J. Arghavani, R. Naghdabadi, and J. P. McGarry, "On the effect of detwinning-induced plasticity in compressive cyclic loading of NiTi shape memory alloys," *Mechanics of Materials*, vol. 148, p. 103451, 2020.
- [157] Q. Kan, W. Shi, D. Song, C. Yu, and G. Kang, "A micromechanical constitutive model of high-temperature shape memory alloys," *International Journal of Mechanical Sciences*, vol. 251, p. 108328, 2023.
- [158] M. R. Karamooz-Ravari, M. T. Andani, M. Kadkhodaei, S. Saedi, H. Karaca, and M. Elahinia, "Modeling the cyclic shape memory and superelasticity of selective laser melting fabricated NiTi," *International Journal of Mechanical Sciences*, vol. 138, pp. 54-61, 2018.
- [159] Y. Xiao and D. Jiang, "Constitutive modelling of transformation pattern in superelastic NiTi shape memory alloy under cyclic loading," *International Journal of Mechanical Sciences*, vol. 182, p. 105743, 2020.
- [160] M. Simoes, C. Braithwaite, A. Makaya, and E. Martínez-Pañeda, "Modelling fatigue crack growth in shape memory alloys," *Fatigue & Fracture of Engineering Materials & Structures*, vol. 45, no. 4, pp. 1243-1257, 2022.
- [161] L. A. Woodworth and M. Kaliske, "A temperature dependent constitutive model for functional fatigue in shape memory alloys," *Mechanics of Materials*, vol. 165, p. 104126, 2022.
- [162] X. Zhang, X. Yan, H. Xie, and R. Sun, "Modeling evolutions of plastic strain, maximum transformation strain and transformation temperatures in SMA under superelastic cycling," *Computational materials science*, vol. 81, pp. 113-122, 2014.
- [163] E. C. Bingham, *An investigation of the laws of plastic flow* (no. 278). US Government Printing Office, 1917.
- [164] W. Huber and M. Asle Zaeem, "A mixed mode phase-field model of ductile fracture," *Journal of the Mechanics and Physics of Solids*, vol. 171, p. 105123, 2023.
- [165] E. A. de Souza Neto, D. Peric, and D. R. Owen, *Computational methods for plasticity: theory and applications*. John Wiley & Sons, 2011.

- [166] H. W. Kuhn and A. W. Tucker, "Nonlinear programming," in *Traces and emergence of nonlinear programming*: Springer, 2013, pp. 247-258.
- [167] M. Asle Zaeem, H. El Kadiri, P. T. Wang, and M. F. Horstemeyer, "Investigating the effects of grain boundary energy anisotropy and second-phase particles on grain growth using a phase-field model," *Computational Materials Science*, vol. 50, no. 8, pp. 2488-2492, 2011/06/01/ 2011, doi: <https://doi.org/10.1016/j.commatsci.2011.03.031>.
- [168] M. Keuper, C. Berthold, and K. G. Nickel, "Long-time aging in 3 mol.% yttria-stabilized tetragonal zirconia polycrystals at human body temperature," *Acta biomaterialia*, vol. 10, no. 2, pp. 951-959, 2014.
- [169] S. K. Chan *et al.*, "Temperature dependence of the elastic moduli of monoclinic zirconia," *Journal of the American Ceramic Society*, vol. 74, no. 7, pp. 1742-1744, 1991.
- [170] K. Ren, J. Xia, and Y. Wang, "Grain growth kinetics of 3 mol.% yttria-stabilized zirconia during flash sintering," *Journal of the European Ceramic Society*, vol. 39, no. 4, pp. 1366-1373, 2019.
- [171] Y. Zhang, Y. You, Z. Mounni, G. Anlas, J. Zhu, and W. Zhang, "Experimental and theoretical investigation of the frequency effect on low cycle fatigue of shape memory alloys," *International Journal of Plasticity*, vol. 90, pp. 1-30, 2017.
- [172] S. Sarker, H. T. Mumu, M. Al-Amin, M. Z. Alam, and M. Gafur, "Impacts of inclusion of additives on physical, microstructural, and mechanical properties of Alumina and Zirconia toughened alumina (ZTA) ceramic composite: A review," *Materials Today: Proceedings*, vol. 62, pp. 2892-2918, 2022.
- [173] K. Pearson, "VII. Mathematical contributions to the theory of evolution.—III. Regression, heredity, and panmixia," *Philosophical Transactions of the Royal Society of London. Series A, containing papers of a mathematical or physical character*, no. 187, pp. 253-318, 1896.
- [174] J. Lee Rodgers and W. A. Nicewander, "Thirteen ways to look at the correlation coefficient," *The American Statistician*, vol. 42, no. 1, pp. 59-66, 1988.
- [175] D. Wicht, M. Schneider, and T. Böhlke, "An efficient solution scheme for small-strain crystal-elasto-viscoplasticity in a dual framework," *Computer Methods in Applied Mechanics and Engineering*, vol. 358, p. 112611, 2020.
- [176] H. Chalal and F. Abed-Meraim, "Hardening effects on strain localization predictions in porous ductile materials using the bifurcation approach," *Mechanics of Materials*, vol. 91, pp. 152-166, 2015.
- [177] N. Zhang and M. Asle Zaeem, "Effects of grain orientations and pre-existing defects on mechanical properties and deformation mechanisms of polycrystalline yttria-stabilized tetragonal zirconia," *Materialia*, vol. 9, p. 100553, 2020.

APPENDIX A  
PERMISSION FOR REUSE OF PUBLISHED MATERIALS

Uploaded as an electronic supplementary file.